

# **X-ray scattering and spectroscopy of supercooled water and ice**

JONAS ALEXANDER SELLBERG

Doctoral Thesis in Chemical Physics  
Stockholm University 2014



*Thesis for the Degree of Doctor of Philosophy in Chemical Physics*  
Department of Physics  
AlbaNova University Center  
Stockholm University  
Stockholm, Sweden

*The front drawing depicts scattering of a single x-ray laser pulse hitting a droplet that contains water (lower left) or ice (upper right). Darker blue corresponds to more intense scattering. The orientation is not representative of reciprocal space.*

© Jonas A. Sellberg (2014) ISBN 978-91-7447-902-7  
Printed by Universitetsservice US-AB, Stockholm, Sweden  
Paper I © Royal Society of Chemistry Publishing  
Paper II © Nature Publishing Group

*Strength does not come from physical capacity. It comes from an indomitable will.*  
Mahatma Gandhi





# Abstract

This thesis presents experimental studies of water and ice at near-atmospheric pressures using intense x-rays only accessible at synchrotrons and free-electron lasers. In particular, it focuses on the deeply supercooled, metastable state and its implications on ice nucleation.

The local structure of the liquid phase was studied by x-ray scattering over a wide temperature range extending from 339 K down to 227 K. In order to be able to study the deeply supercooled liquid, micron-sized water droplets were evaporatively cooled in vacuum and probed by ultrashort x-ray pulses. This is to date the lowest temperature at which measurements of the structure have been performed on bulk liquid water cooled from room temperature. Upon deep supercooling, the structure evolved toward that of a low-density liquid with local tetrahedral coordination. At  $\sim 230$  K, where the low-density liquid structure started to dominate, the number of droplets containing ice nuclei increased rapidly. The estimated nucleation rate suggests that there is a “fragile-to-strong” transition in the dynamics of the liquid below 230 K, and its implications on water structure are discussed.

Similarly, the electronic structure of deeply supercooled water was studied by x-ray emission spectroscopy down to 222 K, but the spectral changes expected from the structural transformation remained absent and explanations are discussed. At high fluence, the non-linear dependence of the x-ray emission yield indicated that there were high valence hole densities created during the x-ray pulse length due to Auger cascades, resulting in reabsorption of the x-ray emission.

Finally, the hydrogen-bonded network in water was studied by x-ray absorption spectroscopy and compared to various ices. It was found that the pre-edge absorption cross-section, which is associated with distorted hydrogen bonds, could be minimized for crystalline ice grown on a hydrophobic  $\text{BaF}_2(111)$  surface with low concentration of nucleation centers.



# List of Publications

This thesis is based on the following six papers, which will be referred to in the text by their corresponding Roman numerals. Reprints\* were made with the permission from the publishers.

**I. Wide-angle X-ray diffraction and molecular dynamics study of medium-range order in ambient and hot water**

C. Huang, K. T. Wikfeldt, D. Nordlund, U. Bergmann, T. McQueen, J. Sellberg, L. G. M. Pettersson, A. Nilsson

*Physical Chemistry Chemical Physics* **13**, 19997-20007 (2011)

**II. Experimental Observation of Bulk Liquid Water Structure in "No-man's Land"**

J. A. Sellberg, C. Huang, T. A. McQueen, N. D. Loh, H. Laksmono, D. Schlesinger, R. G. Sierra, D. Nordlund, C. Y. Hampton, D. Starodub, D. P. DePonte, M. Beye, C. Chen, A. V. Martin, A. Barty, K. T. Wikfeldt, T. M. Weiss, C. Caronna, J. Feldkamp, L. B. Skinner, M. M. Seibert, M. Messerschmidt, G. J. Williams, S. Boutet, L. G. M. Pettersson, M. J. Bogan, A. Nilsson

Accepted in *Nature* doi:10.1038/nature13266 (2014)

**III. Anomalous Behavior of the Homogeneous Ice Nucleation Rate in "No-man's Land"**

H. Laksmono, T. A. McQueen, J. A. Sellberg, N. D. Loh, C. Huang, R. G. Sierra, D. Schlesinger, C. Y. Hampton, D. Starodub, D. P. DePonte, D. Nordlund, M. Beye, A. V. Martin, A. Barty, L. G. M. Pettersson, M. Seibert, M. Messerschmidt, G. J. Williams, S. Boutet, M. J. Bogan, A. Nilsson

Manuscript

---

\*<http://pubs.rsc.org/en/Content/ArticleLanding/2011/CP/C1CP22804H>  
<http://dx.doi.org/doi:10.1038/nature13266>

**IV. Comparison of x-ray absorption spectra between water and ice: new ice data with low pre-edge absorption cross-section**

J. A. Sellberg, S. Kaya, V. H. Segtnan, C. Chen, T. Tyliczszak, H. Ogasawara, D. Nordlund, L. G. M. Pettersson, A. Nilsson

Submitted to *Journal of Chemical Physics*

**V. Reabsorption of Soft X-ray Emission at High X-ray Free-Electron Laser Fluences**

S. Schreck, M. Beye, J. A. Sellberg, T. McQueen, H. Laksmono, D. DePonte, B. Kennedy, S. Eckert, D. Schlesinger, D. Nordlund, H. Ogasawara, R. G. Sierra, V. H. Segtnan, K. Kubicek, W. F. Schlotter, G. Dakovski, S. P. Moeller, U. Bergmann, S. Techert, L. G. M. Pettersson, Ph. Wernet, M. J. Bogan, Y. Harada, A. Nilsson, A. Föhlisch

Submitted to *Physical Review Letters*

**VI. X-ray Emission Spectroscopy of Bulk Liquid Water in "No-man's Land"**

J. A. Sellberg, T. A. McQueen, H. Laksmono, S. Schreck, M. Beye, D. P. DePonte, B. O'Kennedy, D. Nordlund, R. G. Sierra, D. Schlesinger, T. Tokushima, S. Eckert, V. H. Segtnan, H. Ogasawara, K. Kubicek, S. Techert, U. Bergmann, G. L. Dakovski, W. F. Schlotter, Y. Harada, I. Zhovtobriukh, L. G. M. Pettersson, M. J. Bogan, Ph. Wernet, A. Föhlisch, A. Nilsson

Manuscript

The following is a list of papers to which I have contributed but that are left out in this thesis. If used in the text, they will be referred to as normal references.

**A. Effect of H<sub>2</sub>S on Fe Corrosion in CO<sub>2</sub>-saturated Brine**

E. Abelev, J. Sellberg, T. A. Ramanarayanan, S. L. Bernasek

*Journal of Materials Science* **44**, 6167-6181 (2009)

**B. Room Temperature Femtosecond X-ray Diffraction of Photosystem II Microcrystals**

J. Kern, R. Alonso-Mori, J. Hellmich, R. Tran, J. Hattne, H. Laksmono, C. Glöckner, N. Echols, R. G. Sierra, J. Sellberg, B. Lassalle-Kaiser, R. J. Gildea, P. Glatzel, R. W. Grosse-Kunstleve, M. J. Latimer, T. A. McQueen, D. DiFiore, A. R. Fry, M. Messerschmidt, A. Miahnahri, D. W. Schafer, M. M. Seibert, D. Sokaras, T.-C. Weng, P. H. Zwart, W. E. White, P. D. Adams, M. J. Bogan, S. Boutet, G. J. Williams, J. Messinger, N. K. Sauter, A. Zouni, U. Bergmann, J. Yano, V. K. Yachandra

*Proceedings of the National Academy of Sciences* **109**, 9721-9726 (2012)

**C. Nanoflow electrospinning serial femtosecond crystallography**

R. G. Sierra, H. Laksmono, J. Kern, R. Tran, J. Hattne, R. Alonso-Mori, B. Lassalle-Kaiser, C. Glöckner, J. Hellmich, D. W. Schafer, N. Echols, R. J. Gildea, R. W. Grosse-Kunstleve, J. Sellberg, T. A. McQueen, A. R. Fry, M. Messerschmidt, A. Miahnahri, M. M. Seibert, C. Y. Hampton, D. Starodub, N. D. Loh, D. Sokaras, T.-C. Weng, P. H. Zwart, P. Glatzel, D. Milathianaki, W. E. White, P. D. Adams, G. J. Williams, S. Boutet, A. Zouni, J. Messinger, N. K. Sauter, U. Bergmann, J. Yano, V. K. Yachandra, M. J. Bogan

*Acta Crystallographica* **D68**, 1584-1587 (2012)

**D. Energy-dispersive X-ray emission spectroscopy using an X-ray free-electron laser in a shot-by-shot mode**

R. Alonso-Mori, J. Kern, R. J. Gildea, D. Sokaras, T.-C. Weng, B. Lassalle-Kaiser, R. Tran, J. Hattne, H. Laksmono, J. Hellmich, C. Glöckner, N. Echols, R. G. Sierra, D. W. Schafer, J. Sellberg, C. Kenney, R. Herbst, J. Pines, P. Hart, S. Herrmann, R. W. Grosse-Kunstleve, M. J. Latimer, A. R. Fry, M. Messerschmidt, A. Miahnahri, M. M. Seibert, P. H. Zwart, W. E. White, P. D. Adams, M. J. Bogan, S. Boutet, G. J. Williams, A. Zouni, J. Messinger, P. Glatzel, N. K. Sauter, V. K. Yachandra, J. Yano, U. Bergmann

*Proceedings of the National Academy of Sciences* **109**, 19103-19107 (2012)

**E. Real-Time Observation of Surface Bond Breaking with an X-ray Laser**

M. Dell'Angela, T. Anniyev, M. Beye, R. Coffee, A. Föhlisch, J. Gladh, T. Katayama, S. Kaya, O. Krupin, A. Møgelhøj, D. Nordlund, J. K. Nørskov, H. Öberg, H. Ogasawara, H. Öström, L. G. M. Pettersson, W. F. Schlotter, J. A. Sellberg, F. Sorgenfrei, J. J. Turner, M. Wolf, W. Wurth, A. Nilsson

*Science* **339**, 1302-1305 (2013)

**F. Ultrafast soft x-ray emission spectroscopy of surface adsorbates using an x-ray free electron laser**

T. Katayama, T. Anniyev, M. Beye, R. Coffee, M. Dell'Angela, A. Föhlisch, J. Gladh, S. Kaya, O. Krupin, A. Nilsson, D. Nordlund, W. F. Schlotter, J. A. Sellberg, F. Sorgenfrei, J. J. Turner, W. Wurth, H. Öström, H. Ogasawara

*Journal of Electron Spectroscopy and Related Phenomena* **187**, 9-14 (2013)

**G. Simultaneous Femtosecond X-ray Spectroscopy and Diffraction of Photosystem II at Room Temperature**

J. Kern, R. Alonso-Mori, R. Tran, J. Hattne, R. J. Gildea, N. Echols, C. Glöckner, J. Hellmich, H. Laksmono, R. G. Sierra, B. Lassalle-Kaiser, S. Koroidov, A. Lampe, G. Han, S. Gul, D. DiFiore, D. Milathianaki, A. R. Fry, A. Miahnahri, D. W. Schafer, M. Messerschmidt, M. M. Seibert, J. E. Koglin, D. Sokaras, T.-C. Weng, J. Sellberg, M. J. Latimer, R. W. Grosse-Kunstleve, P. H. Zwart, W. E. White, P. Glatzel, P. D. Adams, M. J. Bogan, G. J. Williams, S. Boutet, J. Messinger, A. Zouni, N. K. Sauter, V. K. Yachandra, U. Bergmann, J. Yano  
*Science* **340**, 491-495 (2013)

**H. Selective Ultrafast Probing of Transient Hot Chemisorbed and Precursor States of CO on Ru(0001)**

T. Anniyev, M. Beye, R. Coffee, M. Dell'Angela, A. Föhlisch, J. Gladh, T. Katayama, S. Kaya, O. Krupin, A. Møgelhøj, D. Nordlund, J. K. Nørskov, H. Öberg, H. Ogasawara, H. Öström, L. G. M. Pettersson, W. F. Schlotter, J. A. Sellberg, F. Sorgenfrei, J. J. Turner, M. Wolf, W. Wurth, A. Nilsson  
*Physical Review Letters* **110**, 186101 (2013)

**I. Accurate macromolecular structures using minimal measurements from X-ray free-electron lasers**

J. Hattne, N. Echols, R. Tran, J. Kern, R. J. Gildea, A. S. Brewster, R. Alonso-Mori, C. Glöckner, J. Hellmich, H. Laksmono, R. G. Sierra, B. Lassalle-Kaiser, A. Lampe, G. Han, S. Gul, D. DiFiore, D. Milathianaki, A. R. Fry, A. Miahnahri, W. E. White, D. W. Schafer, M. M. Seibert, J. E. Koglin, D. Sokaras, T.-C. Weng, J. Sellberg, M. J. Latimer, P. Glatzel, P. H. Zwart, R. W. Grosse-Kunstleve, M. J. Bogan, M. Messerschmidt, G. J. Williams, S. Boutet, J. Messinger, A. Zouni, J. Yano, U. Bergmann, V. K. Yachandra, P. D. Adams, N. K. Sauter  
*Nature Methods* doi:10.1038/nmeth.2887, advance online publication (2014)

**J. Observation of correlated x-ray scattering at atomic resolution**

D. Mendez, T. Lane, J. Sung, J. Sellberg, C. Levard, H. Watkins, A. Cohen, M. Soltis, S. Sutton, J. Spudich, V. Pande, D. Ratner, S. Doniach  
Accepted in *Philosophical Transactions of the Royal Society B* (2014)

# Note on Contribution

As the experiments performed at the Linac Coherent Light Source (LCLS) are large international collaborations, it is critical to specify my contribution to the projects. This thesis will highlight the work that was mainly or partly done by myself. For all projects, I partook in conducting the experiments. Chapter 4 focuses on methods used to perform the experiments and Chapter 5 describes the analysis performed on the data that I contributed to and that is necessary to understand the results. In Chapters 6-7 I will summarize the main results of Papers I-VI and put them into perspective. Below is a short description of my contribution to the listed publications.

In Paper I, I conducted the experiment at beam line (BL) 7-2 at Stanford Synchrotron Radiation Lightsource (SSRL) and proof-read the manuscript. In Papers II-III, I prepared and tested the injector setup in the laboratory and conducted the experiment at the Coherent X-ray Imaging (CXI) instrument at LCLS. I developed and implemented algorithms in C++ to extract and correct the raw data. I performed all data corrections and participated in sorting and analyzing the data. I wrote the majority of the supplementary material in Paper II and parts of the manuscripts in Papers II-III. In Paper IV, I performed the experiment at BL 13-2 at SSRL. I designed and tested the sample holder in the laboratory and conducted the experiments at BL 11.0.2 at the Advanced Light Source (ALS). I analyzed all data and wrote the manuscript together with my supervisors. In Papers V-VI, I planned and designed the experiment, including writing the proposal that enabled the experiment. I prepared and tested the injector setup at the BESSY II synchrotron and conducted the experiment at the Soft X-ray Materials Science (SXR) instrument at LCLS. In Paper V, I commented and proof-read the manuscript, whereas in Paper VI, I analyzed the data and wrote parts of the manuscript.





# Contents

<b>Abstract</b>	<b>v</b>
<b>List of Publications</b>	<b>vii</b>
<b>Note on Contribution</b>	<b>xi</b>
<b>Contents</b>	<b>xiii</b>
<b>List of Abbreviations</b>	<b>xvii</b>
<b>1 Introduction</b>	<b>1</b>
<b>2 Light-matter Interactions</b>	<b>5</b>
2.1 Photoelectric Effect . . . . .	6
2.2 Absorption and Scattering Cross-sections . . . . .	6
2.2.1 Thomson Scattering . . . . .	7
2.2.2 Absorption . . . . .	8
2.2.3 Compton Scattering . . . . .	9
2.3 Elastic Scattering Theory . . . . .	10
2.3.1 Born Approximation . . . . .	10
2.3.2 X-ray Scattering of Solids . . . . .	13
2.3.3 X-ray Scattering of Liquids . . . . .	15
2.3.4 X-ray Diffraction of Crystals . . . . .	19
2.4 Core-level Spectroscopy . . . . .	20
2.5 Quantum Description of Light . . . . .	22
2.5.1 Dipole Approximation . . . . .	26
2.5.2 X-ray Photoelectron Spectroscopy . . . . .	28
2.5.3 X-ray Absorption Spectroscopy . . . . .	29
2.5.4 X-ray Emission Spectroscopy . . . . .	29
2.5.5 Auger Electron Spectroscopy . . . . .	30

<b>3</b>	<b>Water</b>	<b>31</b>
3.1	The Water Molecule . . . . .	31
3.2	The Hydrogen Bond . . . . .	33
3.3	Thermodynamics of Water . . . . .	35
3.4	Crystalline Ice . . . . .	37
3.5	Polyamorphism of Water . . . . .	39
3.5.1	Low-density Amorphous Ice . . . . .	40
3.5.2	High-density Amorphous Ice . . . . .	40
3.5.3	Very High-density Amorphous Ice . . . . .	41
3.6	Theoretical Scenarios of Metastable Water . . . . .	42
3.6.1	Stability-limit Conjecture . . . . .	42
3.6.2	Critical Point-free Model . . . . .	43
3.6.3	Singularity-free Scenario . . . . .	44
3.6.4	Second Critical Point . . . . .	44
3.6.5	Equilibration and Metastability Below $T_h$ . . . . .	46
3.7	The Structure Puzzle of Water . . . . .	47
<b>4</b>	<b>Methods</b>	<b>49</b>
4.1	Synchrotron Measurements . . . . .	49
4.1.1	X-ray Scattering . . . . .	49
4.1.2	X-ray Absorption Spectroscopy . . . . .	51
4.2	Free-electron Laser Measurements . . . . .	52
4.2.1	Self-amplified Spontaneous Emission . . . . .	54
4.2.2	Laser Operation Parameters . . . . .	56
4.2.3	Droplet Dispensers . . . . .	57
<b>5</b>	<b>Analysis</b>	<b>65</b>
5.1	Analysis of Diffraction Patterns . . . . .	65
5.1.1	Corrections to Synchrotron Data . . . . .	65
5.1.2	Corrections to the Cornell-SLAC Pixel Array Detector . . . . .	67
5.1.3	Sorting of Scattering Data . . . . .	70
5.1.4	Analysis of Structure Factors and PCFs . . . . .	75
5.1.5	Overlap in Data Sets from SSRL and LCLS . . . . .	81
5.2	Analysis of X-ray Spectra . . . . .	85
5.2.1	Lambert-Beer's Law . . . . .	85
5.2.2	Fluence Dependence Model for X-ray Emission Decay Channel . . . . .	86
5.3	Temperature Calibration . . . . .	90
5.3.1	Knudsen Theory of Evaporation . . . . .	90
5.3.2	Molecular Dynamics Simulations of Evaporative Cooling . . . . .	92
5.3.3	Thermodynamic Parameters and Their Effect on Temperature Estimates . . . . .	92

5.3.4	Delay of Evaporative Cooling from Focusing Gas . . . . .	97
5.3.5	Mass Loss from Evaporation . . . . .	98
5.3.6	Temperature Gradients in Droplets Due to Evaporative Cooling . . . . .	98
5.3.7	Experimental Temperature Calibration . . . . .	100
5.4	Ice Analysis . . . . .	106
5.4.1	Extraction of the Ice Nucleation Rate . . . . .	106
5.4.2	Classical Nucleation Theory and Fragility . . . . .	107
<b>6</b>	<b>Summary of Results</b>	<b>111</b>
6.1	X-ray Scattering of Liquid Water . . . . .	111
6.1.1	Paper I – Medium-range Order in Water is a Fingerprint of Tetrahedral Structures . . . . .	111
6.1.2	Paper II – Accelerated Abundance of Tetrahedral Structures in Deeply Supercooled Water . . . . .	114
6.2	X-ray Scattering and Absorption Spectroscopy of Ice . . . . .	119
6.2.1	Paper III – Homogeneous Ice Nucleation in Deeply Supercooled Water . . . . .	119
6.2.2	Paper IV – The Heterogeneous Structure of Crystalline Ice Films . . . . .	123
6.3	X-ray Emission Spectroscopy of Liquid Water . . . . .	126
6.3.1	Paper V – Valence-excited State Reabsorption of X-ray Emission at High Fluences . . . . .	126
6.3.2	Paper VI – Assessing the Lone-pair Emission in Deeply Supercooled Water . . . . .	129
<b>7</b>	<b>Concluding Remarks and Outlook</b>	<b>131</b>
	<b>Populärvetenskaplig sammanfattning</b>	<b>135</b>
	<b>Acknowledgements</b>	<b>137</b>
	<b>References</b>	<b>139</b>



# List of Abbreviations

1D	one-dimensional
2D	two-dimensional
3D	three-dimensional
ADU	analog-to-digital unit
AES	Auger electron spectroscopy
AEY	Auger electron yield
AFF	atomic form factor
ALS	Advanced Light Source
ASIC	application-specific integrated circuit
ASW	amorphous solid water
BL	beam line
BW	bandwidth
CB	conduction band
CNT	classical nucleation theory
CSPAD	Cornell-SLAC pixel array detector
CXI	Coherent X-ray Imaging
DFT	density functional theory
DOS	density of states
FEL	free-electron laser
FWHM	full width at half maximum
GDVN	gas-dynamic virtual nozzle
H-bond	hydrogen bond
HDA	high-density amorphous
eHDA	expanded HDA
uHDA	unannealed HDA
HDL	high-density liquid
HGW	hyperquenched glassy water
HOMO	highest occupied molecular orbital
LCLS	Linac Coherent Light Source
LDA	low-density amorphous
LDL	low-density liquid

LHS	left-hand side
LJE	Liquid Jet Endstation
LLCP	liquid-liquid critical point
MAFF	modified atomic form factor
MD	molecular dynamics
ML	monolayer
MSF	molecular scattering factor
ND	neutron diffraction
PCF	pair-correlation function
PES	photoemission spectroscopy
PMT	photomultiplier tube
psi	pounds per square inch
RDF	radial distribution function
dRDF	difference RDF
RIXS	resonant inelastic x-ray scattering
RHS	right-hand side
RJ	Rayleigh jet
RMS	root-mean-square
SASE	self-amplified spontaneous emission
SAXS	small-angle x-ray scattering
SEM	scanning electron microscope
SEY	secondary electron yield
SI	international system of units
SLAC	Stanford Linear Accelerator Center
SSE	Surface Science Endstation
SSRL	Stanford Synchrotron Radiation Lightsource
STXM	scanning transmission x-ray microscopy
SXR	Soft X-ray Materials Science
UHV	ultra-high vacuum
UV	ultraviolet
VB	valence band
VFT	Vogel-Fulcher-Tammann
VHDA	very high-density amorphous
WAXS	wide-angle x-ray scattering
XAS	x-ray absorption spectroscopy
XES	x-ray emission spectroscopy
XPS	x-ray photoelectron spectroscopy
XRD	x-ray diffraction
XRS	x-ray Raman scattering

# Chapter 1

## Introduction

Water is one of the most abundant substances on earth's surface and thus critical in numerous geological, ecological, biological, and chemical processes, such as life itself as we know it. Access to clean water is also one of the most challenging questions in the coming century, as climate change begins to play a role combined with an ever increasing world population. Crucially for our existence, water exhibits numerous anomalous physical properties\* compared to other liquids, such as maximum in density at 277 K [1] and unusually large isobaric molar heat capacity with a minimum at 308 K [2]. Many of these anomalous properties are directly related to the structure of the liquid, which is governed by the intermolecular network of hydrogen bonds (H-bonds) that is present in liquid water. To understand water's anomalous behavior, it is therefore crucial to study the structure of the liquid and how it changes with temperature.

For example, the maximum in density is caused by a balance between thermal expansion and the structural change in the H-bonded network. Each water molecule in the liquid can form two donating and two accepting H-bonds with a length of  $\sim 2.8 \text{ \AA}$  [3–5] in a near-tetrahedral arrangement. This structure is energetically favored and leads to an open network with only four nearest neighbors at low temperature, compared to twelve in a close-packed solid. As the liquid is heated toward 277 K, collapse of the open network due to increased thermal motion will favor structures with more neighbors and increase the density. Thermal expansion, on the other hand, is present in any liquid and decreases the density as the liquid is heated. Above the density maximum, the thermal expansion rules over the structural collapse and the density increases as the temperature is decreased, but below 277 K,

---

\*A very ambitious webpage by Martin Chaplin dedicated to water lists 80 anomalous properties to date, and the list is constantly growing. For a current list, see: <http://www1.lsbu.ac.uk/water/anmlies.html>

the structural change in the H-bonded network dominates and the density decreases upon cooling further.

Many anomalous properties become dramatically enhanced upon supercooling water below its melting point  $T_m$ . In particular, extrapolations of the thermal expansion coefficient [6], isothermal compressibility [7], and molar heat capacity at constant pressure [2] can all be fitted with a power law that appears to diverge at a temperature  $T_S$  of 228 K. Experiments on pure bulk water in this temperature regime have so far been impossible; water crystallization occurs rapidly below the homogeneous nucleation temperature  $T_h = 232$  K [8–10] and above the spontaneous crystallization temperature  $T_x \approx 160$  K [11], leading to a “no-man’s land” devoid of experimental results. Water crystallization has been inhibited by confinement in nanoporous silica [12, 13] or in nanometer-sized droplets evaporatively cooled *in vacuo* [14–16], enabling temperatures below 232 K to be attained. However, such measurements rely on nanoscopic volumes of liquid water where the interaction with the confining surfaces makes the relevance to bulk water unclear [17].

X-ray scattering is the technique of choice when studying the local structure of condensed matter, because the pair-correlation function (PCF) of the material can be directly obtained through a Fourier transform of the structure factor (explained in detail in Section 2.3.3). It was used in Paper II to probe the local structure of liquid water over a broad temperature range, extending from 227 K to 339 K. To reach the lowest temperatures, micron-sized droplets had to be evaporatively cooled *in vacuo* and probed by a single pulse from a free-electron laser (FEL) to avoid x-ray induced crystallization. Above the melting point, synchrotron radiation was utilized in Paper I to perform wide-angle x-ray scattering (WAXS) with high energy resolution, focusing on the fine structure of the derived PCF.

One of the advantages of x-ray scattering is that it is very sensitive to translational order present in crystalline materials, in which case the technique is usually referred to as x-ray diffraction (XRD). The translational order results in sharp Bragg peaks in the diffraction pattern, clearly distinguishable from the diffuse scattering of disordered materials. By classifying individual shots as either water or ice, homogeneous ice nucleation could be studied simultaneously to the structure of supercooled water, from which the nucleation rate was extracted in Paper III.

The crystalline phase was also studied separately using x-ray spectroscopy, which has the power to reveal the atom-specific electronic structure. The electronic structure is of great interest in chemical physics, because orbital overlap and hybridization determine the formation of chemical bonds. X-ray emission spectroscopy (XES) and x-ray absorption spectroscopy (XAS) are complementary techniques that study the occupied and unoccupied states, respectively. O K-edge XAS was performed on ice crystallites on a BaF<sub>2</sub> sur-



---

face and between  $\text{Si}_3\text{N}_4$  windows using synchrotron radiation. This is the topic of Paper IV. To gain further insight on the electronic structure of the H-bonded network in water, XES was utilized at the O  $K$ -edge to probe liquid water down to 222 K in a setup similar to the x-ray scattering experiments at the FEL. This is the topic of Papers V-VI.

This thesis combines the studies presented in Papers I-VI to describe a unified picture of the structure of water as a function of temperature and how it is related to the observed nucleation rate and its resulting crystalline phase. A preparatory description of the underlying theory is given, after which the methods necessary to perform the experiments and analyze the results are introduced. Finally, the main results of the studies are summarized and conclusions are drawn.



## Chapter 2

# Light-matter Interactions

This chapter deals with various aspects of light-matter interactions, specifically focusing on x-rays interacting with atoms. First, we will present the cross-sections of various scattering channels and review the theory necessary to analyze scattering data of liquid water and crystalline ice as well as interpret and understand their structures. Second, we will present the spectroscopic techniques used in this thesis and summarize their principles for transitions between different states of the system. Although these theories are general, using x-rays instead of electromagnetic radiation of longer wavelength enables electronic transitions involving core levels in the system. Furthermore, elastic scattering of x-rays is governed by Thomson scattering, which enables us to study diffraction between atomic distances. Thus, Rayleigh scattering of electromagnetic radiation by particles much smaller than the wavelength of the light does not have to be considered. We will also touch briefly on inelastic Compton scattering, which has to be accounted for when extracting the elastically scattered intensity at high momentum transfer.

Neither the theoretical framework presented in this chapter, nor its derivations, are by no means original work done by myself, but it is based on the scientific development during the past centuries that has formed modern physics. Whenever previous knowledge is used, the source where it has been acquired is cited. In all equations I will use SI units unless specified. I will also ignore spin throughout this thesis, excluding the vast research field of magnetic order and spin transitions, since it is not related to the work presented in Papers I-VI.

## 2.1 Photoelectric Effect

The photoelectric effect was first observed by Hertz in 1887 [18], who studied how ultraviolet (UV) light would affect the spark length in a coil with a spark gap. The UV light ionized atoms in the air through the photoelectric effect, creating photoelectrons with a characteristic kinetic energy, which is the basis for the technique described in Section 2.5.2. As the source of electromagnetic radiation was placed behind a glass panel, which absorbs UV light, the spark length was decreased. When glass was replaced by quartz, which does not absorb UV radiation, no such decrease in spark length was observed.

Several experiments by Thomson and Lenard, among many others [19], reproduced the photoelectric effect, which could not be explained by classical electrodynamics that treats light as electromagnetic waves formulated through Maxwell's equations [20]. The kinetic energy of the emitted photoelectrons depended on the frequency of the absorbed radiation as if light was quantized into particles with an energy proportional to the frequency of the radiation. In contrast, classical electrodynamics expected the emitted electrons to have an energy proportional to the intensity of the radiation, of which the electron energy was independent.

Einstein solved this paradox through the particle-wave duality by introducing photons as the discrete quanta of light [21], which earned him the Nobel Prize in 1921. The particle-wave duality led to the development of quantum mechanics, revolutionizing the view on matter. We observe its presence in this thesis, in which elastic scattering is well described by the wave character of light. Core-level spectroscopy, on the other hand, relies on the particle character of light, and is most conveniently described through absorption and emission of photons.

## 2.2 Absorption and Scattering Cross-sections

There are many scattering channels, some of which include absorption and emission of photons, described in Section 2.4. There are also channels in which the photon is scattered elastically, leaving the state of the electronic system unchanged, or it is scattered inelastically, but the photon only loses part of its energy. To visualize the relative importance of various processes, the total cross-section for O is shown in Fig. 2.1 as a function of photon energy of the incoming radiation [22, 23]. Below 100 keV, which is the photon energy range relevant to this thesis, the total cross-section has significant contributions from absorption or photoelectric excitations (including core-level spectroscopies described in Section 2.4), denoted  $\sigma_a$ , coherent or elastic scattering (described in detail in Section 2.3), denoted  $\sigma_{cs}$ , and incoherent or inelastic scattering (including Compton scattering described in Section 2.2.3),

denoted  $\sigma_{is}$ . We see that  $\sigma_a$  dominates and is highly energy-dependent. The sharp edge visible at  $\sim 540$  eV is the O  $K$ -edge associated with photoelectric excitations from the  $1s$  orbital, which enables new scattering channels, but as the photon energy increases far above the edge,  $\sigma_a$  decreases strongly. Except at the  $K$ -edge, the elastic scattering cross-section is fairly insensitive to photon energy up to  $\sim 10$  keV, which we will understand in terms of Thomson scattering in the next section. Compton scattering increases strongly with photon energy and is therefore important when conducting scattering experiments at high photon energies.

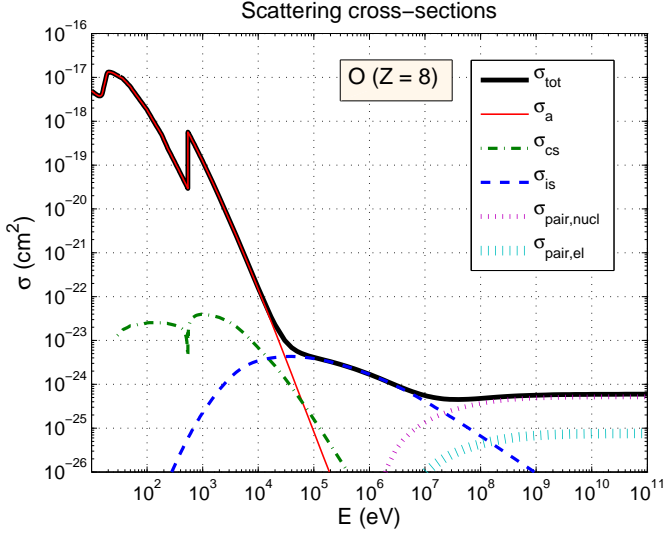


**Figure 2.1:** Scattering cross-sections for an oxygen atom ( $Z = 8$ ) as a function of photon energy. The total cross-section (black thick solid line) is partitioned into five contributions: the absorption cross-section  $\sigma_a$  (red thin solid line); the coherently scattered cross-section  $\sigma_{cs}$ , including Thomson scattering (green dash-dotted line); the incoherently scattered cross-section  $\sigma_{is}$ , including Compton scattering (blue dashed line); the cross-section for pair production in nuclear field  $\sigma_{pair,nucl}$  (magenta thin dotted line); the cross-section for pair production in electric field  $\sigma_{pair,el}$  (cyan thick dotted line). The tabulated data was taken from Refs. [22,23].

### 2.2.1 Thomson Scattering

The elastic scattering off an electron predicted by classical electrodynamics is often called Thomson scattering, which is the foundation for XRD and the elastic scattering theory described in Section 2.3. In the low-energy limit, the

electric field of the electromagnetic radiation accelerates the electron (along the field), which causes the electron in turn to emit radiation. For unpolarized incident radiation (with equal part horizontally and vertically polarized light) the Thomson differential scattering cross-section is [20]

$$\frac{d\sigma_t}{d\Omega} = \left( \frac{e^2}{4\pi\epsilon_0 m_e c^2} \right)^2 \frac{1 + \cos^2 \theta}{2}, \quad (2.1)$$

where  $e$  is the electric charge,  $\epsilon_0$  is the vacuum permittivity,  $m_e$  is the electron mass,  $c$  is the speed of light in vacuum, and  $\theta$  is the scattering angle. The expression inside the parenthesis has the unit of length and is known as the classical electron radius  $r_e = 2.82 \times 10^{-13}$  cm. The  $\theta$ -dependence of  $d\sigma_t/d\Omega$  is solely determined by the polarization of the incoming radiation, *e.g.* see Eq. (5.2) that corrects for the linear polarization in Papers II-III. If we integrate Eq. (2.1) over all solid angles, we obtain the total Thomson scattering cross-section of an electron, which is  $\sigma_t = \frac{8\pi}{3} r_e^2$ . Thus, the coherent cross-section  $\sigma_{cs}$  of an atom may be described in terms of  $\sigma_t$  and a function that takes the correlation between different electrons in the atom into account, resulting in that [24]

$$\sigma_{cs} = \sigma_t |f(0, E)|^2 = \frac{8\pi}{3} r_e^2 |f(0, E)|^2, \quad (2.2)$$

where  $f(\mathbf{q}, E)$  is the energy-dependent atomic form factor (AFF) described by Eq. (2.24) and discussed in detail in Section 2.3.2. Except for the energy-dispersive correction to  $f(\mathbf{q}, E)$ , both  $\sigma_t$  and  $\sigma_{cs}$  in Eq. (2.2) are independent of photon energy, which appears to be consistent with  $\sigma_{cs}$  of O in Fig. 2.1 up to  $\sim 10$  keV. In fact, Thomson scattering can be viewed as Rayleigh scattering off electrons and is a valid approximation when the wavelength of the light is much longer than  $r_e$  and we can assume that the electron can take up the momentum transfer  $\mathbf{q}$  without changing its energy.

### 2.2.2 Absorption

In contrast to Thomson scattering, the absorption cross-section of an atom is highly energy-dependent and can be written as [24]

$$\sigma_a = 2r_e hc \frac{\Im(f(0, E))}{\hbar\omega}, \quad (2.3)$$

where  $h$  is Planck's constant,  $\hbar = h/2\pi$ ,  $\omega$  is the angular frequency, and  $\Im$  denotes the imaginary part of the AFF. Tabulated data of the real part  $\Re(f(0, E))$  and the imaginary part  $\Im(f(0, E))$  are available from Henke *et al.* [23] and can be accessed using the X-ray Database\* maintained by the

---

\*[http://henke.lbl.gov/optical\\_constants/](http://henke.lbl.gov/optical_constants/)

Center for X-ray Optics at Lawrence Berkeley National Laboratory, which is a useful resource to calculate x-ray interactions with matter. Another useful resource is the X-ray Data Booklet<sup>†</sup> [25], which includes similar information condensed into a portable format, perfect for synchrotron experiments.

### 2.2.3 Compton Scattering

When the photon energy  $E = \hbar\omega$  starts to approach the same order of magnitude as the rest energy of the electron of  $m_e c^2 = 511 \text{ keV}$ , momentum conservation will result in inelastic scattering. Considering a photon that scatters at a scattering angle  $\theta$ , the momentum transfer from the scattered photon must be taken up by the electron, making it recoil. The recoil will increase the energy of the electron according to the relativistic energy-momentum relation, which in turn reduces the photon energy. Assuming that the momentum of the electron is effectively zero and the electron therefore is sufficiently close to being at rest (and can be described by only its rest energy), the shift in wavelength upon scattering becomes [26]

$$\lambda' - \lambda = \frac{h}{m_e c} (1 - \cos \theta), \quad (2.4)$$

where  $\lambda$  is the wavelength of the incoming photon,  $\lambda'$  is the wavelength of the scattered photon,  $\theta$  is the scattering angle, and  $h/m_e c = 2.43 \times 10^{-2} \text{ \AA}$  is the Compton wavelength of the electron. We see that the wavelength shift is zero at  $\theta = 0$  and at most twice the Compton wavelength. For the synchrotron radiation used in Paper I with a photon energy of 17 keV and corresponding  $\lambda = 0.73 \text{ \AA}$ , the shift at the maximum scattering angle of  $\sim 135^\circ$  becomes  $\sim 0.04 \text{ \AA}$ , resulting in that the scattered x-rays should have a photon energy of  $\sim 16 \text{ keV}$ . In reality, it is only the valence electrons that scatter as free electrons with such large Compton wavelength. The inner-shell electrons of oxygen are tightly bound to the atom, thus making the whole atom recoil and reducing the Compton wavelength by a factor of  $\sim 29000$  compared to that of a free electron.

The Klein-Nishina formula [27] gives the differential cross-section of photons scattered from a single free electron and connects Thomson scattering and Compton scattering. The differential cross-section is calculated using quantum electrodynamics as [27]

$$\frac{d\sigma_{kn}}{d\Omega} = \alpha^2 r_c^2 P(\hbar\omega, \theta)^2 \frac{[P(\hbar\omega, \theta) + P(\hbar\omega, \theta)^{-1} - 1 + \cos^2(\theta)]}{2}, \quad (2.5)$$

where  $\alpha$  is the fine structure constant,  $r_c = \hbar/m_e c = r_e/\alpha$  is the reduced

<sup>†</sup><http://xdb.lbl.gov/xdb.pdf>

Compton wavelength of the electron, and

$$P(\hbar\omega, \theta) = \frac{1}{1 + (\hbar\omega/m_e c^2)(1 - \cos(\theta))} \quad (2.6)$$

is the ratio of photon energy before and after scattering. For  $\hbar\omega \ll m_e c^2$ ,  $P(\hbar\omega, \theta) \approx 1$  and Eq. (2.5) reduces to that of Thomson scattering stated in Eq. (2.1). Note that the photon energy  $\hbar\omega'$  of the scattered photon depends only on the photon energy  $\hbar\omega$  of the incoming photon and the scattering angle  $\theta$ , and can thus be calculated by  $\hbar\omega' = \hbar\omega P(\hbar\omega, \theta)$ .

## 2.3 Elastic Scattering Theory

This section deals with elastic scattering theory and derives the relevant equations to extract structural information from elastic scattering. Although the original references have been cited, parts are identical to previously published work by me [28], which can be accessed for a more comprehensive derivation of some steps.

We define the problem as consisting of an incoming plane wave  $e^{i\mathbf{k}\cdot\mathbf{r}}$ , describing a flow of particles with wave vector  $\mathbf{k}$  and magnitude  $k$ , scattered through a scattering potential  $U(\mathbf{r})$  with the result of an outgoing spherical wave  $e^{ikr}/r$ . We measure the system in the far-field regime where it can be shown that there is no interference between the incoming and outgoing waves [29, 30]. We also assume there is no multiple scattering, and thus only study the kinematical case where scattering off an aggregate of particles (such as a molecule or crystal) can be regarded as scattering off a single compound particle. In such a system the corresponding wave function must, in the center of mass frame of the system, have the asymptotic form

$$\psi \approx e^{i\mathbf{k}\cdot\mathbf{r}} + a(\theta) \frac{e^{ikr}}{r}, \quad (2.7)$$

where  $a(\theta)$  is the scattering amplitude, which depends on the scattering angle  $\theta$ . It can be shown that  $a(\theta)$  is uniquely defined by the scattering potential  $U(\mathbf{r})$  [29], which contains information about the ensemble of particles studied.

### 2.3.1 Born Approximation

To better understand this connection, we regard  $U(\mathbf{r})$  as a perturbation of first order; this is also known as the Born approximation [29], which is valid when either

$$|U| \ll \frac{\hbar^2}{ms^2}, \quad (2.8)$$



or

$$|U| \ll \frac{\hbar v}{s}, \quad (2.9)$$

where  $|U|$  is the order of magnitude of the potential in the range where it is significant,  $s$  is the range of action of the potential,  $m$  is the reduced mass of the particles,  $\hbar$  is the reduced Planck constant, and  $v$  is the relative velocity with respect to the particles. Hence, Eq. (2.8) is fulfilled for sufficiently small scattering potentials and Eq. (2.9) is true when the particles are sufficiently fast. We seek

$$\psi = \psi^{(0)} + \psi^{(1)}, \quad (2.10)$$

where the asymptotic form of  $\psi^{(0)} = e^{i\mathbf{k}\cdot\mathbf{r}}$  corresponds to an incident particle with wave vector  $\mathbf{k} = \mathbf{p}/\hbar$ , *i.e.* the wave function when no scattering is present. This is the solution to Schrödinger's equation of free motion

$$\nabla^2 \psi^{(0)} + k^2 \psi^{(0)} = 0, \quad (2.11)$$

where  $k = p/\hbar = \sqrt{2mE}/\hbar$  is the magnitude of the wave vector of the particle and  $\hat{H} = \hat{H}_0 = -\frac{\hbar^2}{2m}\nabla^2$  is the Hamiltonian of the free particle. The equation for the correction  $\psi^{(1)}$  to the wave function is to first order at large distances (neglecting the compound particle wave packet)

$$\nabla^2 \psi^{(1)} + k^2 \psi^{(1)} = \frac{2mU(\mathbf{r})}{\hbar^2} \psi^{(0)}, \quad (2.12)$$

where  $\hat{H} = \hat{H}_0 + \hat{V} = -\frac{\hbar^2}{2m}\nabla^2 + U(\mathbf{r})$  is the Hamiltonian of the particle in the scattering field. The solution to Eq. (2.12) is known from electrodynamics [20], where Green's functions are used to solve equations of the kind

$$(\nabla^2 + k^2) \psi(\mathbf{r}) = -4\pi f(\mathbf{r}), \quad (2.13)$$

where  $f(\mathbf{r})$  is an arbitrary function of space  $\mathbf{r}$ . The corresponding Green's function satisfies

$$(\nabla^2 + k^2) G_k(\mathbf{r}, \mathbf{r}') = -4\pi\delta(\mathbf{r} - \mathbf{r}'), \quad (2.14)$$

where  $\delta(\mathbf{r} - \mathbf{r}')$  is the Dirac delta function [29]. The solution to Eq. (2.13) can then be written as

$$\psi(\mathbf{r}) = \psi_0(\mathbf{r}) + \int G_k(\mathbf{r}, \mathbf{r}') f(\mathbf{r}') d\mathbf{r}', \quad (2.15)$$

where  $d\mathbf{r}' = dx'dy'dz'$  and  $\psi_0(\mathbf{r}) = \psi^{(0)}(\mathbf{r})$  is the solution to the homogeneous equation. The desired Green's function can be found if we Fourier transform Eq. (2.14) and solve for the representation of  $G_k(\mathbf{r}, \mathbf{r}')$  in momentum

space  $\mathbf{p}$  and  $\mathbf{r}'$ . To retrieve  $G_k(\mathbf{r}, \mathbf{r}')$ , we inverse Fourier transform with respect to  $\mathbf{p}$  and find that the solutions only depend on  $R = |\mathbf{r} - \mathbf{r}'|$  and can be written as retarded (+) and advanced (-) Green's functions, so that

$$G_k(\mathbf{r}, \mathbf{r}') = G_k^\pm(R) = \frac{e^{\pm i k R}}{R}. \quad (2.16)$$

In terms of retarded potentials, we then obtain

$$\psi(\mathbf{r}) = e^{i\mathbf{k} \cdot \mathbf{r}} - \frac{m}{2\pi\hbar^2} \int U(\mathbf{r}') e^{i\mathbf{k} \cdot \mathbf{r}'} \frac{e^{i k R}}{R} d\mathbf{r}'. \quad (2.17)$$

Taking the origin at the scattering center and accounting for the limited range of  $U(\mathbf{r}')$ , we have  $\mathbf{r} \gg \mathbf{r}'$  at large distances  $\mathbf{r}$  from the origin. We define  $\mathbf{n}'$  as the unit vector along  $\mathbf{r}$  and Taylor expand  $R = |\mathbf{r} - \mathbf{r}'|$  around  $r = |\mathbf{r}|$ :

$$\begin{aligned} R &= \sqrt{(\mathbf{r} - \mathbf{r}')^2} = \sqrt{r^2 - 2\mathbf{r} \cdot \mathbf{r}' + r'^2} = r \sqrt{1 - 2\frac{\mathbf{r}' \cdot \mathbf{n}'}{r} + \frac{r'^2}{r^2}} = \\ &= r \left[ 1 - \frac{\mathbf{r}' \cdot \mathbf{n}'}{r} + \frac{r'^2}{2r^2} - \frac{1}{4} \left( \frac{\mathbf{r}' \cdot \mathbf{n}'}{r} \right)^2 + \dots \right] \approx r - \mathbf{r}' \cdot \mathbf{n}' \end{aligned} \quad (2.18)$$

Thus, Eq. (2.17) becomes

$$\begin{aligned} \psi &\approx e^{i\mathbf{k} \cdot \mathbf{r}} - \frac{m}{2\pi\hbar^2} \int U(\mathbf{r}') e^{i\mathbf{k} \cdot \mathbf{r}'} \frac{e^{i k (r - \mathbf{r}' \cdot \mathbf{n}')}}{r - \mathbf{r}' \cdot \mathbf{n}'} d\mathbf{r}' \approx \\ &\approx e^{i\mathbf{k} \cdot \mathbf{r}} - \frac{m}{2\pi\hbar^2} \int U(\mathbf{r}') e^{i\mathbf{k} \cdot \mathbf{r}'} \frac{e^{i k (r - \mathbf{n}' \cdot \mathbf{r}')}}{r} d\mathbf{r}' = \\ &= \left\{ \mathbf{k}' = k\mathbf{n}' \right\} = e^{i\mathbf{k} \cdot \mathbf{r}} - \frac{m}{2\pi\hbar^2} \frac{e^{i k r}}{r} \int U(\mathbf{r}') e^{i(\mathbf{k} - \mathbf{k}') \cdot \mathbf{r}'} d\mathbf{r}'. \end{aligned} \quad (2.19)$$

We define the momentum transfer  $\mathbf{q} = \mathbf{k}' - \mathbf{k}$  and compare with Eq. (2.7) to obtain the scattering amplitude (replacing  $\mathbf{r}' = \mathbf{r}$ )

$$a(\mathbf{q}) = -\frac{m}{2\pi\hbar^2} \int U(\mathbf{r}) e^{-i\mathbf{q} \cdot \mathbf{r}} d\mathbf{r}. \quad (2.20)$$

Thus, the scattering amplitude has been simplified to a three-dimensional (3D) Fourier transform of the scattering potential. For photon scattering, the potential is very local ( $s$  is very small in Eq. (2.8)-(2.9)), verifying the validity of perturbation theory, and the scattering potential  $U(\mathbf{r})$  can therefore be estimated by the total electron density  $\rho(\mathbf{r})$  of the system. As only relative differences in the scattering amplitude are of practical interest, we choose to consider

$$A(\mathbf{q}) = \int \rho(\mathbf{r}) e^{-i\mathbf{q} \cdot \mathbf{r}} d\mathbf{r}, \quad (2.21)$$

where the constant factor in (2.20) has been omitted. It should be noted that if the quantity transformed is real, as is usually the case with electron densities, the Fourier transform is invariant under sign transformations of the variable. In scattering, this is known as Friedel's law. As a consequence, the scattered intensity is invariant when  $\mathbf{q} \rightarrow -\mathbf{q}$ , since it is defined as

$$I(\mathbf{q}) \equiv I_0 \frac{d\sigma}{d\Omega} = I_0 |a(\mathbf{q})|^2 \propto |A(\mathbf{q})|^2, \quad (2.22)$$

where  $I_0$  is the intensity of the incident beam,  $d\sigma$  is the differential cross-section and  $d\Omega$  is an element of solid angle. This will be the theoretical basis for scattering throughout the rest of this thesis.

### 2.3.2 X-ray Scattering of Solids

When studying condensed matter, it is useful to refine the general expression in Eq.(2.21) and define various cases of scattering. If  $\rho(\mathbf{r})$  is the electron density of an atom  $\rho_{atom}(\mathbf{r})$ , we obtain

$$f_0(\mathbf{q}) = \int \rho_{atom}(\mathbf{r}) e^{-i\mathbf{q} \cdot \mathbf{r}} d\mathbf{r}, \quad (2.23)$$

where  $f_0(\mathbf{q})$  is the AFF. It should be noted that a general expression for the AFF is [31]

$$f(\mathbf{q}, E) = f_0(\mathbf{q}) + f'(E) + if''(E), \quad (2.24)$$

where it is seen that a dispersion correction with real and complex parts contributes to the total AFF. This energy-dispersive correction is only important in resonant scattering when the energy of the incident photons approaches absorption edges in the atom. As non-resonant scattering is considered in Papers I-III, the correction will be ignored from now on so that  $f(\mathbf{q}) = f_0(\mathbf{q})$ .

For  $q = 0$  Eq. (2.23) reduces to an integral of  $\rho_{atom}(\mathbf{r})$  over all space, which gives the total number of electrons  $Z$  of the atom. Hence, AFFs increase with atomic number. In the case of water, this implies that the x-ray scattering is dominated by the scattering off electrons located around the oxygen atom. Since non-interacting closed-shell atoms are spherically symmetric,  $\rho_{atom}(\mathbf{r}) = \rho_{atom}(r)$  and the angular degrees of freedom in Eq.(2.23) can be integrated out. We choose spherical coordinates with  $0 \leq r < \infty$  being the radius from the center of the atom,  $0 \leq \theta \leq \pi$  being the polar angle with  $\theta = 0$  defined in the direction of  $\mathbf{q}$ , and  $0 \leq \phi \leq 2\pi$  being the azimuthal

angle, which gives

$$\begin{aligned}
 f(\mathbf{q}) &= \int_0^\infty \int_0^\pi \int_0^{2\pi} \rho_{atom}(r) e^{-i\mathbf{q}\cdot\mathbf{r}} r^2 \sin\theta \, d\phi d\theta dr = \\
 &= 2\pi \int_0^\infty \int_0^\pi \rho_{atom}(r) e^{-iqr \cos\theta} r^2 \sin\theta \, d\theta dr = \\
 &= \left\{ \begin{array}{l} x = \cos\theta \\ \frac{dx}{d\theta} = -\sin\theta \end{array} \right\} = 2\pi \int_0^\infty r^2 \rho_{atom}(r) \int_{-1}^1 e^{-iqr x} \, dx dr = \\
 &= 2\pi \int_0^\infty r^2 \rho_{atom}(r) \frac{e^{-iqr} - e^{iqr}}{-iqr} \, dr = 4\pi \int_0^\infty r^2 \rho_{atom}(r) \frac{\sin qr}{qr} \, dr.
 \end{aligned} \tag{2.25}$$

Thus,  $f(\mathbf{q}) = f(q)$  is a real quantity (assuming  $\rho_{atom}$  is real) that only depends on the magnitude of the momentum transfer.

If the system consists of many particles, interference of photons scattered by different particles has to be considered. We define our electron density as a sum of  $N$  particle densities

$$\rho(\mathbf{r}) = \sum_{k=1}^N \rho_k(\mathbf{r} - \mathbf{r}_k), \tag{2.26}$$

where  $\rho_k$  is the electron density of particle  $k$  centered at  $\mathbf{r}_k$ . Keeping in mind the definition of the AFF, the scattering amplitude of the system then becomes

$$\begin{aligned}
 A(\mathbf{q}) &= \int \rho(\mathbf{r}) e^{-i\mathbf{q}\cdot\mathbf{r}} \, d\mathbf{r} = \sum_{k=1}^N \int \rho_k(\mathbf{r} - \mathbf{r}_k) e^{-i\mathbf{q}\cdot\mathbf{r}} \, d\mathbf{r} = \\
 &= \left\{ \begin{array}{l} \mathbf{r}' = \mathbf{r} - \mathbf{r}_k \\ \frac{d\mathbf{r}'}{d\mathbf{r}} = 1 \end{array} \right\} = \sum_{k=1}^N \int \rho_k(\mathbf{r}') e^{-i\mathbf{q}\cdot(\mathbf{r}'+\mathbf{r}_k)} \, d\mathbf{r}' = \\
 &= \sum_{k=1}^N e^{-i\mathbf{q}\cdot\mathbf{r}_k} \int \rho_k(\mathbf{r}') e^{-i\mathbf{q}\cdot\mathbf{r}'} \, d\mathbf{r}' = \sum_{k=1}^N f_k(\mathbf{q}) e^{-i\mathbf{q}\cdot\mathbf{r}_k},
 \end{aligned} \tag{2.27}$$

where  $f_k(\mathbf{q})$  is the form factor of particle  $k$ . Thus, the scattered intensity of the system is

$$\begin{aligned}
 I(\mathbf{q}) &\propto |A(\mathbf{q})|^2 = \sum_{k=1}^N f_k(\mathbf{q}) e^{-i\mathbf{q}\cdot\mathbf{r}_k} \sum_{l=1}^N f_l^*(\mathbf{q}) e^{i\mathbf{q}\cdot\mathbf{r}_l} = \\
 &= \sum_{k=1}^N \sum_{l=1}^N f_k(\mathbf{q}) f_l^*(\mathbf{q}) e^{-i\mathbf{q}\cdot(\mathbf{r}_k - \mathbf{r}_l)} = \\
 &= \sum_{k=1}^N |f_k(\mathbf{q})|^2 + \sum_{k=1}^N \sum_{l \neq k}^N f_k(\mathbf{q}) f_l^*(\mathbf{q}) e^{-i\mathbf{q}\cdot(\mathbf{r}_k - \mathbf{r}_l)}.
 \end{aligned} \tag{2.28}$$

The first term is the sum of the scattering by the independent particles and is known as the incoherent part of the scattered intensity. The second term comes from interference of x-ray photons scattered by different particles and is known as the coherent part of the scattered intensity. The coherent part of the scattered intensity requires the coherence length<sup>‡</sup> of the x-ray beam to cover all the particles; if the coherence length of the x-ray beam is smaller than the distance between particles, they are scattered incoherently, *i.e.* their scattered intensities are summed up instead of their scattering amplitudes.

If the sample consists of  $N$  identical spherical atoms, then  $f_k(\mathbf{q}) = f_l^*(\mathbf{q}) \equiv f(q)$  and Eq. (2.28) is reduced to

$$\begin{aligned} I(\mathbf{q}) &\propto \sum_{k=1}^N f(q)^2 + \sum_{k=1}^N \sum_{l \neq k}^N f(q)f(q)e^{-i\mathbf{q} \cdot (\mathbf{r}_k - \mathbf{r}_l)} = \\ &= Nf(q)^2 + f(q)^2 \sum_{k=1}^N \sum_{l \neq k}^N e^{-i\mathbf{q} \cdot (\mathbf{r}_k - \mathbf{r}_l)} = \\ &= Nf(q)^2 \left( 1 + \frac{1}{N} \sum_{k=1}^N \sum_{l \neq k}^N e^{-i\mathbf{q} \cdot (\mathbf{r}_k - \mathbf{r}_l)} \right). \end{aligned} \quad (2.29)$$

We define the structure factor  $S(\mathbf{q})$  of the solid as

$$S(\mathbf{q}) \equiv \frac{1}{N} \sum_{k=1}^N \sum_{l \neq k}^N e^{-i\mathbf{q} \cdot (\mathbf{r}_k - \mathbf{r}_l)}, \quad (2.30)$$

which is the coherent part of the scattered intensity normalized by the incoherent part. The decomposition of  $I(\mathbf{q})$  performed in Eq. (2.29) implies that  $S(\mathbf{q})$  is a real quantity.

It should be noted that the finite sizes of the sample and x-ray beam have to be taken into account, which makes  $S(\mathbf{q})$  a convolution of the shape transform of the illuminated macroscopic object and the bulk structure. This will be discussed more in Section 2.3.4 that focuses on XRD of crystalline materials, where it is possible to separate the contribution of the shape transform from that of the bulk structure. For now, we will ignore the shape transform of the macroscopic object, because the object's large size makes its Fourier transform extend to very low  $q$  and therefore does not notably alter the broad continuous correlations of  $S(\mathbf{q})$  associated with disordered matter.

### 2.3.3 X-ray Scattering of Liquids

We now make the assumption that the sample is macroscopically homogeneous and isotropic, as is the case for liquids. From the isotropy follows that

<sup>‡</sup>The coherence length is defined as the propagation distance over which a coherent wave maintains its coherence and interference patterns are visible.

the scattered intensity must be independent of the orientation of the sample. Hence, we must consider the intensity expressed in Eq. (2.28) but averaged over all orientations such that

$$I(q) = \langle I(\mathbf{q}) \rangle \propto \langle |A(\mathbf{q})|^2 \rangle = \quad (2.31)$$

$$= \left\langle \sum_{k=1}^N |f_k(\mathbf{q})|^2 \right\rangle + \left\langle \sum_{k=1}^N \sum_{l \neq k}^N f_k(\mathbf{q}) f_l^*(\mathbf{q}) e^{-i\mathbf{q} \cdot (\mathbf{r}_k - \mathbf{r}_l)} \right\rangle,$$

where  $\langle x \rangle = \frac{1}{4\pi} \int x \, d\Omega$  denotes an ensemble average integrated over all solid angles  $d\Omega = \sin \theta \, d\theta \, d\phi$  (in real space, not reciprocal space). If the sample consists of  $N$  identical spherical atoms, then similar to Eq. (2.29)-(2.30), we find that the structure factor  $S(q)$  of the liquid becomes

$$S(q) = \langle S(\mathbf{q}) \rangle = \frac{1}{N} \left\langle \sum_{k=1}^N \sum_{l \neq k}^N e^{-i\mathbf{q} \cdot (\mathbf{r}_k - \mathbf{r}_l)} \right\rangle, \quad (2.32)$$

which only depends on the magnitude of the momentum transfer. Eq. (2.32) can be simplified further as a consequence of the isotropy of the system. We define the vector  $\mathbf{r}_{kl} = \mathbf{r}_k - \mathbf{r}_l$  with the polar angle  $\theta$  taken as the angle between  $\mathbf{q}$  and  $\mathbf{r}_{kl}$  and perform the angular integration in spherical polar coordinates

$$S(q) = \frac{1}{N} \left\langle \sum_{k=1}^N \sum_{l \neq k}^N e^{-i\mathbf{q} \cdot (\mathbf{r}_k - \mathbf{r}_l)} \right\rangle = \frac{1}{N} \sum_{k=1}^N \sum_{l \neq k}^N \langle e^{-i\mathbf{q} \cdot \mathbf{r}_{kl}} \rangle = \quad (2.33)$$

$$= \frac{1}{4\pi N} \sum_{k=1}^N \sum_{l \neq k}^N \int_0^\pi \int_0^{2\pi} e^{-iqr_{kl} \cos \theta} \sin \theta \, d\phi \, d\theta =$$

$$= \frac{1}{2N} \sum_{k=1}^N \sum_{l \neq k}^N \int_0^\pi e^{-iqr_{kl} \cos \theta} \sin \theta \, d\theta = \frac{1}{N} \sum_{k=1}^N \sum_{l \neq k}^N \frac{\sin qr_{kl}}{qr_{kl}}.$$

We see that  $S(q)$  has reduced to sums of sinc functions that are solely determined by the magnitudes  $q$  and  $r_{kl}$ . Eq. (2.33) was first derived by Peter Debye [32] and is thus known as the Debye scattering formula.

To quantify the relationship between  $S(q)$  and the local structure in real space, we now turn to the useful concept of the PCF  $g(r)$ , which describes the average probability to find an atom at a radial distance  $r$  from another atom in the sample. Hence, the average number of neighboring atoms  $n(r_1, r_2)$  between  $r_1$  and  $r_2$  from an average atom in the sample can be obtained by integrating

$$n(r_1, r_2) = \int_{r_1}^{r_2} 4\pi r^2 \rho_0 g(r) \, dr. \quad (2.34)$$

The integrand in Eq. (2.34) is sometimes called the radial distribution function (RDF) [3]. We define  $g(r)$  microscopically as [33]

$$\rho_0 g(r) \equiv \frac{1}{N} \left\langle \sum_{k=1}^N \sum_{l \neq k}^N \delta(\mathbf{r} - \mathbf{r}_k + \mathbf{r}_l) \right\rangle, \quad (2.35)$$

where  $\rho_0$  is the average density in the sample and  $\delta(\mathbf{r})$  is the Dirac delta function. Noting that

$$\sum_{k=1}^N e^{-i\mathbf{q} \cdot \mathbf{r}_k} = \int \sum_{k=1}^N \delta(\mathbf{r} - \mathbf{r}_k) e^{-i\mathbf{q} \cdot \mathbf{r}} d\mathbf{r}, \quad (2.36)$$

we rewrite  $S(q)$  as a function of  $g(r)$

$$\begin{aligned} S(q) &= \frac{1}{N} \left\langle \sum_{k=1}^N \sum_{l \neq k}^N e^{-i\mathbf{q} \cdot (\mathbf{r}_k - \mathbf{r}_l)} \right\rangle = \quad (2.37) \\ &= \frac{1}{N} \left\langle \int \int \sum_{k=1}^N \sum_{l \neq k}^N \delta(\mathbf{r} - \mathbf{r}_k) \delta(\mathbf{r}' + \mathbf{r}_l) e^{-i\mathbf{q} \cdot (\mathbf{r} + \mathbf{r}')} d\mathbf{r} d\mathbf{r}' \right\rangle = \\ &= \int \left\langle \frac{1}{N} \sum_{k=1}^N \sum_{l \neq k}^N \delta(\mathbf{r} - \mathbf{r}_k + \mathbf{r}_l) \right\rangle e^{-i\mathbf{q} \cdot \mathbf{r}} d\mathbf{r} = \rho_0 \int g(r) e^{-i\mathbf{q} \cdot \mathbf{r}} d\mathbf{r} = \\ &= \rho_0 \int (g(r) - 1) e^{-i\mathbf{q} \cdot \mathbf{r}} d\mathbf{r} + \rho_0 \int e^{-i\mathbf{q} \cdot \mathbf{r}} d\mathbf{r} = \\ &= \rho_0 \int_0^\infty \int_0^\pi \int_0^{2\pi} (g(r) - 1) e^{-i\mathbf{q} \cdot \mathbf{r}} r^2 \sin \theta d\phi d\theta dr + \rho_0 \delta(q) = \\ &= 2\pi \rho_0 \int_0^\infty r^2 (g(r) - 1) \int_0^\pi e^{-i\mathbf{q} \cdot \mathbf{r}} \sin \theta d\theta dr + \rho_0 \delta(q) = \\ &= 4\pi \rho_0 \int_0^\infty r^2 (g(r) - 1) \frac{\sin qr}{qr} dr + \rho_0 \delta(q). \end{aligned}$$

The Dirac delta function only gives a contribution at  $q = 0$  and can therefore be ignored, since forward scattering cannot be measured experimentally (due to the incident beam). Hence, we are left with

$$qS(q) = 4\pi \rho_0 \int_0^\infty r (g(r) - 1) \sin qr dr \quad (2.38)$$

and we see that  $S(q)$  is related to  $g(r)$  directly through a sine transform. We define the sine transform and its inverse uniquely as [34]

$$f_s(q) = \int_0^\infty g_s(r) \sin qr dr \quad (2.39)$$

$$g_s(r) = \frac{2}{\pi} \int_0^\infty f_s(q) \sin qr dq \quad (2.40)$$

Applying Eq. (2.40) on Eq. (2.38), we get

$$\frac{2}{\pi} \int_0^\infty q S(q) \sin qr \, dq = 8\rho_0 \int_0^\infty \int_0^\infty r (g(r) - 1) \sin qr \, dr \sin qr \, dq = \quad (2.41)$$

$$= 8\rho_0 \frac{\pi}{2} r (g(r) - 1) = 4\pi\rho_0 r (g(r) - 1). \quad (2.42)$$

By multiplying both sides by  $r$  and moving over the last term, we end up with the final expression reported in Paper I

$$4\pi\rho_0 r^2 g(r) = 4\pi r^2 \rho_0 + \frac{2r}{\pi} \int_0^\infty q S(q) \sin qr \, dq. \quad (2.43)$$

Eq. (2.38) and Eq. (2.43) are the basis for interpreting the local structure from scattering data and vice versa. Combining Eq. (2.31)-(2.32) we can obtain  $S(q)$  from the measured  $I(q)$  for monoatomic liquids as

$$S(q) = \frac{KI(q)/N - f(q)^2}{f(q)^2}, \quad (2.44)$$

where  $K$  is a proportionality constant. Since  $N$  is unknown experimentally, the effective proportionality constant  $K_{norm} = K/N$  has to be determined by one of the two methods described in Section 5.1.4.

The procedure described above can be generalized from monoatomic liquids to multicomponent systems. When several atom types are present, the partial structure factor  $S_{\alpha\beta}(q)$  for each atom pair  $\alpha$  and  $\beta$  is [35]

$$q S_{\alpha\beta}(q) = c_\alpha c_\beta 4\pi\rho_0 \int_0^\infty r (g_{\alpha\beta}(r) - 1) \sin qr \, dr, \quad (2.45)$$

where  $c_\alpha = N_\alpha/N$  is the number concentration of the  $\alpha$  component,  $c_\beta = N_\beta/N$  is the number concentration of the  $\beta$  component, and  $g_{\alpha\beta}(r)$  is the  $\alpha$ - $\beta$  PCF, *i.e.* the atomic number density of the  $\beta$  component at a radial distance  $r$  from an average  $\alpha$  atom in the sample. The partial PCFs (and consequently the partial structure factors) are symmetric with respect to the two components, which means that  $g_{\alpha\beta}(r) = g_{\beta\alpha}(r)$ . We can write the total structure factor as a sum of the partial structure factors [35]

$$S(q) = \frac{\sum_\alpha \sum_\beta c_\alpha c_\beta f_\alpha(q) f_\beta(q) S_{\alpha\beta}(q)}{\sum_\alpha c_\alpha f_\alpha(q)^2}. \quad (2.46)$$

Note that the squared AFFs in the nominator and the denominator of Eq. (2.44) are no longer equivalent, since the general expressions in Eq. (2.28) are different for the incoherent and coherent part. The first term in Eq. (2.28) is  $N \sum_\alpha c_\alpha |f_\alpha|^2$  as only self-scattering is considered in the incoherent part, whereas mixed terms exist in the coherent part of the scattered intensity, often



approximated by  $(\sum_{\alpha} c_{\alpha} f_{\alpha})^2$ . Different normalizations have been proposed, suggesting that the self-scattering should be used for both terms [36].

It is possible to modify the AFFs so that they better describe the bonding occurring in molecules, resulting in the modified atomic form factors (MAFFs) [37]

$$f'(q) = \left(1 + \alpha_i e^{-q^2/2\delta_i^2}\right) f_i(q), \quad (2.47)$$

where  $\alpha_i$  accounts for redistribution of charge and  $\delta$  can be tuned to realistically represent the enhanced delocalization of the valence electrons due to covalent bonding.

Finally, we can also define a molecular scattering factor (MSF) by once again using Eq. (2.21)

$$F(q) = \int \rho_{molecule}(\mathbf{r}) e^{-i\mathbf{q}\cdot\mathbf{r}} d\mathbf{r}. \quad (2.48)$$

As previously, we average the scattering over all orientations (in real space) and obtain approximately an equivalent expression to Eq. (2.44) but for the MSF [38]

$$S(q) = \frac{KI(q)/N - \langle F(q)^2 \rangle}{\langle F(q) \rangle^2}, \quad (2.49)$$

where  $\langle F(q)^2 \rangle$  is the average scattering from one water molecule, whereas  $\langle F(q) \rangle^2$  is the scattering of a water molecule oriented randomly with respect to another water molecule at the origin.  $\langle F(q) \rangle^2$  is referred to as the spherical part of  $\langle F(q)^2 \rangle$  and has been found to be similar to  $\langle F(q)^2 \rangle$  for water [38]. This is used in Paper I to obtain the intermolecular  $S(q)$ , resulting in that  $g(r)$  then corresponds to the average probability of finding a water molecule at a radial distance  $r$  from another water molecule in the sample. Strictly speaking, Eq. (2.49) is only valid for a monomolecular liquid in which there are no orientational correlations between neighboring molecules [3], but due to  $\langle F(q)^2 \rangle \approx \langle F(q) \rangle^2$  in water, it has been found to be a fair approximation [38] even though angular correlations are expected to be strong.

### 2.3.4 X-ray Diffraction of Crystals

The translational order present in crystals imposes strict constraints for the allowed values of  $S(\mathbf{q})$ . Fourier analysis of the crystal lattice reveals that only a momentum transfer  $\mathbf{q}$  equal to the reciprocal lattice vector  $\mathbf{G}_{hkl}$  yields constructive interference between crystal planes [39]. The reciprocal lattice vector is conveniently described by its Miller indices  $(hkl)$  so that

$$\mathbf{G}_{hkl} = h\mathbf{b}_1 + k\mathbf{b}_2 + l\mathbf{b}_3, \quad (2.50)$$

where  $\mathbf{b}_1$ ,  $\mathbf{b}_2$ , and  $\mathbf{b}_3$  are the lattice unit vectors in reciprocal space. Thus, we only have to sum over the atomic distances in the unit cell when we calculate  $S(\mathbf{q})$  from Eq. (2.30). The allowed crystal reflections and their relative strength are determined by the specific lattice and its basis.

A finite-sized crystal (or illumination) can be viewed as an infinite crystal lattice multiplied by some crystal shape or beam profile. In the limit of an infinite lattice, the Bragg reflection associated with a crystal plane ( $hkl$ ) becomes infinitely sharp and converges toward a Dirac delta function at  $\mathbf{G}_{hkl}$ . Hence, it is possible to evaluate the convolution of the shape transform and the bulk structure directly, as the Fourier transform of the bulk structure will only contribute at a single point and the distribution around  $\mathbf{G}_{hkl}$  will be that of the shape transform. If the coherence length and the focus of the x-ray beam are large enough, this can be utilized to study the crystal shape or even extract its 3D lattice strain or distortions [40]. We investigated whether this technique could be employed to the ice shots presented in Paper III, but unfortunately the detector resolution was too low to resolve the fringes of the shape transform.

## 2.4 Core-level Spectroscopy

Core-level spectroscopy is frequently used to study the nature of chemical bonds. The valence orbitals are responsible for ionic, covalent, and metallic bonds, as well as polarization resulting in electrostatic dipole interactions. Hence, it may seem contradictory to use inner-shell orbitals to study the chemical state of an atom. However, core electrons provide unique possibilities to study the local electronic and geometric properties centered around one atomic site [41, 42]. The core-level binding energies are sensitive to the chemical environment, whereas the absorption and emission cross-sections of x-rays reveal the symmetry-resolved energy distribution for unoccupied and occupied valence orbitals, respectively.

The various flavors of core-level spectroscopy are schematically pictured in Fig. (2.2). As the name suggests, it involves the creation and decay of a core hole, and can be classified into two classes related to the former (XAS; XPS, see definition below) and the latter (XES; AES, see definition below). First, a core hole is created when absorbing an x-ray photon. Depending on the energy of the photon, it can either result in a core excitation, leaving the molecule in an excited state, or a core ionization, resulting in an ion and a photoelectron. In XAS, the absorption cross-section is measured as a function of excitation energy. This can be done directly by measuring the transmission of x-rays through a very thin sample, or by monitoring the radiative (fluorescence yield) or non-radiative (electron yield) decay channels, which

have been shown to be proportional to the absorption cross-section [24]. In x-ray photoelectron spectroscopy (XPS), the photoelectrons created upon ionization at a known excitation energy are detected and their kinetic energy is measured, usually by bending their path in a hemispherical spectrometer at known bias, from which the binding energy of the core level can be extracted.

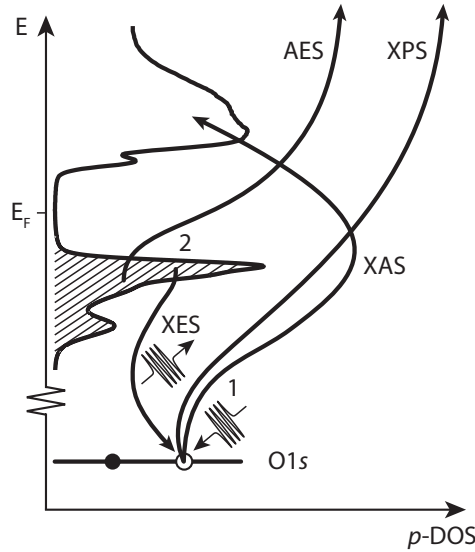


**Figure 2.2:** Schematic illustration of core-level spectroscopy applied to water showing electron energy on the  $y$ -axis and  $p$ -projected density of states (DOS) on the  $x$ -axis. Note that the oxygen core level is of  $s$ -character. The incoming and outgoing photons are shown as thin oscillating arrows, whereas the electron transfers are marked by thick curved arrows. Occupied electron states are shaded black. The core-level processes can be divided into two steps. First, a photon is absorbed (1) and a core electron is excited into the unoccupied DOS (XAS) above the Fermi energy  $E_F$  or a photoelectron (XPS) is ejected into vacuum. Second, a valence electron decays to fill the core hole (2) and a photon (XES) or a second valence electron (AES) is emitted.

The created core hole is highly unstable and the system generally relaxes after a few femtoseconds. For  $O\ 1s$ , the core hole has a lifetime  $\tau = \hbar/\Gamma \sim 3\text{--}4\text{ fs}$  [43, 44], where  $\Gamma$  is the full width at half maximum (FWHM) of the Lorentzian peak shape of the core-excited state (in the energy representation), which has been determined from the spectroscopic  $1s \rightarrow \pi^*$  transition in  $O_2$  [43, 44]. The relaxation can either occur radiatively or non-radiatively. In the former case, an x-ray photon is emitted with an energy corresponding to the energy difference for the decay, which is utilized in XES, where the emitted x-rays are energy resolved using a grating and recorded on a detector.

In the latter case, on the other hand, the released energy is used to emit a secondary valence electron. This process is known as Auger decay, and Auger electron spectroscopy (AES) is measured in similar fashion to XPS. Both XPS and AES rely on the detection of emitted electrons. Thus, the techniques are highly surface sensitive, since the mean-free path of an electron is only  $\sim 1$  nm at 400 eV [24]. A key difference between XPS and AES is that the spectral features studied in XPS do not depend on the electronic binding energy (see Section 2.5.2), whereas the spectral features studied in AES do not depend on the kinetic energy of the photoelectron. Hence, the relative energy positions of peaks from core-level ionizations and Auger decay change as a function of excitation energy. The radiative decay measured in XES is much less surface sensitive, since the attenuation length of soft x-rays in water is about  $5 \mu\text{m}$  at 400 eV (below the absorption edge) and  $\sim 500$  nm at 550 eV (above the O K-edge) [23].

## 2.5 Quantum Description of Light

The interaction of electromagnetic radiation with electrons differs fundamentally for elastic scattering and spectroscopy. As touched upon in Section 2.1, the spectroscopic processes are most conveniently described by quantizing the electromagnetic field. Here, we therefore present a more general approach than what was necessary to describe elastic scattering in Section 2.3.

We consider a non-relativistic electron interacting with a monochromatic plane wave described by its vector potential  $\mathbf{A}$  and scalar potential  $\phi$ . In analogy with classical mechanics, the interaction can be introduced as an external field into Schrödinger's equation by describing the kinetic energy through the generalized momentum [29], resulting in that  $\hat{\mathbf{p}} \rightarrow \hat{\mathbf{p}} - \frac{e}{c}\mathbf{A}$ . We choose the Coulomb gauge by setting  $\vec{\nabla} \cdot \mathbf{A} = 0$  and  $\phi = 0$  (only relative potentials are of importance), which ensures that the plane of the wave is transverse to the direction of propagation [45]. Furthermore, we quantize the electromagnetic field by replacing the classical vector potential  $\mathbf{A}$  by the operator  $\hat{\mathbf{A}}$ . Hence, the Hamiltonian of the total system is [29, 45]

$$\hat{H} = \frac{1}{2m_e} \left( \hat{\mathbf{p}} - \frac{e}{c}\hat{\mathbf{A}} \right)^2 + \sum_{\mathbf{k}, \lambda_p} \hbar \omega_k \left( \hat{a}_{\mathbf{k}, \lambda_p}^\dagger \hat{a}_{\mathbf{k}, \lambda_p} + \frac{1}{2} \right), \quad (2.51)$$

where  $m_e$  is the mass of the electron,  $e$  is the charge (negative for an electron),  $c$  is the speed of light in vacuum,  $\hat{\mathbf{p}} = -i\hbar\vec{\nabla}$  is the generalized momentum operator,  $\hbar$  is the reduced Planck constant,  $\omega_k = kc$  is the angular frequency of the light,  $\hat{a}_{\mathbf{k}, \lambda_p}$  and  $\hat{a}_{\mathbf{k}, \lambda_p}^\dagger$  are the annihilation and creation operators, respectively, of a photon with wave vector  $\mathbf{k}$  and polarization direction  $\lambda_p$ , and

$\hat{\mathbf{A}}$  is the Hermitian vector potential operator given by [45,46]

$$\hat{\mathbf{A}} = \sum_{\mathbf{k}, \lambda_p} \sqrt{\frac{\hbar}{2\omega_k V \epsilon_0}} \left[ \hat{a}_{\mathbf{k}, \lambda_p} \vec{\epsilon}_{\mathbf{k}, \lambda_p} e^{i\mathbf{k} \cdot \mathbf{r}} + \hat{a}_{\mathbf{k}, \lambda_p}^\dagger \vec{\epsilon}_{\mathbf{k}, \lambda_p} e^{-i\mathbf{k} \cdot \mathbf{r}} \right], \quad (2.52)$$

where  $\epsilon_0$  is the vacuum permittivity,  $\vec{\epsilon}_{\mathbf{k}, \lambda_p}$  is the polarization unit vector in the transverse plane (if  $\mathbf{k} \parallel \vec{e}_z$ ,  $\lambda_p = 1, 2$  corresponds to  $\vec{\epsilon}_{\mathbf{k}, 1} \parallel \vec{e}_x$  and  $\vec{\epsilon}_{\mathbf{k}, 2} \parallel \vec{e}_y$ ), and  $V$  is an arbitrarily large normalization volume [45] (evoked to make  $\mathbf{k}$  discrete). The first term in Eq. (2.51) corresponds to the Hamiltonian of the free electron  $\hat{H}_e = \hat{\mathbf{p}}^2/2m_e$  and the interaction  $\hat{V}$  with the field, whereas the second term describes the quantization of the field itself. We see that the Hamiltonian of the electromagnetic radiation  $\hat{H}_{em}$  corresponds to the Hamiltonian of a sum of independent harmonic quantum oscillators for each  $\mathbf{k}$  and  $\lambda_p$ . If  $\hat{H}_{em}$  acts on the vacuum state  $|0\rangle$ , the first term will not contribute (since  $\hat{a}_{\mathbf{k}, \lambda_p}|0\rangle = 0$ ) and the zero-point energy can be defined as the expectation value

$$E_0 \equiv \langle 0 | \hat{H}_{em} | 0 \rangle = \sum_{\mathbf{k}, \lambda_p} \frac{\hbar\omega_k}{2} \langle 0 | 0 \rangle = \sum_{\mathbf{k}, \lambda_p} \frac{\hbar\omega_k}{2}. \quad (2.53)$$

Although this quantity is technically infinite as the sum is over all possible wave vectors, it does not impose a problem as only relative energies are of physical importance, and we can in a similar way to the scalar potential set  $E_0 = 0$ .

Turning back to the first term in Eq. (2.51), the Coulomb gauge ensures that  $\hat{\mathbf{p}}$  and  $\hat{\mathbf{A}}$  commute, so that the two cross terms of the square are identical. Thus, we can write the interaction Hamiltonian as

$$\hat{V} = -\frac{e}{m_e c} \hat{\mathbf{p}} \cdot \hat{\mathbf{A}} + \frac{e^2}{2m_e c^2} \hat{\mathbf{A}}^2. \quad (2.54)$$

The interaction between the electromagnetic field and an arbitrary electronic system can now be investigated. Suppose at time  $t = 0$  the total system (including the photons) is in an initial state  $|n^{(0)}\rangle$ , corresponding to a stationary state of the unperturbed system whose time-dependent wave function  $\Psi_n^{(0)}(t) = e^{-\frac{i}{\hbar} E_n^{(0)} t} |n^{(0)}\rangle$  is known. The interacting system does not in general have stationary states (if  $\hat{V}$  is time dependent), but we can treat the interaction as a time-dependent perturbation and partition the Hamiltonian  $\hat{H} = \hat{H}_0 + \hat{V}$ , where  $\hat{H}_0$  is the Hamiltonian of the unperturbed system (including the Hamiltonian of the non-interacting electrons and photons) and  $\hat{V}$  is defined in Eq. (2.54) with the vector potential operator given in Eq. (2.52). Expanding the time-dependent wave function  $\Psi(t)$  in the stationary states of the unperturbed system

$$\Psi(t) = \sum_m c_{mn}(t) \Psi_m^{(0)}(t), \quad (2.55)$$

the time-dependence (beyond what is expected for the unperturbed system) will be contained in the time-dependence of the expansion coefficients  $c_{mn}(t)$ , which to first order are [29]

$$c_{mn}(t) = \delta_{mn} - \frac{i}{\hbar} \int_0^t e^{i\omega_{mn}t'} \langle m^{(0)} | \hat{V} | n^{(0)} \rangle dt', \quad (2.56)$$

where  $\omega_{mn} = (E_m^{(0)} - E_n^{(0)})/\hbar$ , and  $E_m^{(0)}$  and  $E_n^{(0)}$  are the energies of the  $m$ th and  $n$ th stationary state, respectively. As the matrix element  $\langle m^{(0)} | \hat{V} | n^{(0)} \rangle$  does not depend on time and can be moved outside of the integral, it is straight-forward to perform the integration in Eq. (2.56), yielding

$$\begin{aligned} \int_0^t e^{i\omega_{mn}t'} dt' &= \frac{e^{i\omega_{mn}t} - 1}{i\omega_{mn}} = \frac{(e^{i\omega_{mn}t/2})^2 - 1}{i\omega_{mn}} = \\ &= \frac{\left(\cos\left(\frac{\omega_{mn}t}{2}\right) + i\sin\left(\frac{\omega_{mn}t}{2}\right)\right)^2 - \cos^2\left(\frac{\omega_{mn}t}{2}\right) - \sin^2\left(\frac{\omega_{mn}t}{2}\right)}{i\omega_{mn}} = \\ &= \frac{2i\cos\left(\frac{\omega_{mn}t}{2}\right)\sin\left(\frac{\omega_{mn}t}{2}\right) - 2\sin^2\left(\frac{\omega_{mn}t}{2}\right)}{i\omega_{mn}} = \\ &= \frac{\cos\left(\frac{\omega_{mn}t}{2}\right) + i\sin\left(\frac{\omega_{mn}t}{2}\right)}{\omega_{mn}/2} \sin\left(\frac{\omega_{mn}t}{2}\right) = \frac{e^{i\omega_{mn}t/2}}{\omega_{mn}/2} \sin\left(\frac{\omega_{mn}t}{2}\right). \end{aligned} \quad (2.57)$$

Using Eq. (2.57) in Eq. (2.56) and taking the square modulus, the transition probability to a stationary state  $m \neq n$  becomes

$$|c_{mn}(t)|^2 = \left| \langle m^{(0)} | \hat{V} | n^{(0)} \rangle \right|^2 \frac{4 \sin^2\left(\frac{\omega_{mn}t}{2}\right)}{\hbar^2 \omega_{mn}^2}. \quad (2.58)$$

Notice that the first root of  $\frac{\sin^2(\omega_{mn}t/2)}{\omega_{mn}^2}$  occurs at  $\omega_{mn}t/2 = \pi$ , or  $\omega_{mn} = 2\pi/t$ , indicating there is a non-zero probability of making transitions to states with energy  $\omega_{mn} \neq 0$ . Hence, energy is not conserved for arbitrary  $t$ , but as  $t$  increases,  $\frac{\sin^2(\omega_{mn}t/2)}{\omega_{mn}^2}$  becomes sharper and narrower, in agreement with the uncertainty relation  $\Delta E \Delta t \geq \hbar/2$ . We make use of the representation of the Dirac delta function [45]

$$\delta\left(\frac{\omega_{mn}}{2}\right) = \lim_{t \rightarrow \infty} \frac{\sin^2\left(\frac{\omega_{mn}t}{2}\right)}{\pi t (\omega_{mn}/2)^2} = \lim_{t \rightarrow \infty} \frac{4 \sin^2\left(\frac{\omega_{mn}t}{2}\right)}{\pi t \omega_{mn}^2} \quad (2.59)$$

and rewrite Eq. 2.58 for  $t \rightarrow \infty$ , noting that  $\delta(\omega_{mn}/2) = 2\hbar\delta(E_m^{(0)} - E_n^{(0)})$ , as

$$|c_{mn}(t \rightarrow \infty)|^2 = \lim_{t \rightarrow \infty} \left| \langle m^{(0)} | \hat{V} | n^{(0)} \rangle \right|^2 \frac{2\pi t \delta(E_m^{(0)} - E_n^{(0)})}{\hbar}. \quad (2.60)$$

We see that the transition probability per unit time, *i.e.*  $d|c_{mn}(t)|^2/dt$ , does not depend on time for large  $t$ , so that we can write the transition rate  $T_{mn}$  as

$$T_{mn} = \left| \langle m^{(0)} | \hat{V} | n^{(0)} \rangle \right|^2 \frac{2\pi\delta(E_m^{(0)} - E_n^{(0)})}{\hbar}. \quad (2.61)$$

Although originally derived by Dirac [47], Eq. (2.61) is often denoted Fermi's "golden rule" [24, 45], and will be the theoretical basis for the core-level spectroscopies considered in this thesis.

In XPS and XAS, an x-ray photon is absorbed, whereas in XES, an x-ray photon is emitted. This imposes restrictions on the initial and final states of the system, denoted  $|n^{(0)}\rangle$  and  $|m^{(0)}\rangle$ , respectively, in Eq. (2.61). (The suffix  $^{(0)}$  denotes that the states are represented in the basis of the unperturbed system, which means that if the final state is not an eigenstate of the unperturbed system, it will be expanded in several  $T_{mn}$  terms with various weights.) We regard the initial state for all three processes as a product state of an electronic eigenstate  $|i\rangle$  and a photon eigenstate  $|n_{\mathbf{k},\lambda_p}\rangle$  that contains  $n$  photons of wave vector  $\mathbf{k}$  and polarization direction  $\lambda_p$ , so that

$$|n^{(0)}\rangle = |i\rangle \times |n_{\mathbf{k},\lambda_p}\rangle. \quad (2.62)$$

The resulting final state must be a product state of an electronic state  $|f\rangle$  and, in XPS and XAS, a photon state  $|n_{\mathbf{k},\lambda_p} - 1\rangle$  where a single photon has been absorbed, so that

$$|m^{(0)}\rangle = |f\rangle \times |n_{\mathbf{k},\lambda_p} - 1\rangle, \quad (2.63)$$

whereas in XES, the photon state is  $|n_{\mathbf{k},\lambda_p} + 1\rangle$ , in which a single photon has been emitted, so that

$$|m^{(0)}\rangle = |f\rangle \times |n_{\mathbf{k},\lambda_p} + 1\rangle. \quad (2.64)$$

Using these definitions for the matrix element  $\langle m^{(0)} | \hat{V} | n^{(0)} \rangle$  in Eq. (2.61), it is possible to separate each term of  $\hat{V}$  into a product of a matrix element for the electronic system and a matrix element for the photon system, where the operators in  $\hat{V}$  have been ordered so that  $\hat{a}_{\mathbf{k},\lambda_p}$  and  $\hat{a}_{\mathbf{k},\lambda_p}^\dagger$  are contained in the matrix element for the photon system and the rest of the operators are contained in the matrix element for the electronic system. Thus, without knowing anything of the eigenstates of the electronic system, we can evaluate the transitions in the photon system that yield a non-zero overlap.

First, we recall that the orthonormality condition for eigenstates in the second quantization results in that the inner product

$$\langle m_{\mathbf{k},\lambda_p} | n_{\mathbf{k}',\lambda'_p} \rangle = \delta_{m,n} \delta_{\mathbf{k},\mathbf{k}'} \delta_{\lambda_p,\lambda'_p}, \quad (2.65)$$

which ensures that the sum in Eq. (2.52) reduces to single elements of wave vector  $\mathbf{k}$  and polarization direction  $\lambda_p$ . This also results in that  $\hat{V}$  must in total annihilate (XAS, XPS) or create (XES) one photon for  $T_{mn}$  to be non-zero.

Second, we order the terms of  $\hat{V}$  after their creation and annihilation operators. The  $\hat{\mathbf{p}} \cdot \hat{\mathbf{A}}$  term from Eq. (2.54) results in one term that contains  $\hat{a}_{\mathbf{k},\lambda_p}$  and one term that contains  $\hat{a}_{\mathbf{k},\lambda_p}^\dagger$ , *i.e.* a net loss and gain of one photon, respectively. The  $\hat{\mathbf{A}}^2$  term from Eq. (2.54) results in one term that contains  $\hat{a}_{\mathbf{k},\lambda_p} \hat{a}_{\mathbf{k},\lambda_p}$ , one term that contains  $\hat{a}_{\mathbf{k},\lambda_p}^\dagger \hat{a}_{\mathbf{k},\lambda_p}^\dagger$ , and one term that contains  $2\hat{a}_{\mathbf{k},\lambda_p}^\dagger \hat{a}_{\mathbf{k},\lambda_p} + 1$  (counted twice, since  $[\hat{a}_{\mathbf{k},\lambda_p}, \hat{a}_{\mathbf{k},\lambda_p}^\dagger] = 1$ ), *i.e.* a net loss of two photons, gain of two photons, and no gain or loss, respectively. We see that it is only the term that contains  $\hat{a}_{\mathbf{k},\lambda_p}$  that will connect the initial and final state in XPS and XAS with non-zero overlap. On the other hand, it is only the term that contains  $\hat{a}_{\mathbf{k},\lambda_p}^\dagger$  that will contribute to XES. The  $2\hat{a}_{\mathbf{k},\lambda_p}^\dagger \hat{a}_{\mathbf{k},\lambda_p} + 1$  term that conserves the number of photons is the basis for Thomson scattering and the elastic scattering theory presented in Section 2.3, whereas the  $\hat{a}_{\mathbf{k},\lambda_p} \hat{a}_{\mathbf{k},\lambda_p}$  and  $\hat{a}_{\mathbf{k},\lambda_p}^\dagger \hat{a}_{\mathbf{k},\lambda_p}^\dagger$  terms have no physical significance [48]. Instead, it is the  $\hat{\mathbf{p}} \cdot \hat{\mathbf{A}}$  term taken to second order that is responsible for double-absorption and double-emission processes [48].

### 2.5.1 Dipole Approximation

In addition to the orthogonality of the photon states connected with the annihilation and creation operators, we can simplify the residual factor  $\vec{\epsilon}_{\mathbf{k},\lambda_p} e^{\pm i\mathbf{k} \cdot \mathbf{r}}$  in Eq. (2.52) further by Taylor expanding the exponential around  $\mathbf{k} \cdot \mathbf{r} = 0$

$$e^{\pm i\mathbf{k} \cdot \mathbf{r}} = 1 \pm i\mathbf{k} \cdot \mathbf{r} + \frac{(\pm i\mathbf{k} \cdot \mathbf{r})^2}{2!} + \dots \quad (2.66)$$

If  $\mathbf{k} \cdot \mathbf{r} \ll 1$ , we can to a good approximation replace the exponential by its first term, known as the dipole approximation [24, 45]. To test the validity of the dipole approximation for O K-edge spectroscopy, we calculate  $\mathbf{k} \cdot \mathbf{r} \leq kr$  by considering soft x-rays with photon energies of 550 eV, corresponding to  $k = \omega_k/c = 0.28 \text{ \AA}^{-1}$ . Following Stöhr [24], we estimate the K-shell diameter from the Bohr radius  $a_0 = 0.53 \text{ \AA}$  and the atomic number  $Z$  as  $r \simeq 2a_0/Z = 0.13 \text{ \AA}$ , so that  $\mathbf{k} \cdot \mathbf{r} \leq 0.037$  and the dipole approximation is well satisfied (to at least 95 %) for the O K-edge. This simplifies the transition matrix element in Eq. (2.61) applied to core-level spectroscopies, so that it can be written as

$$\langle f | \hat{\mathbf{p}} \cdot \vec{\epsilon}_{\mathbf{k},\lambda_p} e^{\pm i\mathbf{k} \cdot \mathbf{r}} | i \rangle \approx \langle f | \hat{\mathbf{p}} \cdot \vec{\epsilon}_{\mathbf{k},\lambda_p} | i \rangle = \vec{\epsilon}_{\mathbf{k},\lambda_p} \cdot \langle f | \hat{\mathbf{p}} | i \rangle, \quad (2.67)$$



where the x-ray polarization unit vector (which is a constant) has been taken out of the integral. Using the commutation relation [29]

$$[\hat{H}_0, \mathbf{r}] = -i\hbar \frac{\partial \hat{H}_0}{\partial \hat{\mathbf{p}}} = -\frac{i\hbar}{m_e} \hat{\mathbf{p}}, \quad (2.68)$$

we can rewrite Eq. (2.67) from its “velocity” form to its “length” form [24]

$$\begin{aligned} \vec{\epsilon}_{\mathbf{k}, \lambda_p} \cdot \langle f | \hat{\mathbf{p}} | i \rangle &= \frac{-m_e}{i\hbar} \vec{\epsilon}_{\mathbf{k}, \lambda_p} \cdot \langle f | \hat{H}_0 \mathbf{r} - \mathbf{r} \hat{H}_0 | i \rangle = \\ &= \frac{im_e}{\hbar} \vec{\epsilon}_{\mathbf{k}, \lambda_p} \cdot \langle f | \left( E_f^{(0)} \right)^* \mathbf{r} - \mathbf{r} E_i^{(0)} | i \rangle = \\ &= \frac{im_e}{\hbar} \left( E_f^{(0)} - E_i^{(0)} \right) \vec{\epsilon}_{\mathbf{k}, \lambda_p} \cdot \langle f | \mathbf{r} | i \rangle = im_e \omega_{fi} \vec{\epsilon}_{\mathbf{k}, \lambda_p} \cdot \langle f | \mathbf{r} | i \rangle, \end{aligned} \quad (2.69)$$

where we have used that  $\hat{H}_0$  is Hermitian and its eigenvalues are real. Note that Eq. (2.69) is only valid if  $|i\rangle$  and  $|f\rangle$  are eigenstates of  $\hat{H}_0$ , which we have assumed that  $|i\rangle$  is, but not necessarily  $|f\rangle$ , otherwise they have to be expanded in the eigenstates of  $\hat{H}_0$ , e.g.  $\hat{H}_0 |f\rangle = \sum_g c_g E_g^{(0)} |g\rangle$ . In what follows, we will assume that both  $|i\rangle$  and  $|f\rangle$  are eigenstates of  $\hat{H}_0$ .

The dipole approximation has implications on the selection rules for the transition matrix elements. We utilize group theory and classify the eigenstates  $|i\rangle$  and  $|f\rangle$  by their irreducible representations  $D_i$  and  $D_f$ , respectively, of the symmetry group of the system concerned. Using the “length” form given by the right-hand side (RHS) of Eq. (2.69), we must also classify the operator  $\mathbf{r}$  by the representation  $D_r$  of the same symmetry group. From symmetry arguments [29], it follows that  $\langle f | \mathbf{r} | i \rangle$  is only non-zero if the representation  $D_f \times D_r \times D_i$  of the integrand contains the totally symmetric representation of the symmetry group or, equivalently, the direct product  $D_f \times D_i$  contains  $D_r$ . As the dipole operator transforms as a vector  $\mathbf{r}$  that is antisymmetric with respect to inversion, this results in that the transition matrix element is only non-zero when [49]

- $\Delta J = 0, \pm 1$ , except for  $0 \leftrightarrow 0$ , which is forbidden
- $\Delta M_J = 0, \pm 1$
- $P_f = -P_i$ ,

where  $J$  is the azimuthal quantum number, corresponding to the total angular momentum of the state,  $M_J$  is the magnetic quantum number, corresponding to the projection of the total angular momentum along a given direction, and  $P$  is the parity of the state, either symmetric (known as *gerade*, with  $P_g = 1$ ) or antisymmetric (known as *ungerade*, with  $P_u = -1$ ) with respect to inversion. If we assume the eigenstates  $|i\rangle$  and  $|f\rangle$  can be represented by

a Slater determinant, *i.e.* the antisymmetric version of a product ansatz of independent particles that fulfills the Pauli exclusion principle for fermions, and we assume that the relaxation effects are small, we can simplify the transition matrix element to  $\langle \phi_f | \mathbf{r} | \phi_i \rangle$ , describing the overlap integral between the initial orbital  $\phi_i$  and the final orbital  $\phi_f$  mediated by the dipole operator in its “length” form. Since we have ignored the spin-orbit interaction, the spin quantum number  $\Delta s = 0$  is unaltered, and the general rules for the total angular momentum must therefore describe the change in orbital angular momentum  $l$ . As orbitals with the same  $l$  have the same parity, we finally arrive at the simplified dipole selection rule for the transition matrix element [49, 50]

- $\Delta l = \pm 1$
- $\Delta m_l = 0, \pm 1$

This means that an atomic-like orbital, such as the O 1s core level, must transition to a  $p$ -like orbital with angular momentum  $l = 1$ , imposing selection rules to the core-level spectroscopies. This is especially useful in XAS and XES, where symmetry-resolved information about the unoccupied and occupied valence states, respectively, is achievable.

Although the derivation of the formulas above is almost identical for all core-level spectroscopies (excluding AES, see Section 2.5.5), the final formulas are listed below separately for each spectroscopic technique with some brief comments.

### 2.5.2 X-ray Photoelectron Spectroscopy

The differential cross-section of photoelectrons as a function of their kinetic energy  $E_{kin}$  is proportional to the transition rate  $T_{mn}$  stated in Eq.(2.61) summed over all possible electronic final states  $|f\rangle$ . Using the dipole approximation, we obtain

$$\frac{d\sigma_{XPS}}{d\Omega}(E_{kin}) \propto \sum_f \left| \langle f | \vec{\epsilon}_{\mathbf{k}, \lambda_p} \cdot \hat{\mathbf{p}} | i \rangle \right|^2 \delta(E_f^{(0)} - E_i^{(0)} - \hbar\omega_k + E_{kin}). \quad (2.70)$$

Alternatively, we can express the energy difference of  $|i\rangle$  and  $|f\rangle$  as  $E_f - E_i = E_b + \Phi$ , where  $E_b$  is the binding energy of the core level and  $\Phi$  is the work function. The work function is the energy difference between the vacuum level (*i.e.* the ionization potential where the continuum begins and the photoelectron is no longer bound to the material) and the Fermi energy (*i.e.* the thermodynamic work required to add an electron to the system, coinciding with the energy band in a conductor that has a 50 % probability of being occupied), against which the binding energy usually is measured for

metals. In gas phase, the work function is set to zero and the binding energy is instead measured with respect to the vacuum level.

### 2.5.3 X-ray Absorption Spectroscopy

Similar to XPS, the differential cross-section for photoabsorption as a function of excitation energy  $\hbar\omega_k$  is proportional to the transition rate  $T_{mn}$  stated in Eq. (2.61) summed over all possible electronic final states  $|f\rangle$ . Using the dipole approximation, we obtain

$$\frac{d\sigma_{XAS}}{d\Omega}(\omega_k) \propto \sum_f \left| \langle f | \vec{\epsilon}_{\mathbf{k},\lambda_p} \cdot \hat{\mathbf{p}} | i \rangle \right|^2 \delta(E_f^{(0)} - E_i^{(0)} - \hbar\omega_k). \quad (2.71)$$

### 2.5.4 X-ray Emission Spectroscopy

For XES, we treat the core excitation and the x-ray emission as a two-step process, so that the differential cross-section for photoemission as a function of emission energy  $\hbar\omega_{k'}$  is proportional to the transition rate  $T_{mn}$  stated in Eq. (2.61) summed over all possible electronic final states  $|f\rangle$ . Using the dipole approximation, we obtain

$$\frac{d\sigma_{XES}}{d\Omega}(\omega_{k'}) \propto \sum_f \left| \langle f | \vec{\epsilon}_{\mathbf{k},\lambda_p} \cdot \hat{\mathbf{p}} | i \rangle \right|^2 \delta(E_f^{(0)} - E_i^{(0)} + \hbar\omega_{k'}). \quad (2.72)$$

This is only valid when the core-excited state can be regarded as a quasi-stationary state, independent of its previous history. Thus, it is not valid for resonant XES, in which the x-ray emission yield depends on the excitation energy  $\hbar\omega_k$ . In this case, the core excitation and the x-ray emission should be treated as a one-step process, which can be done by applying perturbation theory to second order. The second order contribution from the  $\hat{\mathbf{p}} \cdot \hat{\mathbf{A}}$  term [48] results in the Kramers-Heisenberg formula [51] relevant for resonant inelastic x-ray scattering (RIXS) [52]

$$\frac{d^2\sigma_{RIXS}}{d\Omega d\omega_{k'}}(\omega_k, \omega_{k'}) \propto \sum_f \left| \sum_g \frac{\langle f | \vec{\epsilon}_{\mathbf{k},\lambda_p} \cdot \hat{\mathbf{p}} | g \rangle \langle g | \vec{\epsilon}_{\mathbf{k}',\lambda_p} \cdot \hat{\mathbf{p}} | i \rangle}{\hbar\omega_k + E_i^{(0)} - E_g^{(0)} + i\Gamma_g/2} \right|^2 \delta(E_f^{(0)} - E_i^{(0)} + \hbar\omega_{k'} - \hbar\omega_k), \quad (2.73)$$

where  $\omega_k$  is the angular frequency of the incoming radiation,  $\omega_{k'}$  is the angular frequency of the outgoing radiation, and  $\Gamma_g$  is the FWHM of the Lorentzian lifetime broadening (in energy) of the intermediate state  $|g\rangle$ . Note that the  $\hat{\mathbf{A}}^2$  term from Eq. (2.54) that is responsible for Thomson scattering and the non-resonant  $\hat{\mathbf{p}} \cdot \hat{\mathbf{A}}$  term taken to 2<sup>nd</sup> order (in which the outgoing

photon is first created, and then the incoming photon is annihilated) have been omitted [52].

### 2.5.5 Auger Electron Spectroscopy

The non-radiative decay studied in AES is governed by different physics compared to the other core-level spectroscopies, although it looks superficially similar to XES with the same initial state (regarding the core excitation and Auger decay as a two-step process). The Auger decay is described by the Coulomb operator, so that  $\hat{V}$  in Eq. (2.61) is proportional to  $\frac{1}{r_{ij}}$ , where  $r_{ij}$  is the distance between the  $i$ th and  $j$ th electron participating in the Auger decay. We also note that the two-hole final state, which can have large correlation effects [53], has no direct relation to the ground state valence structure [42] (compare to XAS and XES, discussed at the end of Section 2.5.1).

We will not derive the differential cross-section probed using AES, since it is not used within this thesis and the Auger decay is only considered in Paper V, but a few remarks can still be made. The ratio between the two major decay channels of the core hole, namely the emission yield and the Auger electron yield (AEY), changes strongly as a function of atomic number  $Z$ . For light elements, such as oxygen, Auger decay dominates strongly with  $\geq 99\%$  of the core holes decaying non-radiatively [24]. As  $Z$  increases, the spatial extent of the outer shells participating in the Auger decay<sup>§</sup> becomes larger and larger, reducing the double-electron overlap with the core level much faster than the single-electron overlap necessary for x-ray emission. Thus, radiative decay of the  $K$ -edge dominates for  $Z > 30$  [24].

Finally, there are several flavors of Auger decay [42]. Normal decay occurs when the excited photoelectron delocalizes prior to the Auger decay, and thus does not affect the kinetic energy of the Auger electron. In contrast, spectator decay occurs when the excited electron is still localized at the core hole and screens the final state, which generally increases the kinetic energy of the Auger electron compared to normal decay [54]. The ratio of the two Auger decays can thus be utilized in “core-hole clock” methods [55–57] to study the charge transfer rate to the surrounding media (given that the core-hole lifetime is known). Participator decay occurs when the excited electron itself decays back to the core level, and can be regarded as resonant photoemission from the valence band (VB) [42].

---

<sup>§</sup>Usually, Auger decay involves  $KLL$ ,  $LMM$ , or  $KVV$  transitions, where the first index is the core level that the electron decays to, and the second and third indices are the electron shells from which one electron decays and one electron is emitted. Except for  $V$  that denotes the valence shell, the other shells follow standard x-ray nomenclature.

# Chapter 3

## Water

This chapter will give an introduction to the water molecule, water's most common condensed phases, the anomalous properties they exhibit, and the various models proposed to explain them. In the end, a brief summary of the results from various structure-sensitive x-ray techniques will be given as background to the experimental work presented later on in this thesis. These studies have not been conducted by myself, but this is merely my summary of the current scientific understanding, as is the rest of this chapter\*.

### 3.1 The Water Molecule

The water molecule consists of two hydrogen atoms and one oxygen atom, in total 10 electrons. The equilibrium O-H bond length is 0.957 Å and H-O-H angle is 104.52° [58]. O is more electronegative than H, resulting in charge transfer toward the O and an equilibrium dipole moment of 1.85 D in the gas phase [59]. The enthalpy of formation from its atomic constituents is −219.337 kcal/mol [58], corresponding to an electronic binding energy of 10 eV/molecule (which excludes the vibrational zero-point energy).

The water molecule exhibits  $C_{2v}$  symmetry, which results in that the ground-state electronic configuration is

$$(1a_1)^2(2a_1)^2(1b_2)^2(3a_1)^2(1b_1)^2,$$

where  $1a_1$  is the localized O 1s core level (*i.e.* as there is only one core level in water, which is highly isolated in energy, there is more or less no hybridization occurring for the O 1s atomic orbital upon forming water), and  $2a_1$  is the inner valence orbital with mainly O 2s character. The outer valence orbitals,

---

\*The exception is the quantum chemical study used to visualize cooperativity in H-bonds in Section 3.2, which has been performed by myself.

responsible for chemical bonding and studied in XAS and XES, are shown in Fig. (3.1). They comprise the bonding  $1b_2$  and  $3a_1$  orbitals, and the non-bonding  $1b_1$  lone-pair orbital. We note that  $1b_1$  has nearly pure O  $2p$  character, and will therefore contribute strongly to the O  $K$ -edge x-ray emission spectrum, following the dipole selection rule in Section 2.5.1. In addition, the lowest unoccupied molecular orbitals consist of the antibonding  $4a_1$  and  $2b_2$  orbitals, both below the ionization threshold (where the continuum begins).

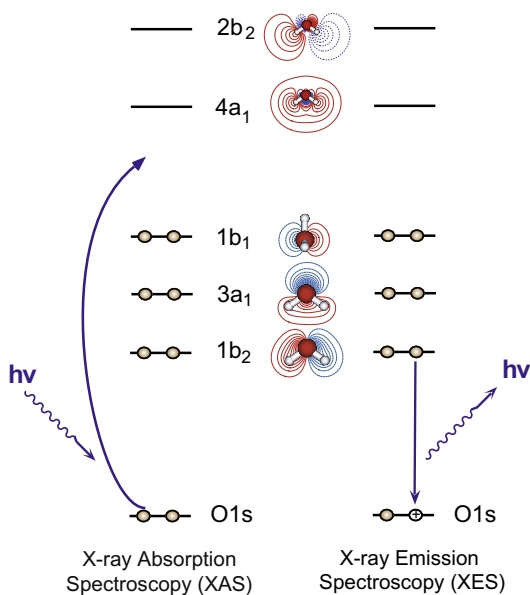


**Figure 3.1:** Molecular orbital diagram depicting the XAS and XES processes in water, reprinted from Ref. [60] with permission from Elsevier. The molecular orbitals (positive phase illustrated by red solid contour lines, negative phase represented by blue dashed contour lines) are named after the irreducible representations of the  $C_{2v}$  point group that they belong to. Thus,  $a_1$  orbitals can be regarded as base functions of the  $A_1$  representation,  $a_2$  orbitals of the  $A_2$  representation, and so on.  $a$  orbitals are symmetric and  $b$  orbitals are antisymmetric with respect to rotations about the principal axis, which is of 2<sup>nd</sup> order in the  $C_{2v}$  point group. The  $a_1$  orbital is completely symmetric (*i.e.* the character of the  $A_1$  representation is 1) with respect to all symmetry transformations.

The non-linear geometry of the water molecule results in that the motion of the water molecule can be partitioned into the motion of the center of mass, including 3 translational and 3 rotational degrees of freedom, and relative

motions within the molecule, including 3 vibrational degrees of freedom. The vibrations can be described by the orthogonal normal modes, corresponding to asymmetrical stretching, symmetrical stretching, and bending motions with characteristic vibrational frequencies of  $\nu_1 = 3755.79 \text{ cm}^{-1}$ ,  $\nu_2 = 3656.65 \text{ cm}^{-1}$ , and  $\nu_3 = 1594.59 \text{ cm}^{-1}$ , respectively [58]. The quantization of the vibrations results in a vibrational zero-point energy of 13.2 kcal/mol or, in terms of wavenumber,  $4634.32 \text{ cm}^{-1}$  [58], compared to  $4503.5 \text{ cm}^{-1}$  that is expected from a harmonic oscillator as in Eq. (2.53).

## 3.2 The Hydrogen Bond

The arguably most important aspect of water molecules in condensed phases is their ability to form H-bonds. The H-bond is the intermolecular interaction between a hydrogen (hence its name) that is partially positively charged and an electronegative element, in this case oxygen. Its bond strength of about 4-6 kcal/mol or  $\sim 0.2 \text{ eV/molecule}$  ( $\sim 10 k_B T$  in water at  $T = 298 \text{ K}$ ) lies in-between that of covalent or ionic bonds of  $\sim 4 \text{ eV}$ , traditionally regarded as (intramolecular) chemical bonds, and that of (intermolecular) van der Waals interactions of  $\sim 0.01 \text{ eV}$ . The exact chemical nature of the H-bond has been intensely debated [61–67], but it is clear that it involves significant changes in the valence electronic structure. For example, the dipole moment in the liquid phase is estimated to increase to 2.6-3.0 D [68, 69], which directly indicates an increased polarization in the molecule. In this thesis, we will interpret the H-bond to involve charge transfer as well as internal polarization. This is in agreement with a detailed study of H-bonding in crystalline ice on Pt(111) [70], in which it was concluded that internal polarization through *s-p* rehybridization in the water molecule and intermolecular charge transfer between the oxygen lone pair and the O-H antibonding orbitals on neighboring molecules stand for  $\frac{1}{3}$  and  $\frac{2}{3}$ , respectively, of the lowering in energy associated with forming an H-bond. The orbital mixing lowers the Pauli repulsion, which is essential for a strong attractive electrostatic interaction [70], and this effect can be observed in the x-ray absorption spectrum, in which the post-edge behaves as an antibonding  $\sigma^*$  resonance of the H-bond [71] (for a detailed investigation of the spectral features, see Paper IV and the references therein). However, the charge accumulated in the middle of the H-bond is 2 orders of magnitude lower than what is observed in the covalent bond in  $\text{H}_2$  and is thus not responsible for the strength of the H-bond [70].

Furthermore, H-bonds in water show a strong cooperativity effect, where successive chains of accepting and donating H-bonds form stronger bonds than that of the isolated water dimer [72]. We can visualize this by performing a simple quantum chemical study in Gaussian 98 using density functional

theory [73,74] (DFT) at the B3LYP [75,76] level of theory with the 6-31G(d,p) basis set. Comparing the results for the geometry-optimized water monomer, dimer, and tetramer, we find that the strength of the H-bond in water is strongly correlated to the O-H bond length of the H-donor, the intermolecular O-O distance, and the frequency shift of the O-H stretching mode attributed to the H-donor. For example, the water tetramer has an average H-bond strength of 6.2 kcal/mol (accounting for the zero-point energy) and an intermolecular O-O distance of 2.758 Å, compared to the water dimer with a H-bond strength of 5.4 kcal/mol and an intermolecular O-O distance of 2.875 Å. The change in O-O distance is almost identical to that of B3LYP calculations in the literature [77] and the cooperativity effect of water clusters has even been measured experimentally [78–80]. At the same time, the O-H bond length of the H-donor increased to 0.983 Å for the trimer and 0.973 Å for the dimer, compared to the 0.965 Å for the non-bonded O-H group (or the water monomer). This resulted in a redshift of the O-H stretching mode (attributed to the H-donor) of  $\sim 110 \text{ cm}^{-1}$  for the water dimer and  $\sim 360 \text{ cm}^{-1}$  for the water trimer, which is in agreement with Badger’s rule [81] that states that the force constant  $k_0 = \omega c$  of the stretch vibration is proportional to  $(r_e - d_{ij})^{-3}$ , where  $r_e$  is the equilibrium bond length and  $d_{ij}$  is the characteristic “distance of nearest approach” for elements  $i$  and  $j$ . Hence, a stronger H-bond results in shorter intermolecular O-O distance and longer O-H bond length of the H-donor, which in turn results in larger redshifts of the O-H stretching mode.

Due to the complex character of H-bonds, it is essential that we touch upon various definitions of the H-bond in water [82]. Wernet *et al.* [83] used a geometric condition

$$d_{OO} \leq d_{OO}^{\max} - 0.00044\theta^2, \quad (3.1)$$

where  $d_{OO}$  is the intermolecular O-O distance,  $\theta$  is the H-O-O angle in degrees, and  $d_{OO}^{\max}$  was chosen to be 3.3 Å [83]. The geometric criterion in Eq. (3.1) was found to correlate well with the changes observed in the pre-edge and post-edge of x-ray absorption spectra [83]. As mentioned previously, an excitation to the post-edge can be interpreted as populating the antibonding  $\sigma^*$  resonance of the H-bond [71], and the pre-edge excitation has been associated with H-donors in distorted or broken H-bonded configurations [71,83–86]. Hence, this definition is inherently related to the excited state probed by XAS and not the ground state associated with the H-bond.

Kumar *et al.* [82] extended the definition in Eq. (3.1) to the ground-state dynamics observed in simulations using SPC/E water [87] and systematically investigated geometric conditions based on two-dimensional (2D) potentials of mean force for many different angle-distance pairs used to characterize the H-bond. The determined cutoffs were in qualitative agreement with Eq. (3.1), which strengthens the connection between XAS and ground-state configu-



rations. Kumar *et al.* [82] also investigated energetic criteria, in terms of the distribution of molecular pair energies within the SPC/E force field and an electronic structure-based definition of H-bonding, related to the occupancy  $N$  of the antibonding O-H orbitals. The latter is in direct connection with our interpretation of the H-bond, and was found to correlate the best with the distance-angle condition<sup>†</sup>

$$d_{OH} \leq d_{OH}^{\max} - 0.011\phi + 0.000057\phi^2, \quad (3.2)$$

where  $d_{OH}$  is the intermolecular O-H distance,  $\phi$  is the polar angle of the intermolecular O-H vector in degrees<sup>‡</sup> with respect to the normal of the molecular plane of the H-acceptor, and  $d_{OH}^{\max}$  was chosen to be 2.52 Å [82]. This suggests that the H-bond is more sensitive to the orientation of the H-acceptor than the H-donor, which is reasonable since the oxygen lone-pair orbital is more directional than the intramolecular antibonding O-H orbital [82]. However, because we experimentally are sensitive to  $d_{OO}$  in x-ray scattering and the geometric criterium based on  $d_{OH}$  and  $\phi$  has a root-mean-square (RMS) deviation when correlated with  $N$  that is only a factor of two smaller than the criterium based on  $d_{OO}$  and  $\theta$ , we will discuss H-bonds in this thesis in accord with the geometric definition in Eq. (3.1).

### 3.3 Thermodynamics of Water

The thermodynamics of water are intricate, which is evident from the phase diagram shown in Fig. 3.2, including 12 thermodynamically stable crystalline phases (in fact, up to 16 crystalline phases have been reported [88]), numerous triple points, and at least one critical point. In this thesis, the studies are performed at near-atmospheric pressure, and we will thus focus on the lower part of the phase diagram, simplifying it greatly. Here, the liquid phase is bounded at high temperature by the liquid-gas coexistence line, starting at the triple point situated at 612 Pa or 4.59 Torr and 273.16 K for H<sub>2</sub>O [89] (661 Pa and 276.97 K for D<sub>2</sub>O [90]) and ending at the gas-liquid critical point situated at 22.064 MPa and 647 K [90]. At low temperature, it is bounded by the liquid-ice coexistence line, situated at 273.15 K at atmospheric pressure and decreasing in temperature with increasing pressure to 251 K at ~2 kbar [91]. The equilibrium vapor pressure of H<sub>2</sub>O is 23.8 Torr at 298 K [90], but decreases by several orders of magnitude when water is supercooled [92],

<sup>†</sup>The correlation with the occupancy  $N$  of the antibonding O-H orbitals was established for all different distance-angle conditions by assuming  $N$  to be an exponentially decaying function of distance and quadratic function of angle.

<sup>‡</sup>Eq. (3.2) is valid for  $0^\circ \leq \phi \leq 90^\circ$ , otherwise  $\phi$  should be replaced by its complement  $180^\circ - \phi$ .

which is important for the temperature calibration of the water droplets studied in Papers II-III, VI (see Section 5.3).

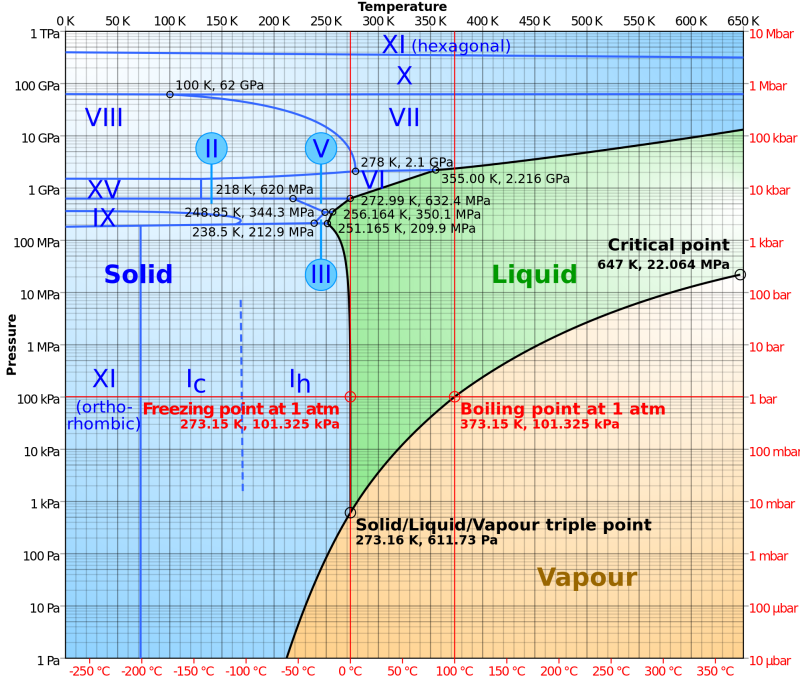


**Figure 3.2:** Phase diagram of water (H<sub>2</sub>O), with the pressure on logarithmic scale in Pa to the left and in bar to the right, and with temperature on linear scale in °C at the bottom and in K at the top. The liquid-gas critical point, the triple points, along with the freezing and boiling point at atmospheric pressure have been marked. The image was taken from Wikipedia [93] according to the Creative Commons Attribution-Share Alike 3.0 Unported license with compiled data from Refs. [94,95].

As mentioned in Chapter 1, many of water's anomalous properties become dramatically enhanced upon supercooling water below its melting point  $T_m$ . In Fig. 3.3, the thermodynamic properties of water are compared as a function of temperature to a simple liquid, such as a Lennard-Jones liquid governed by van der Waals interactions at intermolecular distances [96]. The simple liquid has monotonically decreasing thermodynamic response functions ( $\kappa_T$ ,  $c_p$ , and  $\alpha$  defined below) with decreasing temperature, whereas the density  $\rho$  steadily increases as the liquid is cooled. At high temperatures the qualitative behavior of water is similar to the simple liquid, but when water is cooled below 320 K the discrepancies start to appear. It is first apparent in the isothermal compressibility  $\kappa_T$  and the isobaric molar

heat capacity  $c_P$  with minima at 319 K [1] and 308 K [1, 2], respectively. The thermal expansion coefficient  $\alpha$  decreases anomalously fast and vanishes at 277 K [1] as the density reaches its maximum. The thermodynamic properties are defined as [97]

$$\rho \equiv \frac{m}{V_m}, \quad (3.3)$$

$$\kappa_T \equiv \left( \frac{\partial \ln V_m}{\partial P} \right)_T, \quad (3.4)$$

$$c_P \equiv T \left( \frac{\partial S_m}{\partial T} \right)_P, \quad (3.5)$$

$$\alpha \equiv \left( \frac{\partial \ln V_m}{\partial T} \right)_P, \quad (3.6)$$

where  $m$  is the molar mass,  $V_m$  is the molar volume,  $S_m$  is the molar entropy,  $P$  is the pressure, and  $T$  is the temperature. As water is cooled below 277 K, the volume change is anti-correlated with temperature (as discussed in Chapter 1) and thus  $\alpha$  becomes negative. It can be shown that each one of the thermodynamic response functions is associated with a corresponding fluctuation [1, 98]

$$\langle (\delta V)^2 \rangle = V k_B T \kappa_T, \quad (3.7)$$

$$\langle (\delta S)^2 \rangle = N k_B c_P, \quad (3.8)$$

$$\langle \delta S \delta V \rangle = V k_B T \alpha, \quad (3.9)$$

where  $\delta V$  is the mean-subtracted fluctuating volume,  $V$  is the mean value of the fluctuating volume (for a fixed number of molecules  $N$ ),  $\delta S$  is the mean-subtracted fluctuating entropy,  $S$  is the mean value of the fluctuating entropy (for a fixed number of molecules  $N$  at fixed pressure  $P$ ),  $k_B$  is Boltzmann's constant, and  $\langle x \rangle$  denotes the ensemble average of  $x$ . This means that  $\kappa_T$  is proportional to the variance of the fluctuating volume,  $c_P$  is proportional to the variance of the fluctuating entropy, and  $\alpha$  is proportional to the covariance of the fluctuating volume and entropy. When  $\alpha$  is negative, entropy and volume fluctuations are anti-correlated. Hence, the increase in magnitude of the thermodynamic response functions below  $T_m$  implies that the volume and entropy fluctuations increase strongly upon supercooling. We will discuss the implications further in Section 3.6.

### 3.4 Crystalline Ice

The close similarity between the equilibrium H-O-H angle in water of  $104.52^\circ$  and the tetrahedral angle of  $109.46^\circ$  suggests that water tends to form tetrahedral H-bonds upon crystallization. Indeed, the most stable ice phase at

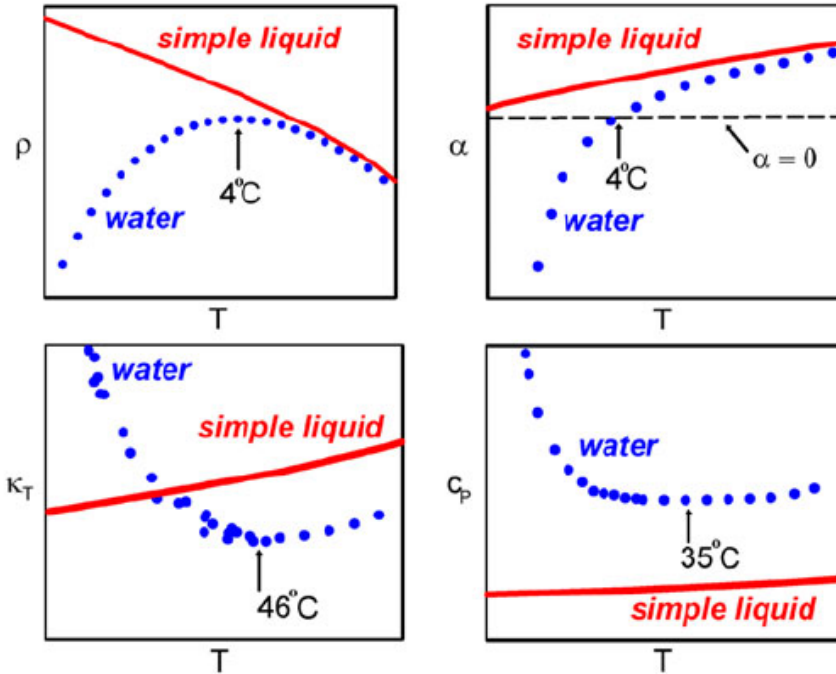


**Figure 3.3:** Schematic comparison of the thermodynamic properties of liquid water to those of a simple liquid, reproduced by permission of IOP Publishing from Ref. [1]. The graphs show the isobaric temperature-dependence of the density  $\rho$  (top left), thermal expansion coefficient  $\alpha$  (top right), isothermal compressibility  $\kappa_T$  (bottom left), and isobaric molar heat capacity  $c_p$  (bottom right). The maxima, minima, and roots of the functions are marked by their corresponding temperature in  $^{\circ}\text{C}$ .

atmospheric pressure below  $T_m$  and above 72 K [99] is hexagonal ice, denoted ice  $I_h$ , with a tetrahedral arrangement of the oxygen atoms. It can be regarded as an  $A \cdot B \cdot A \cdot B$  stacking of layers consisting of a network of open puckered hexagonal rings. The dimensions of the hexagonal unit cell are  $a = 4.498 \text{ \AA}$  and  $c = 7.338 \text{ \AA}$  (which is twice the layer spacing) at 98 K with a corresponding density of  $0.924 \text{ g/cm}^3$  [100]. When water freezes below 190 K, the kinetically favored cubic ice phase, denoted ice  $I_c$ , has been frequently observed [101, 102]. It can be regarded as being built up by layers identical to those of hexagonal ice, but with an  $A \cdot B \cdot C \cdot A \cdot B \cdot C$  stacking typical of the diamond cubic system. The dimensions of the pseudohexagonal unit cell are  $a = 4.495 \text{ \AA}$  and  $c = 11.012 \text{ \AA}$  (which is thrice the layer spacing) at 88 K with a corresponding density of  $0.923 \text{ g/cm}^3$  [100]. More recently, it has also been

proposed that ice that crystallizes homogeneously out of supercooled water is initially neither of these phases, but is instead composed of randomly stacked layers of cubic and hexagonal sequences, denoted stacking-disordered ice [103–107], which quickly transforms into ice  $I_h$  above 237 K [108]. However, as the  $c$  distance is 50 % larger for ice  $I_c$  than for ice  $I_h$ , the layer spacing is equal for the two phases and the local tetrahedral structure of the first hydration shell is thus identical for ice  $I_h$ , ice  $I_c$ , and stacking-disordered ice.

### 3.5 Polyamorphism of Water

In addition to the remarkable number of crystalline phases, there is a rich variety of metastable states reported for glassy water [109–111]. As metastable water is cooled below the glass transition temperature  $T_g$  of  $136 \pm 2$  K [112–114], it forms a glass. Traditionally, glasses are defined as solids that lack long-range order and are often regarded as vitrified liquids, in which the molecules are kinetically immobilized [111]. However, this is only true if the glass is thermodynamically connected to the liquid, which means it must experience a reversible glass-liquid transition [115]. We may separate amorphous solids by their reversibility, and, throughout this thesis, we will denote an amorphous solid a glass if, and only if, it may undergo a reversible glass-liquid transition. Naturally, there are many more amorphous ices than there are phases of glassy water. However, as we shall see below, there appears to exist at least two distinct families of amorphous ices, separated by an apparent first-order transition [116,117], which have been suggested to correspond to two different glassy phases of water [118,119].

Before we describe the various amorphous states, it is important that we touch on metastability. A metastable state implies the existence of a free energy barrier to the thermodynamically stable phase [115]. For a metastable liquid, this free energy barrier prevents the formation of crystal nuclei, whereas for a glass, there are free energy barriers which impede motions from one microscopic configuration in the liquid (denoted a microstate) to another [115]. These two types of metastability behave differently and can be understood in terms of the ergodicity hypothesis, which says that, over long periods of time, the system occupies all accessible microstates in phase space with equal probability. Thus, the time average of an ergodic system will be equal to the ensemble average over all microstates that fulfill energy conservation. In this thesis, we will classify metastable states as metastable liquids if they follow the ergodic hypothesis on some experimentally relevant timescale when the part of phase space that describes the microstates of

the liquid is considered<sup>§</sup>. Hence, the structure and properties of metastable liquids can be measured at a thermodynamic state point independent of its history. This is not the case for amorphous ice, which in this thesis denotes metastable states that are non-ergodic on the given timescale and behave like structurally arrested phases. Thus, glasses are per definition out of equilibrium.

### 3.5.1 Low-density Amorphous Ice

Amorphous solids are traditionally formed by cooling the liquid rapidly below  $T_g$  or by vapor deposition onto a cold plate, kept well below  $T_g$ . If this is done with water at near-atmospheric pressure, it has been customary to call these amorphous solids hyperquenched glassy water [120–122] (HGW) and amorphous solid water [112, 123, 124] (ASW), respectively. Both HGW and ASW have low density [1], which after annealing has been verified to be  $\sim 0.94 \text{ g/cm}^3$  at 1 bar and 77 K, [125]. Alternatively, low-density amorphous (LDA) ice has been formed by temperature- or pressure-induced transformations [117, 126] of an amorphous ice of higher density, discussed in detail in Section 3.5.2, resulting in an equivalent density of  $0.94 \text{ g/cm}^3$  at 1 bar and 77 K, close to that of ice  $I_h$ . Although the behavior of ASW, HGW, and LDA ice differs upon annealing [127], their PCFs are very similar [110] and they will be regarded as belonging to the same glassy phase of water in this thesis [1], possibly as different sub-states [111] or different degrees of relaxation. In Fig. 3.4, the PCF of LDA ice is shown as the black solid curve, and it exhibits local tetrahedral order and a clear separation between the first and second hydration shells located at  $\sim 2.8 \text{ \AA}$  and  $\sim 4.5 \text{ \AA}$ , respectively, with low probability of interstitial molecules [110, 128].

### 3.5.2 High-density Amorphous Ice

In 1984, Mishima et al. [126] found something surprising: when ice  $I_h$  is pressurized above  $\sim 10 \text{ kbar}$  at 77 K, it undergoes a pressure-induced amorphization to high-density amorphous (HDA) ice with a density of  $\sim 1.17 \text{ g/cm}^3$  at zero pressure [116], which is  $\sim 24\%$  higher than that of LDA. In Fig. 3.4, the PCF of HDA ice is shown as the red dashed curve, and it exhibits a collapse of the second hydration shell compared to LDA ice to  $\sim 3.7 \text{ \AA}$ , with an interstitial molecule inside  $r \leq 3.3 \text{ \AA}$  that is not directly H-bonded to the center molecule [128]. If it is heated above  $\sim 117 \text{ K}$ , it transforms irreversibly into LDA ice with a heat evolution of  $42 \pm 8 \text{ J/g}$  [126] at atmospheric pressure, which in turn can be pressurized at 77 K and exhibits a sharp transition

---

<sup>§</sup>The large free energy barrier to form the crystal is thus assumed to clearly separate the microstates of the liquid from that of the crystal.

at  $6 \pm 0.5$  kbar to HDA ice [116]. Although this transition is irreversible at 77 K, it can be made reversible at an elevated temperature of  $\sim 135$  K and occurs at a pressure of  $\sim 2$  kbar (with some hysteresis of  $\pm 1.3$  kbar) with an abrupt volume change of  $0.20 \pm 0.01$  g/cm<sup>3</sup> [117]. This suggests that there may exist a first-order transition between two glassy phases of water, which has been questioned based on the continuous structural transformation from high- to low-density amorphous forms observed upon annealing at atmospheric pressure [129]. Furthermore, the reversible LDA-HDA transition is not conclusive evidence of a first-order phase transition, since one should be able to map out the coexistence line of the two phases and observe the nucleation of one phase growing out of the other. Although this has not yet been possible microscopically [111], macroscopic samples including both LDA ice and HDA ice have been prepared [130, 131], which strengthens the possible coexistence of LDA ice and HDA ice.

The thermal stability of HDA ice at ambient pressure varies strongly with the method of preparation [111]. Therefore, HDA ices have been classified into unannealed (uHDA) and expanded (eHDA) [132], which transform to LDA ice upon heating at  $\sim 117$  K and 131–134 K, respectively [131, 132].

If we assume that both LDA ice and HDA ice correspond to two different glassy phases of water, they should, when heated above their glass transition temperatures, transform into two different liquids to which they are thermodynamically connected (discussed further in Section 3.6.4). Unless the temperature-dependence of the viscosity of the two liquids is identical, the glass transition should occur at different temperatures. Recently, it was reported that in addition to  $T_g$ , which is associated with the glass transition of LDA ice, a second glass transition temperature of eHDA ice was observed at 116 K and 1 bar [133].

### 3.5.3 Very High-density Amorphous Ice

If HDA is annealed at temperatures above 130 K and pressures above 0.8 GPa, an amorphous solid with even higher density than HDA is formed [134]. Its high density of 1.25 g/cm<sup>3</sup> at 1 bar and 77 K [134] has resulted in naming it very high-density amorphous (VHDA) ice. The PCF of VHDA ice is shown in Fig. 3.4 as the green dash-dotted curve, which is indicative of an even stronger collapse of the second hydration shell compared to LDA ice to  $\sim 3.4$  Å, with two interstitial molecules inside  $r \leq 3.3$  Å [135]. Unlike the LDA-HDA transition, the transformation from HDA ice to VHDA ice is continuous and reversible [136]. Although it is unclear whether HDA ice and VHDA ice are two distinct phases thermodynamically connected to two separate liquids, eHDA ice and VHDA ice have very different compressibilities along (and just

below) the crystallization line [111,137] with two linear regimes of density as a function of pressure that result in a clear delimiter between the states.

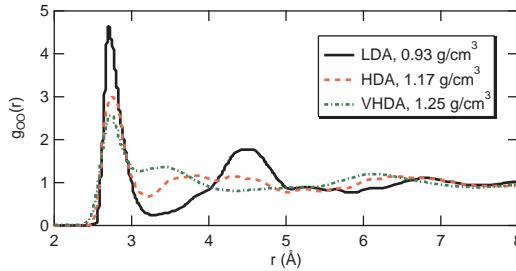


**Figure 3.4:** The oxygen-oxygen PCF  $g_{OO}(r)$  for various amorphous ices, namely LDA ice (black solid line), HDA ice (red dashed line), and VHDA ice (green dash-dotted line), adapted from Finney *et al.* [128,135].

## 3.6 Theoretical Scenarios of Metastable Water

As liquid water is supercooled, the thermodynamic response functions shown in Fig.3.3 grow drastically in magnitude. Extrapolations of the thermal expansion coefficient [6], isothermal compressibility [7], and isobaric molar heat capacity [2] can all be fitted with a power law that appears to diverge at a temperature  $T_S$  of 228 K. It should be noted that in most liquids, volume and entropy fluctuations become smaller as the temperature decreases and volume and entropy fluctuations are correlated [1]. Water's behavior below 277 K contradicts this completely, and numerous scenarios have been proposed to explain this rapid increase in entropy and volume fluctuations in the deeply supercooled regime of liquid water's phase diagram. Below is a short description of four families of models that are thermodynamically consistent [1]. In addition, there have been several concerns raised regarding the metastability of water and whether it is possible to equilibrate the liquid below  $T_h$ , which will end this section.

### 3.6.1 Stability-limit Conjecture

The stability-limit conjecture proposes that the increase in entropy and volume fluctuations upon supercooling water is due to that the liquid-gas spinodal<sup>¶</sup>, which extends from the liquid-gas critical point, retraces from nega-

<sup>¶</sup>The spinodal line of a superheated liquid is where  $\left(\frac{\partial P}{\partial V_m}\right)_T = 0$  [138], so that  $\kappa_T^{-1} = 0$  and the liquid is no longer mechanically stable.



tive pressures in the deeply supercooled regime [139, 140] (see Fig. 3.5). The liquid-gas spinodal is the mechanical stability limit of the liquid with respect to the gas phase. The increase in entropy and volume fluctuations would then mean that the mechanical breakdown of the liquid is approached as the metastable liquid is supercooled further [140]. The temperature  $T_S$  where the thermodynamic response functions are predicted to diverge would thus be the temperature of the retracing spinodal at atmospheric pressure [1].

Thermodynamic consistency demands that the slope of a spinodal curve must change sign upon encountering a line along which the thermal expansion coefficient vanishes [1], *i.e.* a line along which the density reaches its maximum  $\rho_{max}$ . The underlying reason for the anomalous increase in entropy and volume fluctuations would therefore be the density maximum present in water, which is caused by the competition between structural collapse in the H-bonded network and thermal expansion as discussed in Chapter 1.

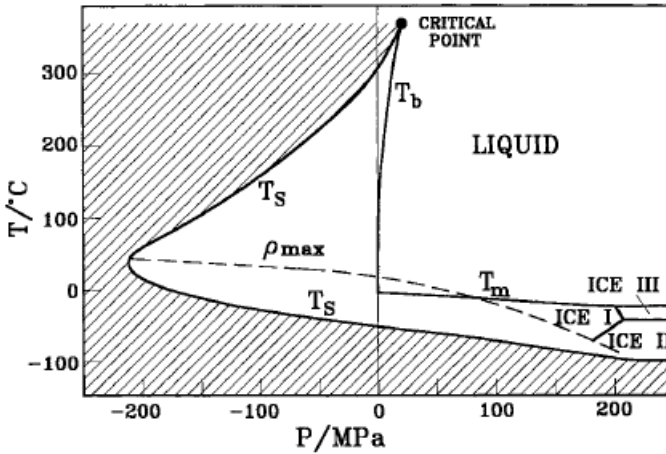


**Figure 3.5:** The phase diagram of water, including the postulated retracing spinodal.  $T_m$  denotes the melting temperature line,  $T_b$  indicates the boiling temperature line,  $\rho_{max}$  represents the temperature line of maximum density, and  $T_S$  symbolizes the continuous (two-valued) temperature curve of the retracing spinodal. The figure was reproduced by permission of IOP Publishing from Ref. [1] and was originally adapted from Ref. [139].

### 3.6.2 Critical Point-free Model

In the critical point-free model, an order-disorder transition separates two liquid phases in the deeply supercooled regime [141]. The two phases are possibly separated by a first-order transition (with corresponding spinodal),

which would explain the anomalous increase in the thermodynamic response functions similarly to the stability-limit conjecture, but due to a different spinodal and hence stability limit. The order-disorder transition extends all the way down to negative pressures, where it crosses the stability limit of the superheated liquid. Thus, a critical point between the two liquid phases does not have to be evoked in the water phase diagram.

### 3.6.3 Singularity-free Scenario

In contrast to the stability-limit conjecture and the critical point-free model, in the singularity-free scenario the thermodynamic response functions remain finite at all temperatures for deeply supercooled water. The increase in entropy and volume fluctuations upon supercooling the liquid is explained by the negative slope of the temperature line of maximum density, where the thermal expansion coefficient vanishes. This implies that, starting at any point where  $\alpha = 0$ ,  $\kappa_T$  increases upon isobaric cooling,  $\alpha$  increases upon isothermal compression and decreases upon isothermal decompression, and  $c_P$  decreases upon isothermal compression [1]. As a consequence, the magnitude of the thermodynamic response functions would increase upon supercooling, but they would all remain finite and reach coinciding maxima [142]. Hence, the proposed divergence at  $T_S$  would be an artifact of extrapolation.

### 3.6.4 Second Critical Point

The last explanation for the increase in entropy and volume fluctuations is that there would exist a liquid-liquid critical point (LLCP) [118,119] in deeply supercooled water (see Fig. 3.6) characterized by a critical temperature  $T_c$ , critical pressure  $P_c$ , and critical density  $\rho_c$ . The existence of two different liquid phases in a unimolecular liquid seems perplexing, but would be the effect of incommensurate requirements of minimizing energy and entropy simultaneously. This would cause a low-density liquid (LDL) to exist at low temperatures and pressures with strong tetrahedral H-bonds that minimize energy, and a high-density liquid (HDL) to exist at low temperatures and high pressures with collapsed second shell and strong disorder that maximizes entropy [143]. Thus, the structures of the two liquids would resemble the thermally excited structures of LDA and HDA ice [144], which would be assumed to be the glassy equivalents of LDL and HDL. The two liquid phases would be separated by a first-order phase transition line, ending in a critical point in “no-man’s land”. Hence, stable water would be a supercritical mixture of the two phases with local structures resembling both LDL and HDL. Due to the fact that stable water is lying on the high-density side in the phase diagram, a majority of HDL structures would be predicted to exist

at ambient conditions [143]. When supercooling the liquid at atmospheric pressure (below the proposed critical pressure), a maximum in entropy and volume fluctuations will be observed when a 50:50 ratio of LDL and HDL structures is present in the liquid. This locus of maximum fluctuations is known as the Widom line and extends from the critical point into the supercritical regime [97], which would form a clear connection between the structure of the liquid and the thermodynamic properties.

It should be noted that the position of the LLCP in the phase diagram makes a large difference on the physical observables. Hence, several of the other models can be viewed in terms of extreme cases of the LLCP model. For example, the critical point-free model can (ironically) be interpreted as  $P_c$  shifted to negative pressures below the stability limit of superheated water, so that only a first-order transition is observed between HDL and LDL in the physically relevant part of the phase diagram [145]. On the other hand, the singularity-free model can be viewed as having the LLCP shifted to  $T_c = 0$  K [145], resulting in only a continuous change (*i.e.* supercritical behavior) of the thermodynamic response functions above absolute zero. In the rest of this thesis, we will therefore assume that the LLCP model represents an LLCP at non-zero  $T_c$  and positive  $P_c$ , most likely between 500-2000 bar.

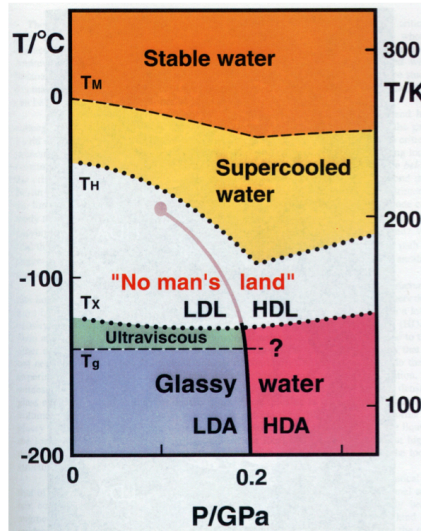


**Figure 3.6:** The phase diagram of water showing the proposed second critical point, reprinted from Ref. [146] with permission from IOS Press. The LLCP is caused by the existence of two different liquid phases, denoted LDL and HDL, which are separated by a first-order phase transition ending in a critical point. The LLCP is residing in “no-man’s land”, preventing it from being directly probed by experiments.

### 3.6.5 Equilibration and Metastability Below $T_h$

Although the models described above summarize the theoretical scenarios that are thermodynamically consistent [1], there have been several concerns raised regarding the metastability of water below  $T_h$  and the validity of applying equilibrium thermodynamics [147–150]. Swenson & Teixeira [147] suggested that the increase in magnitude of the thermodynamic response functions at 228 K is in fact related to the crossover between  $\alpha$ -relaxation and  $\beta$ -relaxation. Thus,  $T_g$  should be revised to  $\sim 228$  K and it is the local  $\beta$ -relaxation that is responsible for the calorimetric transition at  $\sim 136$  K.

Moore & Molinero [148] found that a structural transformation toward an LDL, consistent with an LLCP scenario and crossing the Widom line, occurred in water simulations using the mW model at  $\sim 200$  K. However, the structural transformation also controlled the homogeneous ice nucleation rate, which resulted in that crystallization took place faster than LDL's equilibration time so that the liquid could not equilibrate below 200 K when crystallization was diffusion limited. These results will be discussed further in Section 6.2.1 where the results of Paper III are put in context.

Limmer & Chandler [149, 150] mapped out the free energy landscape as functions of  $\rho$  and the crystal-order variable  $Q_6$  for the ST2, TIP4P/2005, mW, and SW models, and found evidence for only one stable or metastable liquid phase and one ice-like crystal phase. Nevertheless, when non-equilibrium free energy surfaces were calculated at short sampling times for the ST2 model, two liquid basins were present, which was suggested to be the reason for previous reports [118, 151, 152] supporting an LLCP in ST2 water. Thus, the coarsening of the ordered ice-like phase would be responsible for the increase in thermodynamic response functions and the putative LLCP-behavior would be caused by non-equilibrium effects. In fact, the observed behavior could be interpreted as a mechanical stability limit toward the crystal phase associated with a liquid-crystal spinodal.

These non-equilibrium theories are currently under debate. Swenson & Teixeira [147] rely on experimental data of relaxation times for nanoconfined water, in which the interaction with the confining surfaces makes the relevance to bulk water unclear [17, 153]. The mW model [154] has been criticized for treating H-donors and H-acceptors identically, although the difference between the two is an important aspect of the cooperativity in water [70], and Limmer & Chandler's results have been questioned by a recent investigation that confirms that the two liquid phases in ST2 water can be equilibrated and coexist [155]. Lack of experiments in “no-man's land” makes it difficult to prove or disprove these arguments for bulk water, but they highlight the difficulty of verifying equilibration and the complexity of metastability upon deep supercooling.

### 3.7 The Structure Puzzle of Water

There are numerous studies of the structure of water, dating back to late 19<sup>th</sup> century [156,157] and performed using a vast variety of experimental techniques. The proposed models can be divided into two categories: mixture models [118,157] according to which liquid water consists of “ice-lik” molecules with tetrahedral structure and other more close-packed molecules with less well-defined H-bonds; and continuum models [158,159] according to which liquid water is composed of a single component, usually assumed to be four-coordinated, with a continuous distribution of bond energies and geometries. Traditionally, continuum models have been favored by diffraction arguments (of non-existing concentration fluctuations in water above the isothermal compressibility) [159–161] and molecular dynamics (MD) simulations [162], but they struggle to explain the anomalous behavior of the thermodynamic response functions in the deeply supercooled regime [1,145].

To put the current research in context, I list below a very brief summary of the direct structural results I have encountered in the literature using x-rays (including other techniques that yield comparable results). The summary does not claim to be complete or unbiased, but it attempts to discuss the possibility of mixture models versus continuum models without any interpretation regarding the structure of water beyond direct experimental evidence. For detailed explanations of techniques or results, the reader is referred to the original articles cited in the text and the references therein. For expansions of acronyms, see the List of Abbreviations.

**XAS/XRS** Pre-edge associated with distorted or broken H-bonds [71,83–86], main-edge intensity correlated with density and collapse of 2<sup>nd</sup> shell in  $g(r)$  [163], post-edge associated with H-bond  $\sigma^*$  resonance [71].

**XES** Two peaks in the lone-pair region of  $b_1$  character [164], ratio changes with isotope, temperature, and excitation energy, and reduces to one peak at pre-edge excitation [60]. The  $1b_1$  doublet has been proposed to be caused by a bimodal ground-state H-bond structure [60,143] or excited-state dynamics [165,166].

**RIXS** Internal O-H stretch vibration in the ground state of water is highly blueshifted and close to that of gas phase water when probing molecules excited at the pre-edge [167]. Isotope substitution yields  $50 \pm 20\%$  higher preference for O-H to participate in the weakened or broken H-bond than O-D [167].

**AES** The excited electron remains localized longer than 20 fs upon pre-edge excitation, whereas the electron delocalizes in less than 500 as when excited at the post-edge [54].

**PES** One  $1b_1$  band that is narrow enough to exclude splitting in the valence band structure [168].

**XPS** One broad O 1s peak due to strong phonon excitations [169], which make the peak too broad to resolve the  $1b_1$  peaks in XES. Thus, if a two-structure motif is assumed to explain the x-ray emission spectra, it implies a core-level shift of 0.7-0.9 eV, depending on temperature [60].

**WAXS/ND** RDF<sup>||</sup> displays first coordination shell at  $\sim 2.8$  Å of  $\sim 4$  molecules for water and amorphous ices (excluding interstitials) [5, 36, 128, 135]. LDA ice suggests tetrahedral structure with second coordination shell at  $\sim 4.6$  Å of  $\sim 13$  molecules [128]. For HDA ice and VHDA ice the second shell collapses to  $\sim 3.9$  Å and  $\sim 3.6$  Å containing  $\sim 6$  and  $\sim 8$  molecules, respectively [128, 135]. Water's second shell at 4.6-4.7 Å contains  $\sim 15$  molecules [3]. The coordination numbers of the second shells are highly dependent on cutoff radius, which differs if the minima are determined from the RDF or the PCF. Experimental data of water at 298 K do not discriminate between a liquid dominated by tetrahedrally coordinated water molecules or molecules classified as single H-donors according to the geometric criterium defined in Eq. (3.1) [170].

**SAXS** Below 298 K, anomalous density fluctuations increase when lowering the temperature with a fitted Ornstein-Zernicke [171] correlation length of 3-8 Å [143, 172, 173] at 253 K. System still close to being hyperuniform [174] with  $S(0) \approx 0.07$  [143].

When forming a model to describe the structure of water, all these results (and many more) have to be taken into account. This may seem like an overwhelming task, but it is important to avoid over-interpretation of a single structural-sensitive technique, and this also highlights the complexity of solving the structure puzzle of liquid water.

---

<sup>||</sup>Due to the  $r^2$  dependence, the RDFs yield coordinations peaks that are shifted to slightly higher distances compared to the peaks deduced from the PCFs shown in Fig. 3.4.

# Chapter 4

## Methods

In this chapter, experimental details related to Papers I-VI will be described. The chapter will put the chosen methods in context and focus in detail on some aspects where my contribution was significant. Especially, I will elaborate on the characterization of the droplet dispensers used at LCLS. The interested reader is referred to the papers for further information.

### 4.1 Synchrotron Measurements

The experiments presented in this thesis utilize synchrotron radiation, which is the emission of electromagnetic radiation from the acceleration of an electron at relativistic speeds (*i.e.* close to the speed of light  $c$ ) [175, 176]. The effect was first observed from the General Electric synchrotron in 1947 [177]. The loss of energy was initially considered a nuisance when accelerating electrons, but the unique capabilities to produce intense x-rays with high brilliance (see Fig. 4.1 for definition) using synchrotron radiation has led to dedicated storage rings (known as 2<sup>nd</sup> and 3<sup>rd</sup> generation light sources), to which SSRL and ALS belong. I will not dwell on the physics of synchrotron radiation in this thesis, but I only give a brief introduction to the recent free-electron laser (FEL) development in the x-ray regime in Section 4.2, sometimes considered to be the 4<sup>th</sup> generation light source [178]. The interested reader is referred to one of the following books [20, 179–181] or Chapter 2 in the X-ray Data Booklet [25] for a condensed summary.

#### 4.1.1 X-ray Scattering

The WAXS measurements reported in Paper I were performed at BL 7-2 at SSRL. As discussed in Section 2.3.3, the aim of conventional x-ray scattering is

to extract the PCF, which is a fundamental measure of structure in disordered matter and frequently used in simulations to benchmark the structure. In order to do so accurately, one needs to measure  $S(q)$  to sufficiently high  $q$  that all structural correlations have decayed. This is challenging, because of several reasons. First, the  $q$ -range of a detector at a given energy is limited. We recall that the momentum transfer  $q$  can be calculated according to Eq. (5.4) from the wavelength  $\lambda$  of the radiation and the scattering angle  $\theta$ , which means that a wide  $q$ -range can be obtained in an angular-dispersive setup (varying  $\theta$ ) or energy-dispersive setup (varying  $\lambda$ ). In Paper I, we chose to utilize an angular-dispersive setup with  $\theta$  varying between  $3\text{--}135^\circ$  at  $17\text{ keV}$ , corresponding to an incident wavelength  $\lambda = 0.73\text{ \AA}$ . This enabled us to reach a maximum momentum transfer of  $\sim 16\text{ \AA}^{-1}$ .

Second, the elastic scattering signal of water decays by several orders of magnitude at high  $q$  (see Fig. 5.1), which sets harsh requirements to achieve high signal-to-noise. Although many experiments have been made previously [3, 4, 37, 38, 159, 182, 183], most of them relied on theoretical corrections for Compton scattering, which becomes increasingly important at high  $q$  (see Section 2.2.3), and subtractions of background scattering from the sample container. Inspired by Fu *et al.* [3], we wanted to remove these sources of error experimentally and increase the statistics and energy resolution compared to previous work. The scattering from the sample container could be circumvented by using a water jet with a diameter of  $360\text{ mm}$ , which was aligned at the rotation center of a Huber 6-circle diffractometer and kept in a He environment to reduce the air scattering signal. The angular-dispersive setup enabled us to eliminate Compton scattering experimentally by using a germanium crystal analyzer with  $15\text{ eV}$  energy resolution and thus filtering out scattering intensity outside of the elastic peak. The crystal was mounted in a Rowland geometry to refocus the scattered beam on a photomultiplier tube (PMT) detector, which was shielded by a beam stop, as illustrated in Fig. 1 in Paper I. The sample temperature was controlled through the water flow system and diffraction data were recorded for  $\text{H}_2\text{O}$  at  $280$ ,  $298$ , and  $339\text{ K}$ . To increase the statistics at large  $q$ , a constant scattering dose of about  $85000$  photon counts was recorded at each data point, resulting in a statistical uncertainty below  $1\%$  (assuming a Poisson distribution).

In Paper II, the synchrotron measurements had a different objective, namely to complement the FEL measurements (described in Section 4.2) by recording scattering data over a large temperature range. Thus, a similar setup to previous small-angle x-ray scattering (SAXS) experiments [143, 173] at BL 4-2 at SSRL was utilized, which had been proven effective to supercool water while controlling the temperature with a measurement accuracy of  $\pm 1\text{ K}$ . Data were recorded from  $323\text{ K}$  down to  $251\text{ K}$  using a static liquid water sample with a total volume of  $\sim 5\text{ }\mu\text{l}$  that was contained in a quartz



capillary with an inner diameter of 1.5 mm. The quartz capillary was integrated into a sample cooling holder kept in an  $N_2$  gas atmosphere to eliminate water condensation. To be able to directly compare the results to the FEL measurements, we wanted to cover a  $q$ -range of  $0.5 \leq q \leq 3.5 \text{ \AA}^{-1}$ , which was achieved by using a static optical fiber-coupled Rayonix MX225-HE detector with an active area of  $225 \times 225 \text{ mm}^2$  at a sample-detector distance of 329 mm and photon energy of 14.5 keV. The synchrotron measurements were crucial to calibrate the temperature in “no-man’s land” and the procedure is described thoroughly in Section 5.3.7.

### 4.1.2 X-ray Absorption Spectroscopy

During the last decade, XAS\* has been established as a standard technique at synchrotrons to study H-bonding in water [71,83,184,185], ice [71,83,163,186,187], aqueous solutions [71,188–194], and water at interfaces [71,86,195,196]. Its sensitivity to hybridization of the spatially extended unoccupied valence states around the oxygen atom in water makes it possible to characterize H-bonding topology. Even so, there is an open debate, specifically for ice, regarding the pre-edge in the O K-edge spectrum of water. Since the pre-edge has been established to be associated with broken or distorted H-bonds [71,83,85,86,167] (see Sections 3.2 and 3.7), one would expect that it would be absent for ice  $I_h$ . This is also supported by a symmetry argument for the tetrahedral symmetry group  $T_d$ , for which the lowest unoccupied molecular orbital would have pure O2s character and therefore not contribute to the O K-edge spectrum according to the dipole selection rule. However, most experimental x-ray absorption spectra of crystalline ice show a distinct pre-edge [71,163,187], and it has even been argued that it is inherent to the ice spectrum [163,185].

Due to this discrepancy, we studied ice in Paper IV under two different growth conditions using XAS. The first sample was prepared by injecting  $H_2O$  into a Si sample cell with 300 nm thick Au spacers and 200 nm thick  $Si_3N_4$  windows (described in detail in Refs. [193,197]). Such a sample had been measured previously [71,198] at the scanning transmission x-ray microscopy (STXM) end station [199] at BL 11.0.2 at ALS, and it had been demonstrated to yield high-quality x-ray absorption spectra of water with very little saturation effects and low probability of non-dipole transitions [71]. However, the standard setup used with the sample cell at the STXM end station could only record spectra at room temperature. I therefore developed a custom-made Cu sample holder that cooled the sample cell using a 1.5 W Peltier element, which in turn was cooled through Cu foil by a liquid  $N_2$

---

\*Here, we also include x-ray Raman scattering (XRS), the hard x-ray analog of XAS, which follows the dipole selection rule at the limit of low momentum transfers.

reservoir. The sample was cooled by adjusting the Peltier output power and lowering the He pressure in the chamber, so that ice spectra could be recorded at 232 K, corresponding to a He pressure of  $2 \times 10^{-5}$  Torr. The cooling rate at which the ice was formed was approximately 1 K/min.

The second sample was prepared differently, building on previous ultra-high vacuum (UHV) experiments on thin films of ice on a hydrophobic BaF<sub>2</sub> surface [200] at the Surface Science Endstation (SSE) at the elliptical undulator BL 13-2 at SSRL. To minimize the concentration of nucleation sites and favor growth of larger crystallites, the BaF<sub>2</sub> crystal was freshly cleaved along the (111) plane prior to sample loading, after which 30 monolayers (ML) of D<sub>2</sub>O were dosed onto the clean surface while kept at 144 K for 18 min. As touched upon in Section 2.4, there are several different ways of obtaining the absorption cross-section [24]. In our setup, fluorescence yield was not sensitive enough to achieve sufficient signal-to-noise ratio from the ice crystallites, so we were forced to rely on electron yield, which is highly surface sensitive. At the same time, the insulating surface charges easily so that the Auger peaks are broadened and difficult to locate. Thus, we chose to monitor the secondary electrons with kinetic energy of 12 eV and pass energy of 200 eV using a VG-Scienta R3000 hemispherical electron spectrometer, which yields highly bulk-sensitive spectra when the polarization of the incident photons is set to be parallel to the (111) surface. Due to the mean-free path of the low-energy electrons, the effective probing depth of secondary electron yield (SEY) is approximately 50 Å [24], which is less than the estimated thickness of the ice film of  $\sim 110$  Å (from the layer thickness in ice I<sub>h</sub> and ice I<sub>c</sub>). To further minimize the signal from the underlying substrate, the spectrum of the clean surface was subtracted.

## 4.2 Free-electron Laser Measurements

The past decade, FELs have started to emerge in the x-ray regime. These instruments have revolutionized x-ray science, because their unprecedented peak brilliance is  $\sim 8$  orders of magnitude higher than the brightest synchrotrons (see Fig. 4.1), and because they can produce ultrashort ( $\leq 100$  fs) pulses with high degree of coherence<sup>†</sup>, enabling the possibility of single-particle imaging [204] and movies of molecular motion to be recorded [40].

In this thesis, measurements have been performed at LCLS<sup>‡</sup>, which is the

<sup>†</sup>The high degree of coherence is mainly in the transverse direction during standard operation, but seeded beams will increase the longitudinal coherence drastically and reduce the number of modes from a few hundred [201] toward the lower limit of single-mode amplification [202, 203].

<sup>‡</sup>For an animated introduction to LCLS and how a FEL operates, please visit: <http://lcls.slac.stanford.edu/AnimationViewLCLS.aspx>

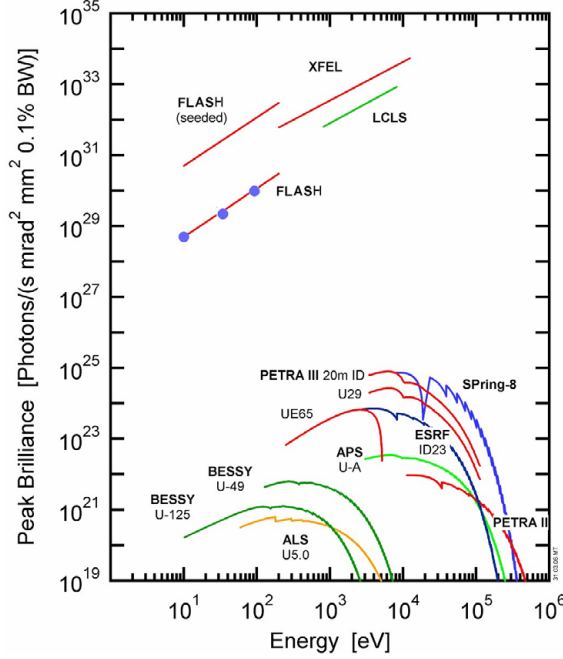


**Figure 4.1:** Peak brilliance of storage ring and FEL sources measured in flux [photons/pulse]  $\div$  pulse length [s/pulse]  $\div$  divergence [ $\text{mrad}^2$ ]  $\div$  cross-sectional area [ $\text{mm}^2$ ]  $\div$  0.1 % bandwidth (BW) [ $0.001\Delta\omega/\omega_0$ ], where  $\Delta\omega$  is the frequency range of the radiation measured and  $\omega_0$  is the nominal frequency of the radiation. The figure was reprinted with permission from Ref. [201].

world's first hard x-ray FEL, situated at SLAC National Accelerator Laboratory. In Paper II, we utilized the FEL to study the structure of the metastable liquid state in “no-man’s land” (*i.e.* below the commonly referenced  $T_h \sim 232\text{ K}$ ) prior to crystallization. In Paper III, the nucleation process was investigated from scattering patterns of individual droplets probed by single shots of the FEL. In Paper V, the effect of the ultrabright pulses on the x-ray emission yield was examined, which was further used in Paper VI to study the valence electronic structure of the metastable liquid state in “no-man’s land” using XES. The choice of techniques to study the metastable liquid should be commented. X-ray scattering is an obvious choice for the first study, since it is a direct probe of the structure and it has high enough cross-section to record a scattering pattern in a single shot. We chose to follow up the scattering study with XES, because x-ray emission of the lone-pair orbital in water has been shown previously to be highly temperature dependent [60]. This will be discussed further in Section 6.3.2. In all experiments, the

ultrabright and ultrashort attributes of the x-ray pulses were utilized. The high transverse coherence only had minor effects on the results presented in Chapter 6, but may be critical in future scattering experiments where the coherent speckles in individual scattering patterns of water are analyzed or the size and shape of ice crystals are reconstructed from the fringes extending around individual Bragg peaks.

Ignoring briefly the scientific impact, which will be discussed more in Chapter 6, the novelty of the experiments can be appreciated solely from their technical aspects, since it was the first time such experiments were performed on water using a FEL. Hence, I will thoroughly go through sample injection in Section 4.2.3, data analysis of single-shot scattering patterns in Sections 5.1.2 and 5.1.3, and temperature calibration in Section 5.3, where my contribution was vital in the multi-national collaborations necessary to perform FEL experiments.

### 4.2.1 Self-amplified Spontaneous Emission

Following Altarelli [178] and aided by Attwood [179], I will give an intuitive introduction to how a FEL operates.

The x-ray FEL is based on a long periodic array of magnetic dipoles and quadrupoles, known as an undulator (see Fig. 4.2). The undulator is characterized by its number of periods  $N$  and their respective wavelength  $\lambda_u$ , together with the magnetic field strength  $B$ . If we consider a relativistic electron with a kinetic energy of  $\gamma m_e c^2$ , where  $\gamma$  is the relativistic factor,  $m_e$  is the electron mass, and  $c$  is the speed of light in vacuum, the characteristic wavelengths of the emitted radiation passing through the undulator is [178, 179]

$$n\lambda = \frac{\lambda_u}{2\gamma^2} \left( 1 + \frac{K^2}{2} + \gamma^2 \theta^2 \right) \quad (4.1)$$

where  $n$  is the harmonic of the undulator ( $n = 1$  is the fundamental),  $\theta$  is the angle from the forward direction, and  $K$  is the deflection parameter defined as

$$K = \frac{eB\lambda_u}{2\pi m_e c}, \quad (4.2)$$

with  $e$  being the electric charge. We shall note three important points. If we want to change the photon energy at an undulator beam line, it is convenient to do so by changing  $B$  in Eq. (4.2) – a characteristic of the undulator – instead of changing  $\gamma$  in Eq. (4.1) – a characteristic of the relativistic electron beam<sup>§</sup> – and this is done practically by tuning the undulator gap (*i.e.* the distance between the upper and lower arrays of magnets). Second, the

<sup>§</sup>At a synchrotron facility, many BLs share the same electron beam, which is stored in a storage ring.

occurrence of higher harmonics above the fundamental is due to deviations from a radiating dipole in the electron rest frame, with odd harmonics corresponding to motions in the direction of the dipole and even harmonics corresponding to motions in the direction of the forward beam. The even harmonics are therefore highly suppressed in the forward direction, because their emission (that has a  $\sin^2 \theta'$  distribution with respect to the direction of motion [20]) forms a hollow cone upon Lorentz transformation to the laboratory frame.

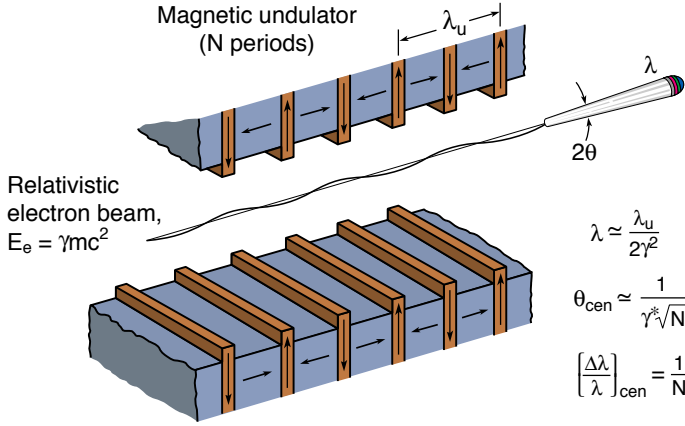


**Figure 4.2:** Schematic operation of an undulator. A relativistic electron beam with a relativistic factor  $\gamma \gg 1$  (i.e. a kinetic energy much larger than its rest energy  $m_e c^2$ ) is sent through a periodic array of magnetic dipoles and quadrupoles, known as an undulator. The undulator is characterized by its number of periods  $N$  and its wavelength  $\lambda_u$ , which together with  $\gamma$  (or  $\gamma^*$ , which is the effective relativistic factor in the forward direction) determines the emitted radiation's fundamental wavelength  $\lambda$ , angular divergence  $\theta_{cen}$ , and spectral BW  $[\Delta\lambda/\lambda]_{cen}$ . The figure was reprinted with permission from Ref. [179].

Last, we note that  $\lambda$  in Eq.(4.1) can be viewed as the distance that the electron beam lags behind the emitted radiation upon traveling one period in the undulator, corresponding to a distance  $\lambda_u$  [178]. Thus, there is a definite phase relationship between an electron and the radiation it emits at different points of the trajectory, and there is constructive interference of the overlapping fields only for wavelengths described by Eq. (4.1) [178]. However, because the electron bunch at a synchrotron with a length of  $\sim 1$  cm is much longer than  $\lambda$ , which is on the order of  $\sim 1 \text{ \AA}$  for hard x-rays, the interference between different electrons is usually averaged out. Because of this, the radiated power is proportional to the number of electrons  $N_e$  in the bunch, which usually contains on the order of  $10^9$  electrons. If, on the other hand, we

could order the electron bunch on a length scale comparable to  $\lambda$ , we could obtain a radiated power proportional to  $N_e^2$  from constructive interference, which would give a huge boost in radiated intensity. In a FEL, the undulator is so long<sup>¶</sup> that the emitted radiation starts to interact with the electrons and order them for us [178]. This microbunching phenomenon [206] occurs because the electric field has a small component in the direction of the forward beam, which accelerates and decelerates the electrons so they radiate in phase with each other [178]. Hence, shot-noise fluctuations in the generated electron bunch will increase the radiation, assuming a Fourier component in the electron density of appropriate wavelength is included, and the coherent emission will in turn reinforce the density fluctuation, which leads to an exponential amplification of the radiated intensity known as self-amplified spontaneous emission (SASE) [178]. The SASE process is the base for the laser-like properties of the FEL and proceeds until saturation occurs due to Coulomb repulsion of the relativistic electrons, which eventually degrades the microbunching. Normally, the FEL is operated in the saturation regime, since it yields higher intensity stability [207]. Since the performance of the FEL depends exponentially on the quality of the electron beam<sup>||</sup>, the SASE process is currently only realized at linear accelerators.

## 4.2.2 Laser Operation Parameters

LCLS has a wide range of parameters that can be tuned to optimize the beam characteristics for the specific experiment performed [205].

During the x-ray emission measurements performed at the SXR instrument [208] using the Liquid Jet Endstation (LJE) [209], the FEL was operated at an average photon energy of 550 eV (corresponding to a wavelength  $\lambda = 2.25$  nm) with a nominal pulse duration of  $\sim 100$  fs. These pulses were delivered at 120 Hz at a bunch charge of 150 pC, resulting in 0.5-1.1 mJ pulse energy at the gas detectors, corresponding to between  $6 \times 10^{12}$  and  $12 \times 10^{12}$  photons/pulse in the white beam (*i.e.* non-monochromatized beam prior to all beam line components); about 10 % of the intensity is estimated to reach the sample.

During the scattering experiments at the CXI instrument [210], the FEL was operated at 9.4 keV photon energy (corresponding to  $\lambda = 1.32$  Å),  $\sim 50$  fs pulse length, 120 Hz repetition rate, 150 pC bunch charge, and  $\sim 3$  mJ pulse energy, resulting in  $\sim 2 \times 10^{12}$  photons/pulse in the white beam; about 25 % of the intensity is estimated to reach the sample.

<sup>¶</sup>LCLS has 112 m of active undulator, but only 60 m is sufficient to achieve saturation [205].

<sup>||</sup>For LCLS, the beam current is  $I \sim 3$  kA [205] (corresponding to  $\sim 10^9$  electrons within a  $\sim 30$   $\mu$ m sphere) compared to synchrotrons where  $I$  usually is around 100-300 mA.

### 4.2.3 Droplet Dispensers

The destructive nature of the FEL necessitates a continuously replenished supply of well-characterized water droplets at 120 Hz, which was achieved by two types of droplet dispensers. Together they covered a temperature range of 222–258 K (see Section 5.3.7).

The size and speed of droplets, which are necessary to determine the droplet temperature from evaporative cooling (see Section 5.3), were determined by mass conservation for a liquid jet and a single-file droplet train with a characteristic frequency and droplet diameter. Assuming the density is constant along the liquid jet and during droplet formation, the droplet dispensers must obey

$$Q = A_{jet}v = \pi \left( \frac{D_{jet}}{2} \right)^2 v, \quad (4.3)$$

$$Q = V_{drop}f = \frac{4\pi}{3} \left( \frac{D_{drop}}{2} \right)^3 f, \quad (4.4)$$

$$v = l_{drop-drop}f, \quad (4.5)$$

where  $Q$  is the volume flow rate,  $A_{jet}$  is the cross-sectional area of the liquid jet,  $v$  is the speed (of droplets as well as jet),  $D_{jet}$  is the jet diameter,  $V_{drop}$  is the droplet volume,  $f$  is the frequency of droplets,  $D_{drop}$  is the droplet diameter, and  $l_{drop-drop}$  is the droplet spacing.

The drop-on-demand dispenser (model MJ-AT-01-020) commercially available from MicroFab Technologies, Inc. is a capillary with an inner diameter of  $20\text{ }\mu\text{m}$ , through which water flows to produce a liquid jet, denoted Rayleigh jet (RJ). The jet can be broken up into droplets in a controlled fashion by a piezoelectric actuator attached to the outside of the capillary. The piezoelectric actuator induces vibrations into the jet at a frequency close to the Rayleigh resonance frequency  $f_R = v/4.55D_{jet}$ , producing at the resonance frequency droplets of diameter  $D_R = 1.89D_{jet}$  [211]. By applying a sine wave form with 8 V amplitude at frequencies of 69 and 106 kHz in Paper II, we managed to produce spatially evenly distributed and uniformly sized droplets of  $37 \pm 9$  and  $40 \pm 6\text{ }\mu\text{m}$  in diameter with droplet spacings of  $198 \pm 7$  and  $109 \pm 5\text{ }\mu\text{m}$ , respectively. The droplet formation was observed through an optical microscope using stroboscopic illumination synchronized with the piezoelectric actuator (see Fig. 4.3). The experimental droplet parameters are listed in Table 4.1. Enforcing experimental overlap in the principal maximum of the elastic scattering structure factor between the RJ data series at LCLS and synchrotron data recorded at SSRL narrowed the uncertainty in droplet

diameters and resulted in the reported 34 and 37  $\mu\text{m}$  droplet diameters in Paper II (see Section 5.3.7 for details).

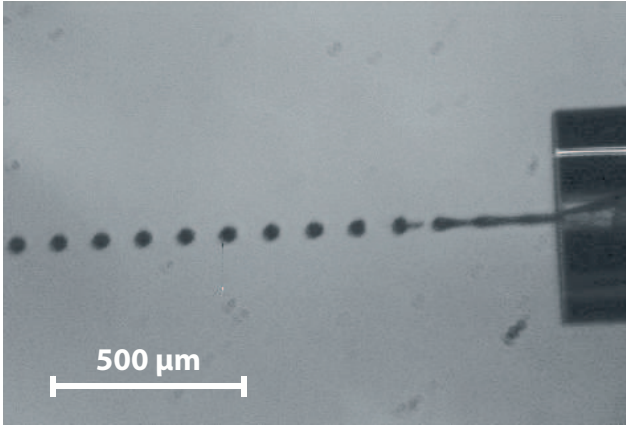


**Figure 4.3:** The droplet dispenser *in situ* during the CXI experiment in Feb 2011, producing a water ( $\text{H}_2\text{O}$ ) jet of  $24 \pm 3 \mu\text{m}$  in diameter ejected through an orifice of nominally  $20 \mu\text{m}$  in diameter using a back pressure of 12 psi He. A piezoelectric actuator was used to break up the jet into uniform droplets with a diameter of  $40 \pm 6 \mu\text{m}$ , droplet spacing of  $109 \pm 5 \mu\text{m}$ , and a speed of  $11.6 \pm 0.6 \text{ m/s}$ . The droplet formation was observed by an optical microscope using stroboscopic illumination synchronized with the piezoelectric actuator, set to a sine wave form with 8 V amplitude at a frequency of 106 kHz. The outer capillary diameter of  $573 \mu\text{m}$  determined through physical measurement with calipers was used as reference length.

The gas-dynamic virtual nozzle (GDVN) [212] is made from an inner capillary with an inner diameter of 20-40  $\mu\text{m}$ , through which water flows, surrounded by a larger capillary containing a flow of He or  $\text{N}_2$  gas. The gas flow serves as a “virtual nozzle” that focuses the water flowing through the inner capillary, thus producing droplets much smaller than a regular RJ would do. Since clogging of dust particles is a significant problem for capillaries with an inner diameter smaller than 10  $\mu\text{m}$ , the GDVN is effectively designed to produce a stable stream of droplets of 1-10  $\mu\text{m}$  in diameter (depending on the nozzle and pressures used). For the GDVNs, the optical resolution was insufficient to determine  $D_{\text{drop}}$  and  $l_{\text{drop-drop}}$  *in situ*, and the nozzles were therefore characterized *ex situ* in near identical setups.

The GDVN used in Feb 2011 in Papers II-III was characterized after the experiment by high-resolution optical microscopy at identical pressures and driving frequencies (as shown in Fig. 4.4), measuring a droplet diameter of  $9.7 \pm 0.8 \mu\text{m}$ , jet diameter of  $8.1 \pm 0.8 \mu\text{m}$ , and droplet spacing of  $41 \pm 2 \mu\text{m}$  at a flow rate of  $17 \pm 2 \mu\text{l/min}$  (see Table 4.2). However, the measured val-



ues were not consistent with Eqs. (4.3)-(4.5), indicating illumination-related distortions of the optical image. The droplet parameters were therefore estimated by fitting Eqs. (4.3)-(4.5) to the measured droplet parameters, yielding droplet diameters of  $12.2\text{--}13.9\text{ }\mu\text{m}$  with speeds varying from  $5.5$  to  $9.9\text{ m/s}$  (see Table 4.3). Based on experimental overlap in the principal maximum of the elastic structure factor with synchrotron data from SSRL (see Section 5.3.7), the conservative best fit yielding a droplet diameter of  $12.4\text{ }\mu\text{m}$  and droplet speed of  $9.9\text{ m/s}$  was chosen to be used with an uncertainty of  $\pm 5\%$  for the final temperature calibration of the data series (see Table 4.4).

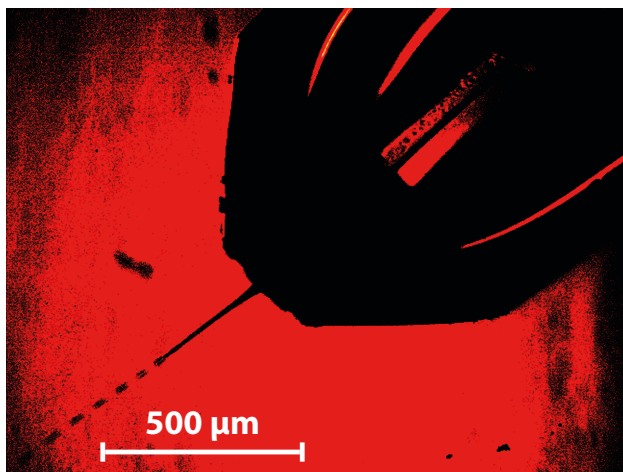


**Figure 4.4:** The GDVN used during the CXI experiment in Feb 2011, producing a water ( $\text{H}_2\text{O}$ ) jet of  $8.1 \pm 0.8\text{ }\mu\text{m}$  in diameter by means of a focusing gas sheath of  $\sim 490\text{ psi}$   $\text{N}_2$  gas that acted as a “virtual nozzle”. The back pressure in the liquid line was  $\sim 210\text{ psi}$  Ar gas. A piezoelectric actuator drove the break-up of the jet into uniform droplets with a diameter of  $9.7 \pm 0.8\text{ }\mu\text{m}$  and droplet spacing of  $41 \pm 2\text{ }\mu\text{m}$  at a flow rate of  $17 \pm 2\text{ }\mu\text{l/min}$ . The droplet formation was observed by an optical microscope using stroboscopic illumination synchronized with the piezoelectric actuator, set to a sine wave form with  $10\text{ V}$  amplitude at a frequency of  $201\text{ kHz}$ . The outer capillary diameter of  $1001\text{ }\mu\text{m}$  determined through physical measurement with calipers was used as reference length.

The GDVNs from Oct 2012 in Paper VI and Jan 2013 in Papers II-III were characterized prior to use at LCLS in a scanning electron microscope (SEM) without using a piezoelectric actuator to drive the breakup. Jet diameters of  $2.2$  and  $3.6\text{ }\mu\text{m}$  were measured at volume flow rates of  $3.2$  and  $18\text{ }\mu\text{l/min}$ , implying droplet speeds of  $14$  and  $29\text{ m/s}$ , respectively, according to Eq. (4.3). It was not possible to characterize the droplets at experimental conditions. However, the experimental droplet parameters can be estimated through Bernoulli’s law for an inviscid, incompressible flow. Since the gas

acts as a “virtual nozzle” around the liquid, the internal pressure in the liquid jet, according to Newton’s third law of motion, is equivalent to the gas pressure surrounding the jet (neglecting surface tension effects). During the x-ray scattering experiment in Papers II-III, the  $N_2$  gas pressure was 200 psi compared to SEM conditions at 470 psi, whereas the He gas pressure during the x-ray emission measurements in Paper VI was identical to SEM conditions (so Bernoulli’s law is not needed). Assuming the liquid has the same density at both pressures and that the change in potential energy due to gravitational forces between the two setups is negligible, the jet speed  $v_1$  for a setup at pressure  $P_1$  can be estimated by

$$v_1 = v_2 \sqrt{\frac{P_1}{P_2}}, \quad (4.6)$$

where  $v$  indicates the jet speed and  $P$  indicates the internal pressure for respective setup. Taking  $v_2$  as 29 m/s,  $P_2$  as 470 psi, and  $P_1$  as 200 psi,  $v_1$  becomes 19 m/s for the GDVN used in Jan 2013. The exponent of 1/2 for the pressure dependence on speed in Eq. (4.6) neglects shear forces exerted on the liquid by the gas [213], which would make the exponent approach unity. Since it was not possible to quantify these effects with the present nozzle and they have been suggested to be small for water jets down to the micron scale [213], we have chosen to use the conservative estimate from Bernoulli’s law, resulting in a higher speed and thus a higher estimate of temperature (see Section 5.3). From the *in situ* measured volume flow rates of 3.57 and 18.64  $\mu\text{l}/\text{min}$  and droplet frequency of 900 kHz, droplet diameters of 5.02 and 8.70  $\mu\text{m}$ , respectively, could be obtained using Eq. (4.4). For the GDVN used in Jan 2013, the droplet diameter was verified through calibration of its ice formation temperature (see Section 5.3.7 for details). For the GDVN used in Oct 2012, no such verification could be made as the low count rate only allowed one data set to be recorded. Other droplet parameters could be calculated using Eq. (4.3) and (4.5) (see Table 4.4).

The pressure increase  $\Delta P$  inside the water droplets due to the Laplace pressure can be determined from a simple force balance (performed on half of the droplet) as

$$\Delta P = \frac{4\Gamma}{D_{\text{drop}}}, \quad (4.7)$$

where  $\Gamma$  is the surface tension of water ( $\Gamma = 0.0756 \text{ N/m}$  at 273 K, usually denoted  $\gamma$  but altered here so as not to be confused with the relativistic factor in Section 4.2.1 or the evaporation coefficient presented in Section 5.3.1). We thus estimate the inner pressure of the RJ and the GDVN droplets to be  $\sim 0.08 \text{ atm}$  and 0.3-0.6 atm above the steady-state chamber pressure  $P_0$ , respectively. Since the structure of water is thought to be insensitive to such

small variations in pressure, we assume that the experimental data measured with the RJ and GDVN droplets are representative of atmospheric pressure.

**Table 4.1:** Experimental droplet parameters determined through *in situ* optical microscopy for LCLS data series recorded with the RJ. Note that enforcing experimental overlap with synchrotron data from SSRL later narrowed the errors in  $D_{drop}$  and  $v$  (see Section 5.3.7), resulting in the reported droplet diameters in Paper II.

LCLS data series	34 $\mu\text{m}$ droplets	37 $\mu\text{m}$ droplets
recorded	Feb 2011	Feb 2011
back pressure (psi)	0 (He)	12 (He)
$f$ (kHz)	69	106
amplitude (V)	8	8
$D_{jet}$ ( $\mu\text{m}$ )	$14 \pm 4$	$24 \pm 3$
$D_{drop}$ ( $\mu\text{m}$ )	$37 \pm 9$	$40 \pm 6$
$l_{drop-drop}$ ( $\mu\text{m}$ )	$198 \pm 7$	$109 \pm 5$
$Q$ ( $\mu\text{l}/\text{min}$ ) <sup>a</sup>	$110 \pm 30$	$218.5 \pm 0.8$
$v$ (m/s) <sup>b</sup>	$13.6 \pm 0.5$	$11.6 \pm 0.6$
$f_R$ (kHz)	$230 \pm 70$	$110 \pm 20$
$D_R$ ( $\mu\text{m}$ )	$26 \pm 7$	$46 \pm 7$
$P_0$ (Torr)	$2.0 \times 10^{-3}$	$3.0 \times 10^{-3}$
$P_0 + \Delta P$ (bar) <sup>c</sup>	0.09	0.08

<sup>a</sup>Calculated from  $f$  and  $D_{drop}$  using Eq. (4.4), uncertainties are propagated independently (root-sum-squared).

<sup>b</sup>Calculated from  $f$  and  $l_{drop-drop}$  using Eq. (4.5), uncertainties are propagated independently (root-sum-squared).

<sup>c</sup>Calculated using Eq. (4.7) for the droplet diameters obtained after the final temperature calibration.

**Table 4.2:** Experimental droplet parameters determined through *ex situ* optical and electron microscopy for the GDVNs. The SEM had no ability to drive the droplet break-up, which is why there are no droplet parameters given for the electron microscopy measurements (marked as not available, n/a).

LCLS data series	5 $\mu\text{m}$ droplets	9 $\mu\text{m}$ droplets	12 $\mu\text{m}$ droplets
measured	<i>ex situ</i> , Oct 2012	<i>ex situ</i> , Jan 2013	<i>ex situ</i> , Feb 2011
gas pressure (psi)	330 (He)	470 ( $\text{N}_2$ )	490 ( $\text{N}_2$ )
back pressure (psi)	550 (He)	490 (He)	230 (Ar)
$f$ (kHz)	n/a	n/a	201
amplitude (V)	n/a	n/a	10
$D_{jet}$ ( $\mu\text{m}$ )	2.2	3.6	$8.1 \pm 0.8$
$D_{drop}$ ( $\mu\text{m}$ )	n/a	n/a	$9.7 \pm 0.8$
$l_{drop-drop}$ ( $\mu\text{m}$ )	n/a	n/a	$41 \pm 2$
$Q$ ( $\mu\text{l}/\text{min}$ )	3.2	18	$17 \pm 2$
$v$ (m/s) <sup>a</sup>	14	29	$6 \pm 1$

<sup>a</sup>Calculated from  $D_{jet}$  and  $Q$  using Eq.(4.3), uncertainties are propagated independently (root-sum-squared) for the 12  $\mu\text{m}$  droplets.

**Table 4.3:** Least-squares fits of Eqs. (4.3)-(4.5) to the *ex situ* determined droplet parameters for the GDVN used in Feb 2011. The initial guess for each parameter was set equal to the experimentally determined droplet parameters for  $12\mu\text{m}$  droplets given in Table 4.2. The residuals denote the difference from the initial guess for each fit, *i.e.* residual + fit = initial guess, taken from Table 4.2. The scores, which are the values minimized by the least-squares fitting routine, were calculated by taking the residuals normalized by respective initial guess times a weight factor, such that *e.g.* a frequency of 278 Hz with a weight factor of  $10^{-3}$  would yield a score of  $(278 - 201) \div 201 \times 10^{-3} = 3.8 \times 10^{-4}$ . The weights should resemble the relative accuracy in each initial guess to obtain an accurate fit.

Weights	fit #1	fit #2	fit #3
$f$	0.1	10	0.1
$D_{jet}$	1	1	1
$D_{drop}$	1	1	1
$l_{drop-drop}$	1	1	1
$Q$	0.1	10	1
$v$	0.1	10	0.1
Residuals	fit #1	fit #2	fit #3
$f$ (kHz)	13	0	-77
$D_{jet}$ ( $\mu\text{m}$ )	2.4	0	2.2
$D_{drop}$ ( $\mu\text{m}$ )	-2.4	-4.2	-2.7
$l_{drop-drop}$ ( $\mu\text{m}$ )	5	14	5
$Q$ ( $\mu\text{l}/\text{min}$ )	6.3	0	0.3
$v$ (m/s)	-1.3	0	-4.4
Best fits	fit #1	fit #2	fit #3
$f$ (kHz)	188	201	278
$D_{jet}$ ( $\mu\text{m}$ )	5.7	8.1	5.9
$D_{drop}$ ( $\mu\text{m}$ )	12.1	13.9	12.4
$l_{drop-drop}$ ( $\mu\text{m}$ )	36	27	36
$Q$ ( $\mu\text{l}/\text{min}$ )	10.6	16.9	16.6
$v$ (m/s)	6.8	5.5	9.9

**Table 4.4:** Corrected experimental droplet parameters for LCLS data series recorded with GDVNs in Papers II-III and VI.

LCLS data series	5 $\mu\text{m}$ droplets	9 $\mu\text{m}$ droplets	12 $\mu\text{m}$ droplets <sup>a</sup>
recorded	Oct 2012	Jan 2013	Feb 2011
gas pressure (psi)	330 (He)	200 (N <sub>2</sub> )	490 (N <sub>2</sub> )
back pressure (psi)	800 (He)	490 (He)	210 (Ar)
$f$ (kHz)	900	900	$280 \pm 10$
amplitude (V)	50	20	10
$D_{jet}$ ( $\mu\text{m}$ ) <sup>b</sup>	2.3	4.5	$5.9 \pm 0.3$
$D_{drop}$ ( $\mu\text{m}$ ) <sup>c</sup>	5.02	8.70	$12.4 \pm 0.6$
$l_{drop-drop}$ ( $\mu\text{m}$ ) <sup>d</sup>	15.6	21	$36 \pm 2$
$Q$ ( $\mu\text{l}/\text{min}$ )	3.57	18.64	$16.6 \pm 0.8$
$v$ (m/s) <sup>e</sup>	14	19	$9.9 \pm 0.5$
$f_R$ (kHz)	1300	930	$370 \pm 40$
$D_R$ ( $\mu\text{m}$ )	4.3	8.5	$11.2 \pm 0.6$
$P_0$ (Torr)	$(1.7 \pm 0.2) \times 10^{-3}$	$4.5 \times 10^{-4}$	$1.0 \times 10^{-3}$
$P_0 + \Delta P$ (bar)	0.6	0.3	0.2

<sup>a</sup>The corrected values of  $f$ ,  $D_{jet}$ ,  $D_{drop}$ ,  $l_{drop-drop}$ ,  $Q$ , and  $v$  were determined through least-squares fit#3 (see Table 4.3) of Eqs. (4.3)-(4.5) to the *ex situ* determined droplet parameters (see Table 4.2) with an uncertainty of  $\pm 5\%$ .

<sup>b</sup>Calculated from  $Q$  and  $v$  using Eq. (4.3), except for the 12  $\mu\text{m}$  droplets<sup>a</sup>.

<sup>c</sup>Calculated from  $Q$  and  $f$  using Eq. (4.4), except for the 12  $\mu\text{m}$  droplets<sup>a</sup>.

<sup>d</sup>Calculated from  $v$  and  $f$  using Eq. (4.5), except for the 12  $\mu\text{m}$  droplets<sup>a</sup>.

<sup>e</sup>Propagated to experimental conditions using Eq. (4.6), except for the 12  $\mu\text{m}$  droplets<sup>a</sup>.

# Chapter 5

## Analysis

In this chapter, data analysis of the experimental methods used in Papers I-VI will be described. The chapter will focus on the aspects where my contribution was noteworthy and that are important for the main results summarized in Chapter 6. The interested reader is referred to the papers for further details. Specifically, I will focus on the analysis presented in the supplementary information of Paper II, where parts of Sections 5.1 and 5.3 are taken from, but the sections will include details beyond what was stated in the supplementary information and also include the droplet dispenser used in Paper VI.

### 5.1 Analysis of Diffraction Patterns

In this section, I will explain the corrections that have been applied to data to obtain publishable quality. In addition, I will go through the procedures used to extract the structure factor from the intensities and how to relate it to the real-space structure in terms of the PCF.

#### 5.1.1 Corrections to Synchrotron Data

Three experimental corrections were performed to extract the elastic signal from the raw scattering intensities measured at BL 7-2, SSRL, in Paper I. First, a scattering background correction was performed, which is mainly due to air scattering and detector dark signal. Second, the polarization of the beam was corrected using Eq. (5.2) for a horizontally polarized incident beam with 5% fraction of a vertical component), *i.e.*  $c_{horz} = 0.95$ ,  $c_{vert} = 0.05$ ; the one-dimensional (1D) path taken by the diffractometer corresponds to  $\phi = 0^\circ$  and  $\theta$  ranging between  $3$ - $135^\circ$ . Last, optical aberrations of the analyzer crystal due to the finite size of the water jet and in-plane beam focus were taken into

account. The re-scale factors corresponding to these three corrections and the modified raw data on a logarithmic scale are shown in Fig 5.1. We also note that the correction accounting for multiple-scattering effects is negligible in our current experiment due to the small sample dimension. The attenuation length of x-rays is approximately 9 mm at 17 keV, so absorption can also safely be neglected.

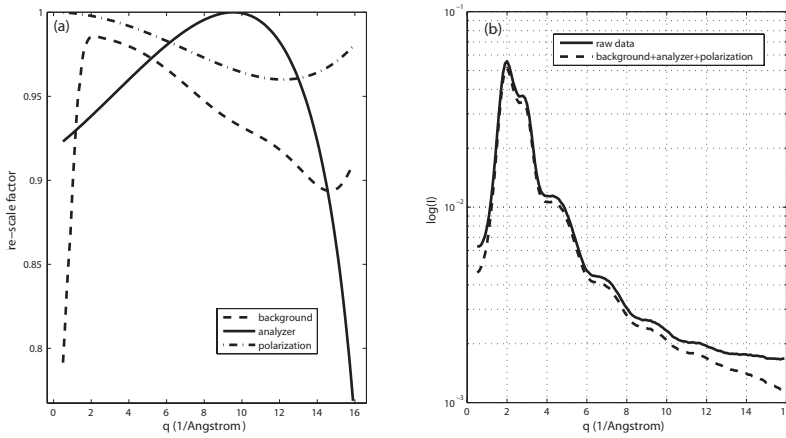


**Figure 5.1:** (a) Re-scale factors of measured scattering intensity due to the contributions from air scattering background (dashed line), the optical aberration of the Ge analyzer crystal (solid line), and the polarization of the incident x-ray beam (dash-dotted line). (b) Comparison between the raw data of scattering intensity (solid line) and the data after the three corrections (dashed line) shown in (a) with a logarithmic scale for liquid water at 280 K. The figure is reproduced from Paper I by permission of the PCCP Owner Societies.

For the scattering patterns recorded at BL4-2, SSRL, in Paper II, background subtraction was performed on the 2D image by separately measuring the scattering from the empty quartz capillary. A solid angle correction comparable to Eq. (5.3) was employed and the angularly averaged intensity  $I(q)$  was normalized to electron units described in Section 5.1.4. Compton scattering was also removed theoretically from the normalized  $I(q)$  through a polynomial (3<sup>rd</sup> order) least-squares fit to high-level (single and double excitation configuration interaction) quantum chemical calculations from Wang *et al.* [214], yielding

$$I(q)_{\text{Compton}} = -0.080279 + 1.7788q - 0.060148q^2 - 0.0031625q^3. \quad (5.1)$$



### 5.1.2 Corrections to the Cornell-SLAC Pixel Array Detector

The LCLS data in Papers II-III were recorded on a  $\sim 1516 \times 1516$  pixel array detector developed by Cornell University and SLAC (CSPAD) with a dynamic range of 10000 [215,216]. The CSPAD consists of 64 application-specific integrated circuits (ASICs) made up by  $185 \times 194$  pixels each covering an area of  $109.92 \times 109.92 \mu\text{m}^2$ . The CSPAD was located 139 mm in Feb 2011 and 132 mm in Jan 2013 downstream of the interaction region where the direct beam passed through its central hole. In both experiments, the CSPAD version 1.0 was used.

The corrections to the raw images of the CSPAD were developed and implemented as modules in C++ to the standard analysis framework\* at LCLS. The code base through which all the single-shot corrections in Papers II-III (summarized below) were performed, has been developed into the framework-independent data processing program Cheetah [217], which is led by Anton Barty at DESY, Germany, and is available online† for public use.

Several corrections had to be applied to the raw data before the structural information of the illuminated sample could be extracted. First, the average readout value when no x-rays are present, known as the dark signal, was subtracted for each pixel (see Fig. 5.2 left). This is measured in analogue-to-digital units (ADUs) and is between 1000 and 1600 ADUs for well-behaved pixels. The noise associated with the dark subtraction can be quantified by the standard deviation of the readout value when no x-rays are present (see Fig. 5.2 right). It is primarily made up by a frame-wise-variable pedestal contribution uniform for the pixels within each ASIC as well as the electronic noise of each individual pixel (dark noise in terms of thermally induced electron-hole splitting is negligible), and it is generally smaller than the detector response of a single photon (roughly 10 ADUs for 9.4 keV photons). After these corrections had been performed, the detector response was re-scaled on a pixel basis using a normalized gain correction. The gain correction was calculated from a linear fit of the average readout value of each individual pixel as a function of photon flux from flat-field Cu fluorescence (including a geometric correction) *in situ* at CXI with varying attenuation, covering a range from nearly zero to about 700 ADUs.

The geometry of the CSPAD was assembled in several steps. The CSPAD is comprised by four quadrants, each one containing 16 ASICs. The ASICs are put together in elements containing two ASICs each (separated by a distance of 3 pixels), whose corner positions were calibrated through an optical measurement using silicon sensors. For the Feb 2011 experiment, the quadrant positions were aligned by establishing the continuity of dark lines created

---

\*<https://confluence.slac.stanford.edu/display/PCDS/Data+Analysis>

†<http://www.desy.de/~barty/cheetah/Cheetah/Welcome.html>

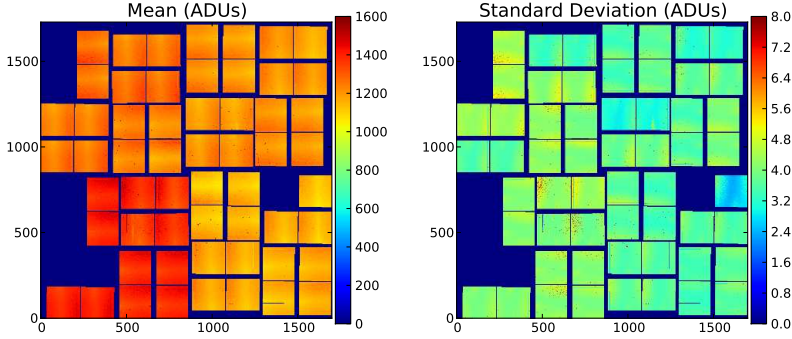


**Figure 5.2:** Average readout (left) and variance (right) in ADUs for each pixel when no x-rays are present. The mean value is between 1000 ADUs and 1600 ADUs and the standard deviation is below 7 ADUs for well-behaved pixels.

by the illumination of 0.5 mm diameter W wires, which did not transmit the incident x-rays and spanned the face of the detector. The center position of the FEL beam (with respect to the CSPAD) was calibrated by optimizing the sharpness of the Si(111) Bragg reflection using a circular Hough transform. For the Jan 2013 experiment, the W wires had been removed and the quadrant positions as well as the center position were instead calibrated by optimizing the overlap between (*i.e.* maximizing the product of) the angularly integrated intensities of the ice  $I_h$  Bragg reflections for each quadrant.

The linear polarization of the FEL beam reduces the scattering at high angles according to classical electrodynamics [20]. To correct for the horizontally polarized FEL beam, the intensity of each pixel was divided by [183]

$$\alpha_{pol} = c_{horz} \left[ 1 - \sin^2 \phi \sin^2 \theta \right] + c_{vert} \left[ 1 - \cos^2 \phi \sin^2 \theta \right], \quad (5.2)$$

where  $c_{horz}$  is the fraction of horizontal polarization (in this case 100%),  $c_{vert} = 1 - c_{horz}$  is the fraction of vertical polarization (in this case 0%),  $\phi$  is the azimuthal angle of the pixel, and  $\theta$  is the scattering angle of the pixel. The polarization correction removes the azimuthal dependence of the isotropic scattering of the liquid. Furthermore, the difference in solid angle spanned by different pixels in the scattering geometry has to be taken into account. This was done by calculating the solid angle of each individual pixel, which can be split up into two plane triangles whose solid angle is known [218] to be

$$\Omega = 2 \tan^{-1} \left[ \frac{|\mathbf{R}_1 \mathbf{R}_2 \mathbf{R}_3|}{R_1 R_2 R_3 + (\mathbf{R}_1 \cdot \mathbf{R}_2) R_3 + (\mathbf{R}_1 \cdot \mathbf{R}_3) R_2 + (\mathbf{R}_2 \cdot \mathbf{R}_3) R_1} \right], \quad (5.3)$$

where  $\mathbf{R}_1, \mathbf{R}_2, \mathbf{R}_3$  are the vectors of the vertices of the plane triangle with corresponding magnitudes  $R_1, R_2, R_3$ ,  $|\mathbf{R}_1 \mathbf{R}_2 \mathbf{R}_3|$  is the (positive) scalar triple product, and  $\mathbf{R}_1 \cdot \mathbf{R}_2$  denotes the scalar product between  $\mathbf{R}_1$  and  $\mathbf{R}_2$ . The solid angle of each pixel is roughly proportional to  $\cos^3 \theta$ , where  $\theta$  is the scattering angle of the pixel. Moreover, the scattering angle was used to calculate the magnitude of the momentum transfer  $q$  for each pixel on a shot-by-shot basis by

$$q = \frac{4\pi}{\lambda} \sin\left(\frac{\theta}{2}\right), \quad (5.4)$$

where  $\lambda$  is the wavelength of the FEL shot, from which the angular average of the intensity was computed.  $\lambda$  is calculated from the peak current and the relativistic energy of the electron beam, and the method accurately describes relative changes in wavelength. The absolute wavelength has to be calibrated from a reference sample at several detector positions, but is to first order corrected by the sample-detector distance  $R^\parallel$  calculated during geometry calibration, since it uses the computed  $\lambda$  and the Taylor expansion of  $\frac{4\pi}{\lambda} \sin\left(\frac{\theta}{2}\right) = \frac{4\pi}{\lambda} \sin\left(\frac{\tan^{-1}(R^\perp/R^\parallel)}{2}\right) \approx \frac{4\pi}{\lambda} \sin\left(\frac{R^\perp/R^\parallel + O((R^\perp/R^\parallel)^3)}{2}\right) \approx \frac{2\pi R^\perp}{\lambda R^\parallel} + O\left(\frac{(R^\perp/R^\parallel)^3}{\lambda}\right)$ , where  $R^\perp$  and  $R^\parallel$  are the magnitudes of the components of  $\mathbf{R}$  perpendicular and parallel to the FEL beam, respectively. Thus, it is to first order sufficient to determine the product  $\lambda R^\parallel$ , which was effectively done during geometry calibration. The error in  $q$  due to the  $O\left(\frac{(R^\perp/R^\parallel)^3}{\lambda}\right)$  term is expected to be smaller than the  $\sim 0.2\%$  BW of the FEL beam, resulting in a broadening of the  $q$  resolution corresponding to  $\sim 0.006 \text{ \AA}^{-1}$  at  $3 \text{ \AA}^{-1}$ . Nevertheless, the data were splined with  $0.001 \text{ \AA}^{-1}$  resolution prior to averaging to account for the energy jitter by the FEL beam, which had a standard deviation of 15-25 eV at 9.4 keV.

Finally, pixels with anomalous behavior were masked out, slightly reducing the solid angle probed by the detector. Masking out seven of the ASICs that were not operational during the experiment in Feb 2011, the borders of each ASIC that accumulate more charge than the rest of the detector, the shadows of the W wires in front of the detector (as well as other anomalous pixels) removed 419671 pixels (18.3%). Additionally, pixels with a standard deviation of the dark readout value larger than 6 ADUs (resulting in 95% accuracy of single-photon detection if a Gaussian distribution of dark readout values is assumed) and pixels with a gain 25% higher or 25% lower than the nominal value were masked out. In total, this results in that 427779 pixels (18.6%) were masked out from the data set. After all corrections were applied, the data quality was notably improved (see Fig. 5.3). For the Jan 2013 experiment, all ASICs were operational and there were no W wires in front of the detector, which reduced the number of masked pixels. In total, 123793

pixels (5.4 %) were masked out from the data set, corresponding to pixels with a standard deviation of the dark readout value larger than 3.4 ADUs or smaller than 1.58 ADUs (15087 pixels), pixels along the border of each ASIC (96000 pixels), non-bonded pixels (1216 pixels), as well as other anomalous and shadowed pixels.

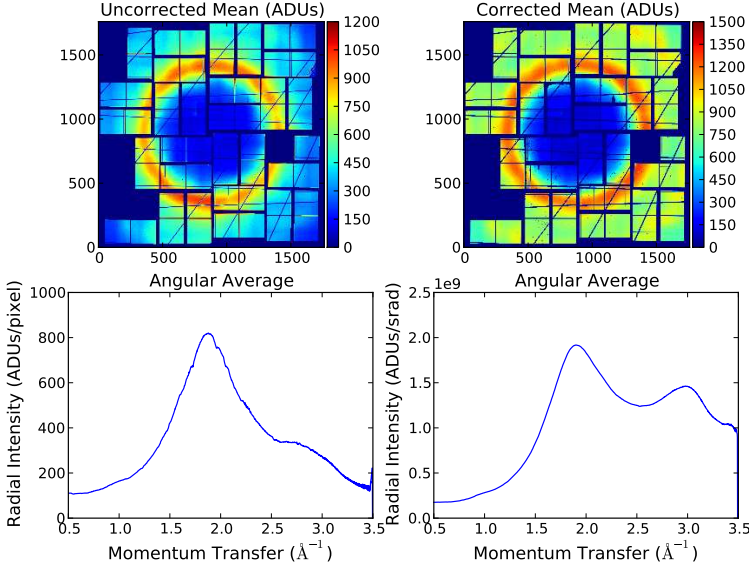


**Figure 5.3:** The assembled scattering patterns and angular averages of  $37\text{ }\mu\text{m}$  diameter water droplets 20.79 mm away from the nozzle using the RJ. The patterns show a comparison of the mean intensity of 100 hits for uncorrected (only dark subtracted) and fully corrected data (dark subtracted, gain corrected, polarization corrected, solid-angle corrected, and with anomalous pixels masked out). It is evident that the angular average is notably improved by the corrections and that the splitting of the water scattering peak becomes visible after these corrections. Any streaks seen over the ASICs in the assembled scattering patterns are artifacts from interpolation when visualizing the images and are not included in the angular averages.

### 5.1.3 Sorting of Scattering Data

After the raw data had been properly corrected as described above, hits were selected out of the data stream and sorted based on their scattering patterns. As each measurement point contained between  $2 \times 10^5$  and  $1 \times 10^6$  shots, the hit selection process had to be fully automatic. A simple threshold algorithm

initially detected all water and ice hits with more than 5000 pixels above 50 ADUs (water biased) or more than 50 pixels above 500 ADUs (ice biased). These ensembles contained many weak hits from the mist of nanoscale water and ice particles that were created around the primary droplets. By sorting the hits based upon the integrated intensity of the angular average, the weak hits could be successfully eliminated (see Fig. 5.4). The remaining hits contained pure water scattering, pure ice scattering, as well as a mixture of both water and ice scattering.

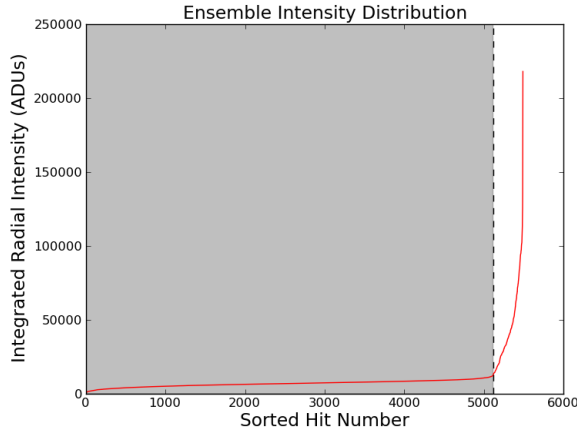


**Figure 5.4:** Ensemble intensity distribution after initial hit detection for  $12\text{ }\mu\text{m}$  water droplets 40.40 mm away from the nozzle using the GDVN. The ensemble contained many weak hits from the mist of nanoscale water and ice particles surrounding the primary droplets (marked by the shaded area), which could effectively be removed from the ensemble by sorting the hits after the integrated intensity of the angular average. Only the hits to the right of the dashed line were kept for further analysis.

To remove any influence of ice scattering from the water ensembles in Paper II, only the hits containing pure water scattering were kept for further analysis. This was effectively done by sorting the intensity of the angular average by the gradient maximum, which specifically detects the sharp intensity variation of Bragg peaks, after applying a (5 pixel wide) moving median filter (see Fig. 5.5). Note that the filter was implemented only for this sorting step to remove spurious intensity gradients from residual bright, faulty pixels or non-signal regions on the detector. Such a filter was not applied to any of the final data shown or analyzed in the present thesis. Finally, a small fraction of the data that showed gradients in their angular-averaged scattering intensities beyond what is expected of those from the

water ring had to be manually sorted. This final inspection was performed on the 2D scattering patterns of individual hits to identify the presence or absence of Bragg reflections expected of crystalline ice. The hits containing ice were kept for further analysis in Paper III.

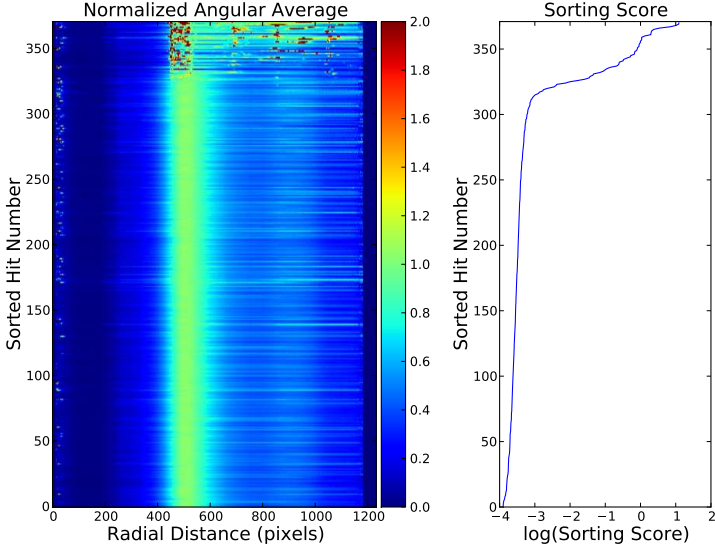


**Figure 5.5:** Sorted spectrum of an ensemble of strong hits for  $12\ \mu\text{m}$  diameter water droplets 40.40 mm away from the nozzle using the GDVN. The ensemble was sorted by the gradient maximum (after applying a 5 pixel wide moving median filter) of the radial intensity for each hit. The hits with a high sorting score (seen at the upper part of the spectrum) contained ice, as evidenced by the sharp peaks observed in the normalized angular average, whereas the rest of the hits only contained pure water.

The water droplets produced by the RJ displayed hit rates between 1-10% (see Table 5.1) and contained no significant fraction of ice hits due to the higher droplet temperatures. The droplets produced by the GDVNs, however, showed an increasing fraction of ice hits as the distance between the nozzle and the interaction region was increased beyond  $\sim 35\ \text{mm}$  (see Tables 5.2 and 5.3). The hit rates of the GDVNs (see Table 5.2) were slightly lower than those for the RJ, but all data points (including the RJ) where ice hits were in minority contained ensembles of at least 1000 water hits. Only pure water hits were kept for analysis of the structure factor, described in Section 5.1.4.

**Table 5.1:** Data statistics for different sample-nozzle distances using the RJ in Feb 2011. Number of total hits denotes all pure water hits that made it through data selection. As no significant fraction of ice hits was observed for the RJ and the 34-37  $\mu\text{m}$  diameter droplets had a noteworthy increase in scattering cross section compared to the 12  $\mu\text{m}$  droplets, the thresholds for automatic sorting were set more conservatively to avoid manual sorting. The hit rates (and number of total hits) of the RJ are therefore slightly lower than actual hit rates observed during the experiment.

Sample-nozzle distance (mm)	Number of total hits	Hit rate (%)
10.01	7860	7.17
15.80	3900	10.08
20.79	3580	9.71
30.01	3000	6.01
30.74	2280	4.66
40.76	2705	2.01
60.71	1880	2.32
70.66	1820	0.79

**Table 5.2:** Data statistics for different sample-nozzle distances for the 12  $\mu\text{m}$  diameter water droplets produced by the GDVN in Feb 2011. Number of total hits denotes all water and ice hits that made it through data selection. The ice ratio includes all hits that do not exhibit pure water scattering (*i.e.* hits with partial ice scattering upon a water background as well as hits with pure ice scattering).

Sample-nozzle distance (mm)	Number of total hits	Hit rate (%)	Ice ratio (%)
12.35	10150	4.87	0.07
21.41	15713	5.27	0.07
30.60	9295	1.73	0.13
40.40	6339	0.62	18.14
45.60	5142	0.58	83.59
50.62	3600	1.31	97.08

**Table 5.3:** Data statistics for different sample-nozzle distances for the  $9\mu\text{m}$  diameter water droplets produced by the GDVN in Jan 2013. Number of total hits denotes all water and ice hits that made it through data selection. The ice ratio includes all hits that do not exhibit pure water scattering (*i.e.* hits with partial ice scattering upon a water background as well as hits with pure ice scattering).

Sample-nozzle distance (mm)	Number of total hits	Hit rate (%)	Ice ratio (%)
25.88	15208	2.81	0.06
36.04	3754	1.06	4.85
50.62	2455	0.69	18.29



### 5.1.4 Analysis of Structure Factors and PCFs

The water structure in Paper I was analyzed on a per-molecule basis. A quantum mechanically calculated MSF of an isolated H<sub>2</sub>O molecule [214] was employed to separate the scattering structure factor  $S(q)$  from the total scattering intensity by using Eq. (2.49) under the assumption that  $\langle F(q) \rangle^2 \approx \langle F(q)^2 \rangle$ . Two important analysis steps were performed before Eq. (2.43) could be applied to derive the molecular PCF. First a proper normalization constant had to be found to relate  $I(q)$  uniquely to  $S(q)$ . There are two widely used approaches to determine the normalization factor: the large-angle method and the integral method [219].

The large-angle (*i.e.* scattering angle) method relies on the fact that the normalized intensity oscillates around the independent MSF with decreasing amplitude at large  $q$  [31]. To show this, we recall that  $S(q)$  for an isotropic material (*i.e.* averaged over all orientations in real space) can be written as a sum of sinc functions  $\frac{\sin qr_{kl}}{qr_{kl}}$  using the Debye scattering formula in Eq. (2.33), where  $r_{kl}$  is the distance between the particle pair concerned. It is evident that the sinc functions must oscillate around zero with decreasing amplitude at large  $q$ . The large-angle normalization factor  $K_{norm}^{large-angle}$  is therefore determined in Paper I as

$$K_{norm}^{large-angle} = \left\langle \frac{\langle F(q)^2 \rangle_{\Omega}}{I(q)} \right\rangle_{q \geq 14 \text{ \AA}^{-1}} \quad (5.5)$$

where the inner average is taken in real space over all solid angles  $\Omega$  and the outer average is taken in reciprocal space over all measured momentum transfers above  $14 \text{ \AA}^{-1}$ .

The second method is the integral method [220,221], which is based on the fact that no water molecule can overlap. This means that  $g(r) \rightarrow 0$  as  $r \rightarrow 0$ , which we can utilize in Eq. (2.43) to obtain

$$\begin{aligned} \lim_{r \rightarrow 0} g(r) &= 1 + \lim_{r \rightarrow 0} \frac{1}{2\pi^2 \rho_0 r} \int_0^\infty q S(q) \sin(qr) dq = \quad (5.6) \\ &= \left\{ \sin(qr) \approx qr - (qr)^3/6 + \dots \right\} = 1 + \lim_{r \rightarrow 0} \frac{r}{2\pi^2 \rho_0 r} \int_0^\infty q^2 S(q) dq = \\ &= 1 + \frac{1}{2\pi^2 \rho_0} \int_0^\infty q^2 S(q) dq. \end{aligned}$$

Equating the left-hand side (LHS) of Eq. (5.6) to 0, it can be rewritten using

Eq. (2.49) as

$$-2\pi^2\rho_0 = \int_0^\infty q^2 S(q) dq = \int_0^\infty q^2 \frac{KI(q)/N - \langle F^2 \rangle_\Omega}{\langle F^2 \rangle_\Omega} dq = \quad (5.7)$$

$$= K_{norm} \int_0^\infty q^2 \frac{I(q)}{\langle F^2 \rangle_\Omega} dq - \int_0^\infty q^2 dq \quad (5.8)$$

Thus, we compute the normalization factor  $K_{norm}^{integral}$  in Paper I as

$$K_{norm}^{integral} = \frac{\int_{q_{min}}^{q_{max}} q^2 dq - 2\pi^2\rho_0}{\int_{q_{min}}^{q_{max}} q^2 I(q) / \langle F(q)^2 \rangle_\Omega dq}, \quad (5.9)$$

where the limits of integration have been exchanged by the minimum and maximum momentum transfer measured in Paper I, namely  $q_{min} = 0.5 \text{ \AA}^{-1}$  and  $q_{max} = 15.9 \text{ \AA}^{-1}$ , respectively. Hence, both the large-angle method and the integral method have to be approximated by the limited  $q$ -range. Since the two methods gave similar normalization factors to within 1 % for the data presented in Paper I, we are confident that the measured  $q$ -range is sufficient to accurately normalize the intensity to electron units. In the end, the average of the two normalization factors was used for further analysis.

After a proper normalization has been performed, the finite range of data in  $q$  has to be accounted for, as it is well known that it gives rise to spurious Fourier ripples [34]. We applied an exponentially decaying window function  $e^{-aq^2}$  to decrease the magnitude of the ripples resulting from the truncation errors. We thus used the expression

$$4\pi\rho_0 r^2 g(r) = 4\pi r^2 \rho_0 + \frac{2r}{\pi} \int_0^\infty e^{-aq^2} q S(q) \sin qr dq. \quad (5.10)$$

This increases the smoothness of the data significantly, rendering it possible to observe the correlations at large distances. As a consequence, the data gets artificially broadened, which slightly reduces the first peak in  $g(r)$ , but as the emphasis of the study is on temperature-dependent changes it does not affect the conclusions drawn.

In Paper II, a different approach had to be taken, as the data did not have sufficient  $q$ -range to allow Fourier inversion according to Eq. (2.43). To circumvent Fourier inversion, MD simulations were utilized to compare the split of the principal maximum of the total scattering structure factor and relate it to the changes in the oxygen-oxygen PCF, which will be discussed in detail in Section 6.1. Thus,  $S(q)$  was calculated on a per-atom basis using

$$S(q) = \frac{K_{norm} I(q) - \sum_\alpha c_\alpha f'_\alpha(q)^2}{(\sum_\alpha c_\alpha f'_\alpha(q))^2}, \quad (5.11)$$

where  $f'_\alpha$  are the MAFFs described by Eq.(2.47) for atom  $\alpha$  being either O or H, with corresponding number concentration  $c_O = 1/3$  or  $c_H = 2/3$ , respectively. A charge transfer  $\alpha_H$  of 0.43 electrons from each hydrogen toward the oxygen ( $\alpha_O = 0.1075$  to retain charge neutrality) was used, which has been shown to yield good fits to experimental data previously using the Reverse Monte Carlo technique [170, 222], and  $\delta = 2.01 \text{ \AA}^{-2}$  from fits to a quantum mechanically calculated MSF [214]. However, the limited  $q$ -range of about  $0.5\text{--}3.2 \text{ \AA}^{-1}$  supplied by the fixed detector position did not allow for a rigorous determination of  $K_{norm}$  using neither normalization method described above. Instead, an approximate version of the large-angle method was used in the  $q$ -range  $0.66\text{--}3.26 \text{ \AA}^{-1}$  and adjusted by 0.623 to correct the intensity normalization for the limited  $q$ -range. The correction constant was determined by applying the same approximate normalization to the data set in Paper I and then compare the approximate  $K_{norm}$  over the limited  $q$ -range with what was obtained from Eq. (5.5).

The principal maximum of  $S(q)$  in water around  $q \sim 1.5\text{--}3 \text{ \AA}^{-1}$  splits up into two distinctive peaks denoted  $S_1$  and  $S_2$ , growing sharper and more well-defined upon cooling (see Section 6.1). The  $S_1$  and  $S_2$  peak positions (denoted  $q_1$  and  $q_2$ , respectively) were derived from the maxima of local (5<sup>th</sup> order) polynomial least-squares fits. The error bars were estimated by shifting the derivative of the polynomial fit by an error factor

$$\varepsilon_{dS/dq} = \left| \frac{d^2S}{dq^2} \right| \times \varepsilon_{dq}, \quad (5.12)$$

where  $\varepsilon_{dq}$  is the bin size of  $0.001 \text{ \AA}^{-1}$  (LCLS) and  $0.003 \text{ \AA}^{-1}$  (SSRL) and  $\left| \frac{d^2S}{dq^2} \right|$  is taken to be  $50 \text{ \AA}^2$  for all peaks. The zero of  $dS/dq \pm \varepsilon_{dS/dq}$  is an estimate of the uncertainty in the peak position, which takes the width of the maximum into account. Because the  $S_1$  and  $S_2$  peaks grew sharper and more well-defined upon cooling, the uncertainties in  $q_1$  and  $q_2$  generally became smaller when the temperature decreased.

Prior to applying Eq. (5.11) to the data measured on water droplets at LCLS, one last correction was performed on the angularly averaged intensity corrected according to Section 5.1.2, denoted  $I_{corr}(q)$ . A background subtraction was performed to minimize the influence of upstream beamline components (dominated by scattering from a diamond window) and reduce the effect of Compton scattering on  $I(q)$ . The background was gathered from x-ray shots just missing the droplets, which after smoothening was scaled to half the intensity of  $I_{corr}(q)$  inside the water ring, *i.e.* between  $0.46\text{--}0.61 \text{ \AA}^{-1}$  (dashed lines in Fig. 5.6a). To visualize this background subtraction, it is shown in green for the  $12 \mu\text{m}$  droplets  $45.60 \text{ mm}$  away from the nozzle recorded in Feb 2011 and in purple for the  $9 \mu\text{m}$  droplets  $36.04 \text{ mm}$  away

from the nozzle recorded in Jan 2013 (see Fig. 5.6a). The two data points are determined to lie within 3 K from each other based on the Knudsen theory of evaporation and experimental overlap of ice nucleation (see Tables 5.6 and 5.8) and should therefore have a fairly similar  $S(q)$  profile. It is evident that the data recorded in Jan 2013 with weaker intensity has a much more asymmetric peak shape for  $I_{norm}(q)$ , which results in that  $q_1$  is shifted to higher  $q$  for  $S(q)$  (Fig. 5.6c). This effect is assigned to the non-linearity of the detector at low scattering intensities, which is primarily a problem for the last data points of the GDVNs when ice nucleation occurs frequently and the x-rays have to be attenuated to protect the detector from very intense Bragg peaks of hexagonal ice. The non-linear effects of the detector can be minimized by removing the weakest hits from the water-shots ensemble that have a maximum intensity smaller than 50 ADUs/pixel (corresponding to  $\sim 9 \times 10^7$  ADUs/srad). On the other hand, the different detector position for the  $9 \mu\text{m}$  droplets recorded in Jan 2013 changes the non-linear and non-local detector response for the intensity average slightly, which are then amplified at high  $q$  by the solid angle and polarization correction due to their  $\cos^3(\theta)$  and  $\cos^2(\theta)$  proportionality (where  $\theta$  is the scattering angle), respectively. Thus,  $q_1$  is relatively insensitive to the background subtraction routine, whereas  $q_2$  has a larger uncertainty due to the increasing background with steeper slope that has to be effectively subtracted. By changing the background subtraction for the  $9 \mu\text{m}$  droplet series so that it uses the previously removed weak hits with a maximum intensity smaller than 50 ADUs/pixel the intensity profile at high  $q$  is comparable to the droplet series recorded in Feb 2011 and the relative errors in the  $q_2$  determination are minimized (compare Fig. 5.6c and Fig. 5.7c).

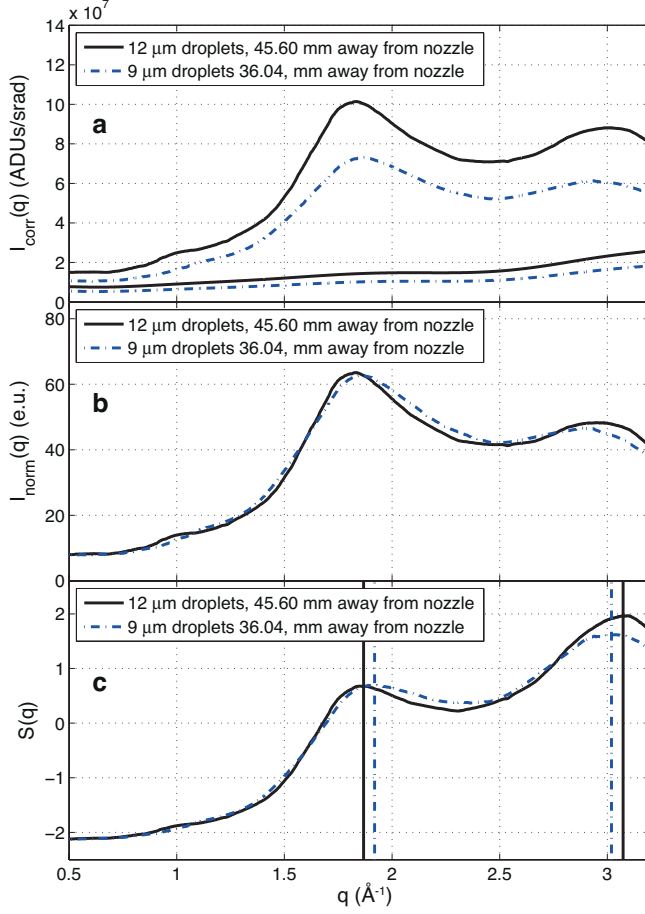


**Figure 5.6:** The angularly integrated intensities  $I(q)$  and derived total scattering structure factor  $S(q)$  for 12  $\mu\text{m}$  diameter water droplets 45.60 mm away from the nozzle (black solid curves) and 9  $\mu\text{m}$  diameter water droplets 36.04 mm away from the nozzle (blue dash-dotted curves) produced by GDVNs in Feb 2011 and Jan 2013, respectively. (a) The single-shot 2D scattering patterns were corrected and averaged as stated in Section 5.1.2 to produce  $I_{\text{corr}}(q)$  for the full water ensembles containing all shots that had an angular average with maximum intensity greater than 20 ADUs (corresponding to  $\sim 4 \times 10^7$  ADUs/srad). The lines with low intensities denote the respective background subtractions made to  $I_{\text{corr}}(q)$ . (b) The normalized corrected angularly integrated intensities  $I_{\text{norm}}(q)$ , which were obtained from background-subtracted  $I_{\text{corr}}(q)$  that were normalized in the  $q$ -range  $0.66\text{--}3.26 \text{ \AA}^{-1}$ . (c) The resulting interatomic total scattering structure factor  $S(q)$  obtained from  $I_{\text{norm}}(q)$  using Eq. (5.11). The vertical lines indicate  $q_1$  and  $q_2$  derived from the maxima of local (5<sup>th</sup> order) polynomial least-squares fits.

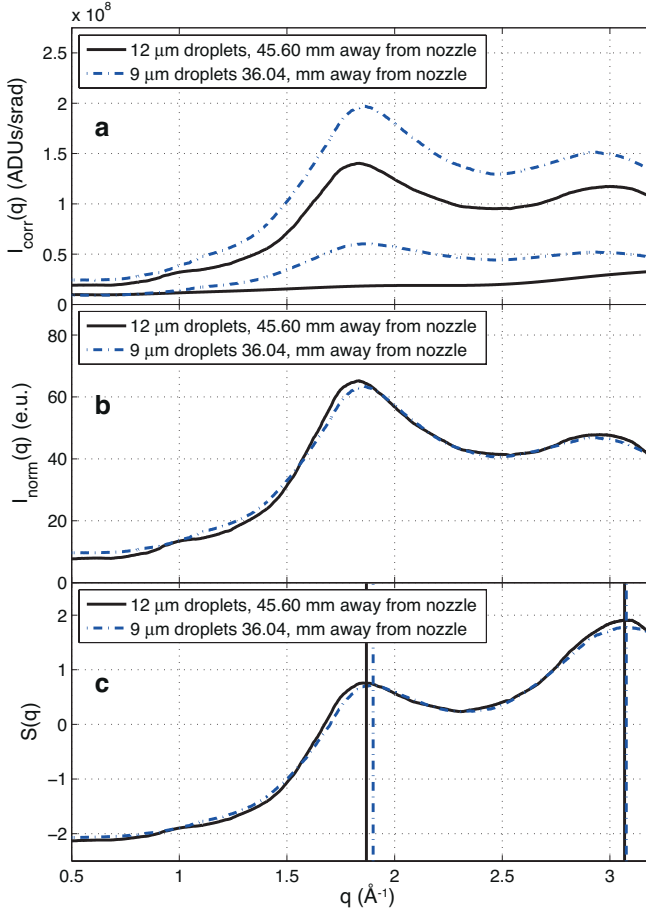


**Figure 5.7:** The angularly integrated intensities  $I(q)$  and derived total scattering structure factor  $S(q)$  for  $12\ \mu\text{m}$  diameter water droplets  $45.60\ \text{mm}$  away from the nozzle (black solid curves) and  $9\ \mu\text{m}$  diameter water droplets  $36.04\ \text{mm}$  away from the nozzle (blue dash-dotted curves) produced by GDVNs in Feb 2011 and Jan 2013, respectively. (a) The single-shot 2D scattering patterns were corrected and averaged as stated in Section 5.1.2 to produce  $I_{\text{corr}}(q)$  for the full water ensembles containing all shots that had an angular average with maximum intensity greater than 50 ADUs (corresponding to  $\sim 9 \times 10^7$  ADUs/srad). The lines with low intensities denote the respective background subtractions made to  $I_{\text{corr}}(q)$ . (b) The normalized, corrected angularly integrated intensities  $I_{\text{norm}}(q)$ , which was obtained from background-subtracted  $I_{\text{corr}}(q)$  that were normalized in the  $q$ -range  $0.66$ – $3.26\ \text{\AA}^{-1}$ . (c) The resulting interatomic total scattering structure factor  $S(q)$  obtained from  $I_{\text{norm}}(q)$  using Eq. (5.11). The vertical lines indicate  $q_1$  and  $q_2$  derived from the maxima of local ( $5^{\text{th}}$  order) polynomial least-squares fits.

### 5.1.5 Overlap in Data Sets from SSRL and LCLS

After the  $S(q)$  algorithm had been established (described in the previous section), the experimental data in Paper II were compared to confirm overlap between data sets. Due to the increasing background and decreasing scattering intensity of water at high  $q$ ,  $q_1$  could be determined to much higher accuracy than  $q_2$ . Therefore,  $q_1$  was used to align the independent data sets measured at LCLS in Feb 2011 to the data set measured at SSRL in Jan 2012 with an absolute temperature calibration. The  $34\text{ }\mu\text{m}$  diameter droplets produced by the RJ had 10.01 mm away from the nozzle an almost identical  $q_1$  to the static sample of  $\text{H}_2\text{O}$  measured at 258 K (Fig. 5.8a). Similarly, the  $12\text{ }\mu\text{m}$  diameter droplets produced by the GDVN exhibited 12.35 mm away from the nozzle  $q_1$  very close (but at slightly higher  $q$ ) to the static sample of  $\text{H}_2\text{O}$  measured at 251 K (see Fig. 5.8b). This, together with the mutual overlap between the  $12\text{ }\mu\text{m}$  droplets and  $34\text{ }\mu\text{m}$  droplets at further distances away from the nozzles (see Fig 5.8c), enabled us to relate the data series measured at LCLS in Feb 2011 to known temperatures. Consequently, the uncertainties of the droplet parameters presented in Section 5.3.7 were narrowed down through the Knudsen theory of evaporation, yielding droplet diameters of 12, 34, and  $37\text{ }\mu\text{m}$  with corresponding droplet velocities of 10.35, 13.15, and 11.03 m/s, respectively.

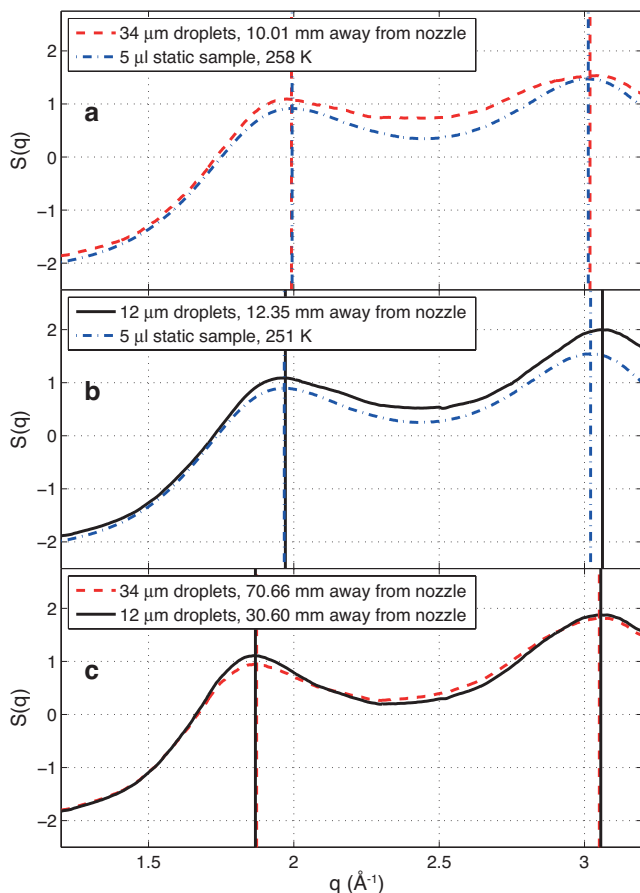


**Figure 5.8:** The interatomic total scattering structure factor  $S(q)$  compared for (a)  $34\ \mu\text{m}$  water droplets  $10.01\ \text{mm}$  away from the nozzle (red dashed curve) measured at LCLS in Feb 2011 and a  $5\ \mu\text{l}$  static sample of  $\text{H}_2\text{O}$  held at  $258\ \text{K}$  (blue dash-dotted curve) measured at SSRL in Jan 2012; (b)  $12\ \mu\text{m}$  water droplets  $12.35\ \text{mm}$  away from the nozzle (black solid curve) measured at LCLS in Feb 2011 and a  $5\ \mu\text{l}$  static sample of  $\text{H}_2\text{O}$  held at  $251\ \text{K}$  (blue dash-dotted curve) measured at SSRL in Jan 2012; (c)  $34\ \mu\text{m}$  water droplets  $70.66\ \text{mm}$  away from the nozzle (red dashed curve) and  $12\ \mu\text{m}$  water droplets  $30.60\ \text{mm}$  away from the nozzle (black solid curve) both measured at LCLS in Feb 2011.  $S(q)$  were obtained from  $I_{\text{norm}}(q)$  using Eq. (5.11), as explained in Section 5.1.4. The vertical lines indicate  $q_1$  and  $q_2$  derived from the maxima of local (5<sup>th</sup> order) polynomial least-squares fits. The near-identical  $q_1$  suggest that the temperature of the data series measured independently at LCLS in Feb 2011 can be related to each other as well as the data series measured at SSRL in Jan 2012 with an absolute temperature calibration of  $\pm 1\ \text{K}$ .



The data series recorded in Jan 2013 using the GDVN had a separate  $q$ -calibration and different detector position compared to the data series recorded in Feb 2011. Furthermore, the weak average intensity of the water hits for the data series (due to attenuated x-ray pulses forced by intense ice scattering) suffered from non-linear effects in the detector as discussed in the end of Section 5.1.4. We therefore concluded  $q_1$  and  $q_2$  were too uncertain to force experimental overlap with previously measured data. Instead the increased probability of ice nucleation events observed independently during the two experiments at long distances from the nozzle orifices could be utilized to confirm that the temperature calibration for the  $9\text{ }\mu\text{m}$  droplets was consistent with the synchrotron measurements at absolute temperature. The similar droplet diameters for the two GDVNs (and thus similar cooling rates, see Section 5.3.7) indicate that the quick increase in ice hit fraction, which is expected to be highly temperature dependent [148], must occur at almost identical temperatures well within our uncertainties. Thus, it is possible to relate the droplet temperature of the last data point for the  $9\text{ }\mu\text{m}$  droplets to the 3<sup>rd</sup> last data point for the  $12\text{ }\mu\text{m}$  droplets where the ice hit fraction is 18 % (see Fig. 5.9).

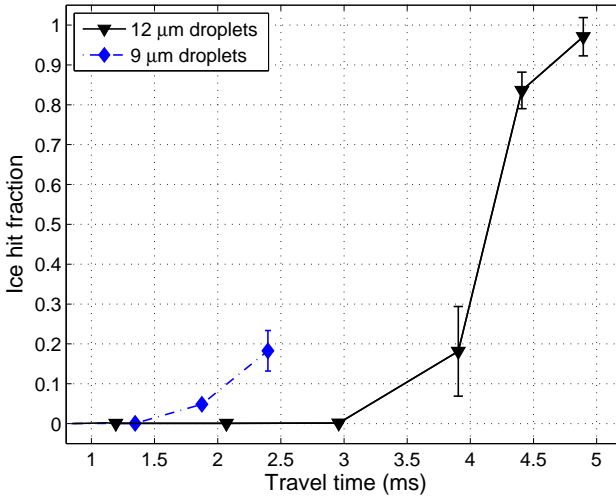


**Figure 5.9:** Plot of ice hit fraction with respect to the total number of hits including both water and ice hits as a function of travel time in vacuum for 12  $\mu\text{m}$  (black solid curve with triangles) and 9  $\mu\text{m}$  (blue dash-dotted curve with diamonds) diameter water droplets. The droplets were produced by the GDVNs in Feb 2011 and Jan 2013 with corresponding velocities of 10.35 m/s and 19.23 m/s, respectively. The error bars are obtained by the standard deviation of each individual recording at the same travel time with a total hitting number varying from 100 to 15000. Although the data series were recorded independently, the similarity in droplet size makes it possible to relate the droplet temperature of the last data point for the 9  $\mu\text{m}$  droplets to the 3<sup>rd</sup> last data point for the 12  $\mu\text{m}$  droplets where the ice hit fraction is  $\sim 18\%$ .

## 5.2 Analysis of X-ray Spectra

I will not review the corrections to the x-ray spectra, as they were less complex than those applied to the scattering patterns described in Section 5.1 and they are well documented in Papers IV and VI<sup>‡</sup>. Instead, I will discuss Lambert-Beer's law for XAS and use it to derive the fluence dependence model applied to data in Paper V.

### 5.2.1 Lambert-Beer's Law

Historically, Lambert's law stated that the absorbance  $A$  (or optical density) is proportional to the thickness of the sample  $z$  [m], and Beer's law that  $A$  is proportional to the concentration of the sample. Putting the two together, the intensity change  $dI_z$  upon passing through an infinitesimally thin layer  $dz$  must be proportional to the number density of particles  $n$  [molecules/m<sup>3</sup>], each particle's absorption cross-section<sup>§</sup>  $\sigma_a$  [m<sup>2</sup>/molecule], and the number of photons  $I_z$  passing through the layer, so that

$$dI_z = -\sigma_a n I_z dz. \quad (5.13)$$

Eq. (5.13) is separable and we can solve it directly by integrating  $I_z$  from  $I_0$  to  $I_l$  and  $z$  from 0 to  $l$ , and we obtain

$$\ln(I_l) - \ln(I_0) = -\sigma_a n l. \quad (5.14)$$

Raising Eq. (5.14) to the exponent yields the familiar expression for Lambert-Beer's law

$$I_l = I_0 e^{-\sigma_a n l}, \quad (5.15)$$

where  $\sigma_a n l = A$  fulfills the statements by Lambert and Beer. Eq. (5.15) gives a simple relation between the transmitted intensity through a sample of thickness  $l$  and the absorption cross-section, which we employed in the STXM measurements at ALS to extract  $\sigma_a$  in Paper IV.

When measuring XAS for very thin samples with thicknesses much less than the attenuation length of the x-rays, we may approximate Eq. (5.15) by a linear relationship. Assuming the intensity of secondary electrons is directly

<sup>‡</sup>Additionally, my contribution was less extensive, since the code base through which all x-ray emission data at LCLS was processed had already been implemented in the standard analysis framework by my colleague Martin Beye at Helmholtz-Zentrum Berlin. Therefore, I merely had to execute the scripts.

<sup>§</sup>Technically, one may want to consider the intensity change of the incident photons to be proportional to the total scattering cross-section, but as the absorption cross-section dominates by orders of magnitude over all other contributions (see Fig. 2.1) for water at the excitation energies considered, we can safely replace  $\sigma_{tot}$  by  $\sigma_a$ .

proportional to the attenuated intensity  $I_0 - I_l$ , we Taylor expand around  $A = 0$  for the SEY measurements, so that

$$I_{SEY} = I_0 (1 - e^{-A}) = I_0 (1 - 1 + A + \dots) \approx I_0 A = I_0 \sigma_a n l. \quad (5.16)$$

Eq. (5.16) was used to extract  $\sigma_a$  for the ice film on BaF<sub>2</sub> recorded at SSRL in Paper IV.

### 5.2.2 Fluence Dependence Model for X-ray Emission Decay Channel

XES performed at synchrotrons is usually expected to be in the linear regime where the intensity of the radiative decay is proportional to fluence (or equivalently, number of incident photons per molecule). This assumes that the majority of the molecules are in the ground state at any given point in time an x-ray photon is absorbed and then emitted after the decay of the core-hole, which is no longer the case at FELs where a large fraction of molecules can be valence-excited (or ionized) through Auger decay within the x-ray pulse length. Below, I briefly review the rate equation used in Paper V to describe the fluence dependence of the x-ray emission yield based upon reabsorption of x-ray emission following Lambert-Beer's law.

We describe the number of observed photons  $N_o$  that travel toward the spectrometer as a function of the  $y$  coordinate, *i.e.* the direction which the spectrometer is mounted toward (see Fig. 5.10), with  $y = 0$  at the farthest point of the excitation volume away from the spectrometer. The boundary condition is then given by  $N_o(y = 0) = 0$ . Ignoring any dependence in other directions, we may formulate the ordinary differential equation

$$\frac{dN_o}{dy} = \frac{dN_e}{dy} - \frac{dN_a}{dy}, \quad (5.17)$$

where  $N_e$  is the number of spontaneously emitted photons and  $N_a$  is the number of absorbed photons. Assuming a constant core-excitation density across the illuminated volume,  $N_e$  must increase linearly with  $y$ , so we may write the differential emission as

$$\frac{dN_e}{dy}(E, N_i) = A N_i \frac{1}{Y} \frac{\sigma_e(E)}{\Sigma}, \quad (5.18)$$

where  $N_i$  is the number of incident photons,  $\sigma_e(E)$  is the emission cross-section as a function of emission energy  $E$ ,  $\Sigma = \int \sigma_e(E) dE$  is the total emission cross-section of the whole x-ray emission region,  $Y$  is the maximum emission depth (see Fig. 5.10), and  $A$  is a scaling parameter that depends on the quality of alignment, the fraction of emission yield compared to other

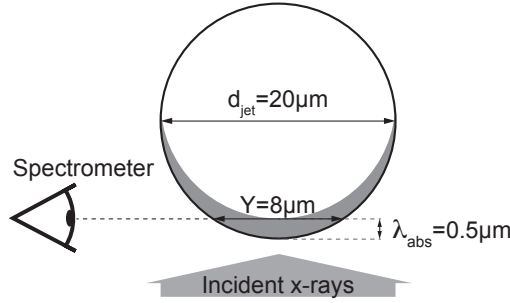


**Figure 5.10:** Schematic image of the experimental geometry as seen in the horizontal plane perpendicular to the flowing water jet with a diameter of  $20 \mu\text{m}$ . The spectrometer is mounted at  $90^\circ$  with respect to the incident x-rays and is aligned so that its field of view is overlapping with the illuminated volume of the water jet. The x-rays with a nominal photon energy of  $550 \text{ eV}$  penetrate about  $0.5 \mu\text{m}$  into the water jet before they are absorbed, resulting in a maximum emission depth  $Y = 8 \mu\text{m}$ . The drawing is not to scale.

decay channels (Auger decay), and the angular acceptance and detection efficiency of the detector.

In agreement with Lambert-Beer's law (described in Section 5.2.1), the absorbed number of photons in an infinitesimally thin layer  $dy$  should be proportional to the number of observed photons and the absorption cross-section. With the proportionality constant being the valence-hole density  $\rho_{vh}(N_i)$ , we obtain

$$\frac{dN_a}{dy}(y, E, N_i) = N_o(y) \sigma_a(E) \rho_{vh}(N_i), \quad (5.19)$$

where  $\sigma_a(E)$  is the absorption cross-section as a function of excitation energy  $E$ . If we compare Eq. (2.71) for XAS and Eq. (2.72) for XES, we see that if  $\hbar\omega_k = \hbar\omega_{k'}$ , they are the inverse processes with identical transition probabilities so that  $\sigma_e(E) = \sigma_a(E) \equiv \sigma(E)$ . It is therefore identical to the corresponding emission cross-section and we approximate its energy dependence by the measured undistorted x-ray emission spectrum at very low fluence.

Thus, Eq. (5.17) is a first-order linear differential equation, which is conveniently solved using an integrating factor [223], yielding<sup>‡</sup>

$$N_o(y, E, N_i) = \frac{AN_i}{Y\rho_{vh}(N_i)\Sigma} \left(1 - e^{-\sigma(E)\rho_{vh}(N_i)y}\right). \quad (5.20)$$

<sup>‡</sup>After integration of the exact differential, we must apply the boundary condition to determine the solution to the homogeneous equation that is relevant to the physical problem.

To fit Eq. (5.20) to our x-ray emission data, we must describe how the valence-hole density depends on the incident number of photons. Suppose that in our simple model (see Fig. 5.11) the DOS of the VB and conduction band (CB) are of box-like shapes with width  $E_{BW}$  (taken from width in x-ray emission spectrum), height  $6/E_{BW}$  (so that the integral is 6 electrons for the VB, excluding the  $2a_1$  level), and separation  $E_{HL}$ , corresponding to the band gap in water (estimated from the onset of x-ray absorption and the high-energy end of the resonant x-ray emission taken from Ref. [60]). If we also assume that the valence-hole density is maximized as a function of the total energy deposited per molecule  $E_{tot} = N_i E_i / N_{H_2O}$ , we can write

$$\rho_{vh} = -\frac{3E_{HL}}{E_{BW}} \pm \sqrt{\frac{9E_{HL}^2}{E_{BW}^2} + \frac{6N_i E_i}{N_{H_2O} E_{BW}}}. \quad (5.21)$$

We evaluate Eq. (5.20) at  $y = Y$  (assuming all losses of photons beyond the water jet are taken care of  $A$ ) and see that for very low fluences,  $1 - e^{-\sigma(E)\rho_{vh}(N_i)Y} \approx \sigma(E)\rho_{vh}(N_i)Y$  so that  $N_o \approx AN_i\sigma(E)$ , and for very high fluences,  $e^{-\sigma(E)\rho_{vh}(N_i)Y} \approx 0$  so that  $N_o \propto \sqrt{N_i}$ . However, if the valence-hole density would saturate at  $\rho_{vh}(N_i) = \rho_{vh}^{sat}$ , which it will do eventually as there is a limited number of valence electrons,  $N_o$  would again depend linearly on  $N_i$  with a slope differing from that in the low-fluence regime by  $(1 - e^{-\sigma(E)\rho_{vh}^{sat}Y}) / \rho_{vh}^{sat}$ . We will use these results to explain the fluence dependence of the x-ray emission yield in Paper V, presented in Section 6.3.1.

The parameters used in Paper V are summarized in Table 5.4; a more thorough description of the fluence dependence model is given in the supplementary information of Paper V.

**Table 5.4:** Parameters used by the reabsorption model described in Eq. (5.20). All are properties of the geometry or sample and can be estimated theoretically, except for  $A$  that is fitted to experimental data.

Parameter	Value
$E_{HL}$	7.3 eV
$E_{BW}$	7.0 eV
$Y$	8 $\mu\text{m}$
$\Sigma$	$1 \times 10^{-22} \text{ m}^2$
$\rho_{H_2O}$	$3.3 \times 10^{28} \text{ m}^{-3}$
$A$	$(0.41 \pm 0.01) \times 10^{-10}$

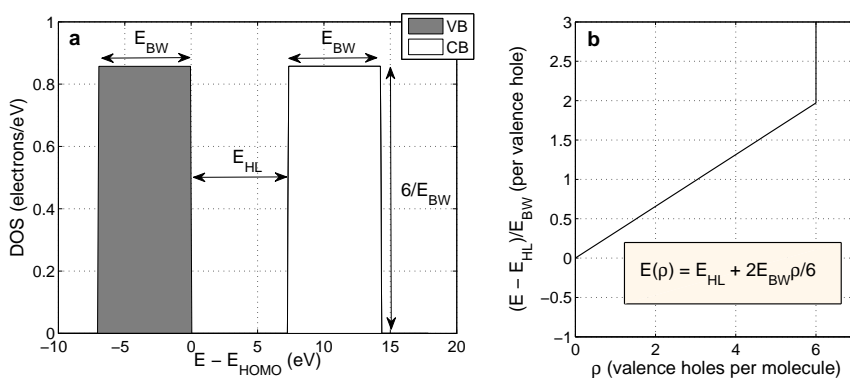


**Figure 5.11:** (a) Simplified model of the DOS in water, assuming the occupied VB and the unoccupied CB are of box-like shapes with width  $E_{\text{BW}} = 7.0$  eV and height  $6/E_{\text{BW}}$ , so that the integral is 6 electrons for the VB, excluding the  $2a_1$  level. The VB and CB are separated by  $E_{\text{HL}} = 7.3$  eV, corresponding to the band gap in water. The energy is plotted with respect to the energy of the highest occupied molecular orbital (HOMO). (b) The minimum energy  $E(\rho)$  necessary to form a valence hole as a function of valence-hole density  $\rho$ . If  $E(\rho)$  is integrated up to a given valence-hole density  $\rho_{\text{vh}}$ , the total energy necessary to form a valence-hole density  $\rho_{\text{vh}}$  is obtained.

### 5.3 Temperature Calibration

A critical part of the data analysis was to calibrate the temperature of the deeply supercooled droplets presented in Papers II-III and VI. In this section, the underlying theory is reviewed along with the numerical implementation, which is briefly compared to results from MD simulations, after which the experimental parameters and conditions are studied in detail. The 12  $\mu\text{m}$  diameter droplets produced by the GDVN and the 34  $\mu\text{m}$  diameter droplets produced by the RJ will be used as examples. Finally, the temperature calibration is derived based on experimental overlap between data sets in Papers II-III, which was established in Section 5.1.5.

#### 5.3.1 Knudsen Theory of Evaporation

The evaporation rate of a substance is commonly calculated using the Knudsen theory of evaporation [224–226], which is based on kinetic theory of gases [227]. It can be used to derive the cooling rate at the droplet surface [228]

$$\frac{dT_s}{dt} = -\gamma J_{e,max}(T) A_s(t) \frac{\Delta H_{vap}(T)}{N_A C_P(T) M_s(T)}, \quad (5.22)$$

where  $t$  is the travel time in the vacuum [s],  $T$  is the temperature [K],  $\Delta H_{vap}$  is the molar enthalpy of vaporization [J/mol],  $N_A$  is Avogadro's number [molecules/mol],  $C_P$  is the isobaric specific heat capacity [J/K,kg],  $A_s$  is the surface area of the droplet [ $\text{m}^2$ ],  $M_s$  is the mass of the interfacial evaporation layer of the droplet [kg],  $J_{e,max} = (P_e - P_v) / \sqrt{2\pi m k_B T_s}$  is the theoretical maximum rate of evaporation under equilibrium conditions [molecules/s,  $\text{m}^2$ ] [227] with the (corrected) equilibrium vapor pressure  $P_e$  [Pa], water vapor partial pressure  $P_v$  [Pa], Boltzmann's constant  $k_B$  [J/K], molecular mass  $m$  [kg/mol], and surface temperature  $T_s$  [K]. The evaporation coefficient  $\gamma$  in Eq. (5.22) is the ratio between the experimental rate of evaporation and the theoretical maximum  $J_{e,max}$ , and its value has varied largely in past measurements between 0.5 and 1 for water evaporation [229]. This variation appears to mainly arise from varying accuracies in surface temperature and vapor pressure measurements due to different experimental conditions and apparatuses (see the review by Eames *et al.* [229] and references therein). Theoretically,  $\gamma$  is related to the probability for a liquid molecule to evaporate at the interface given that it is thermodynamically favorable, or reversely, it is related to the sticking coefficient for a gas molecule to condense as it impinges on a liquid surface. To cite Varilly & Chandler [230]: “Any deviation of  $\gamma$  from 1 signals impediment to evaporation (or condensation) beyond the mere cohesive strength of the liquid.” The fact that it appears to be experimentally possible to achieve  $\gamma = 1$  suggests that there is little or no kinetic barrier



for water molecules to pass the liquid-vapor interface. This is supported by recent MD simulations obtaining  $\gamma$  close to unity [230]. Hence, we set  $\gamma = 1$  in the present work. Our results from MD simulations are briefly presented in Section 5.3.2.

For each time step in the numerical calculation, the thermal transport within the droplet is calculated. The water droplet was modeled as a sphere subdivided into  $n_{max}$  spherical shells with a uniform shell thickness of  $\Delta r$ , indexed  $n$ , where  $n$  decreases with decreasing shell radii,  $r_n$ . The heat flow  $dQ/dt$  through the surface between the  $n^{\text{th}}$  and  $(n+1)^{\text{th}}$  shells inside a water droplet is calculated using Fourier's law of thermal conduction

$$\frac{dQ}{dt} = -4\pi r_n^2 \kappa \frac{T_{n+1} - T_n}{\Delta r}, \quad (5.23)$$

where  $\kappa$  is the thermal conductivity of water,  $r_n$  is the radius of the surface between the  $n^{\text{th}}$  and  $(n+1)^{\text{th}}$  shells, and  $T_{n+1} - T_n$  is the temperature difference between the  $n^{\text{th}}$  and the  $(n+1)^{\text{th}}$  shells. An energy balance is set up for each spherical shell and the temperature change  $\Delta T_n$  of a unit step in time for the  $n^{\text{th}}$  shell is then calculated by

$$\Delta T_n = \frac{\Delta Q_n}{C_p M_n}, \quad (5.24)$$

where  $\Delta Q_n$  is the net heat flow in/out of the  $n^{\text{th}}$  shell during a unit step in time and  $M_n$  is the mass of the  $n^{\text{th}}$  shell.

The pressure inside tiny droplets is increased due to the large curvature of the droplet surface and the surface tension, discussed in Chapter 4. The equilibrium vapor pressure is increased due to this effect and is corrected for in the numerical simulations using the Kelvin equation

$$P_e(T) = P_{e_0}(T) e^{2 \frac{\Gamma V_m}{r_{n_{max}} R T}}, \quad (5.25)$$

where  $P_{e_0}(T)$  is the equilibrium vapor pressure for a flat interface,  $\Gamma$  is the surface tension,  $V_m$  is the molar volume,  $r_{n_{max}}$  is the radius of the droplet,  $R$  is the general gas constant, and  $T$  is the temperature. The exponential factor for droplets of  $r_{n_{max}} = 3 \text{ nm}$  as in a typical MD simulation evaluates to 1.44, while for experimental droplet dimensions of  $r_{n_{max}} = 5 \mu\text{m}$  it is 1.0003 at  $T = 298 \text{ K}$ . The correction thus plays a role if we want to compare theory and simulation results, while it is negligible for experimental dimensions.

Additionally, the effect of mass loss was taken into account, which is described by integrating the total evaporation rate

$$\frac{dN}{dt} = \gamma J_{e,max} A_s(t) = \gamma J_{e,max} 4\pi r_{n_{max}}(t)^2, \quad (5.26)$$

where  $dN/dt$  is the rate at which molecules escape from the droplet surface through evaporation. Eq. (5.26) was integrated over time, providing the total number of evaporated molecules and thus the total mass loss up to the given time step. The radius  $r_{n_{max}}$  of the droplet and the shell thickness  $\Delta r$  were adapted in every time step.

The numerical code to perform the evaporative cooling calculations was written in C++, which is necessary to enable calculations with short enough time steps (usually  $\Delta t = 1 \times 10^{-10}$  s) to be feasible on a regular laptop. The short time steps are required for the numerical simulations to converge when nearly all quantities in Eq. (5.22) are temperature (and hence also time) dependent. Of course, this depends on the cooling rate of the material studied. The numerical code is planned to be published as open source in a forthcoming publication [231].

### 5.3.2 Molecular Dynamics Simulations of Evaporative Cooling

To verify the Knudsen theory of evaporation, MD simulations of water droplets with radii of 2-4 nm were performed using the TIP4P/2005 force field. In short, it was found that the mass-averaged temperature obtained from the Knudsen theory of evaporation was comparable to the time-dependent droplet temperature in the simulation to within 2-4 K (see Fig. 5.12), given that the correct thermodynamic parameters were supplied to the model. The Knudsen theory of evaporation used  $\gamma = 1$ , which is in agreement with a recent transition path sampling study by Varilly & Chandler [230] that found, using the SPC/E force field, that there was no additional barrier to evaporation beyond the cohesive strength of the liquid. Further details on the MD simulations are found in the supplementary information of Paper II and are planned to be published in a forthcoming publication [231].

### 5.3.3 Thermodynamic Parameters and Their Effect on Temperature Estimates

Based on the MD simulation results described above we find that, with sufficient knowledge about the substances' temperature dependent properties, there is no need for the evaporation coefficient  $\gamma$  frequently used in the literature on evaporation [225, 228, 229]. From experiments, the evaporation coefficient of water has been suggested to be unity under all conditions of pressure and temperature [229]. More recently, there has been an estimation using Raman thermometry [228] giving  $\gamma = 0.6$ , but the same authors have shown that this method is not valid for water [232]. Below I discuss, for

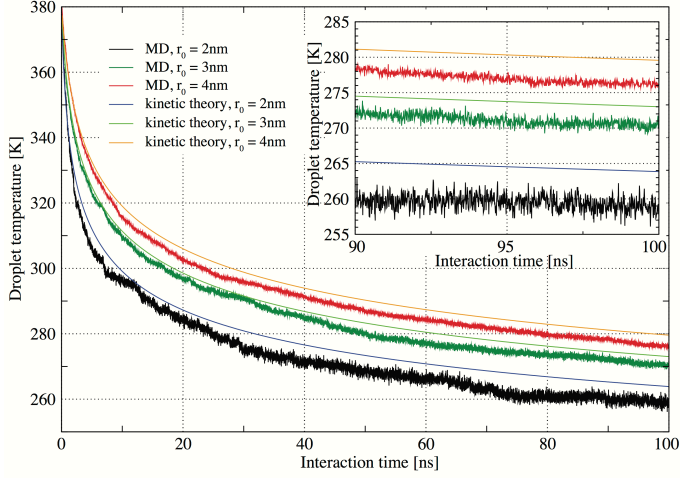


**Figure 5.12:** The temperature evolution in MD simulations of three different droplet sizes ( $r_0 = 2, 3$ , and  $4$  nm) compared to the corresponding results from the Knudsen theory of evaporative cooling. The numerical calculation accounts for evaporation, heat conduction, mass loss and the modification of vapor pressure due to surface tension. Furthermore, the surface area is corrected for the instantaneous surface area fitted to the data obtained from simulations. A value of  $\gamma = 1$  is used in the Knudsen theory of evaporation. The inset shows a blow-up of the region 90-100 ns and a finer temperature scale to facilitate comparison. The simulations are planned to be published in a forthcoming publication [231].

completeness, how an evaporation coefficient would affect the temperature calibration.

The effect of the uncertainty in the evaporation coefficient  $\gamma$  on the droplet temperature calculation using the Knudsen theory of evaporation described in Eq. (5.22)-(5.24) is illustrated in Fig. 5.13, where the mass-averaged temperature  $T$  of the droplet is calculated as a function of droplet travel time  $t$  in the vacuum after leaving the dispenser orifice for three selected values of  $\gamma$  (0.6, 0.8 and 1). It is clear that in the timescale of our measurements (within  $t \sim 6$  ms), the maximum uncertainty in the calculated temperature across this range of  $\gamma$  is  $\pm 3$  K, which is significant. However, as  $\gamma$  is a constant coefficient in Eq. (5.22), a variation in  $\gamma$  is identical to a similar variation around the measured speed  $v$  on which the travel time depends linearly, *i.e.* reducing  $\gamma$  and  $v$  by half yields an unchanged  $T_s$  as a function of sample-nozzle distance. It is only in Eq. (5.23)-(5.24) that there is a difference between a variation in  $\gamma$  and  $v$ , since Eq. (5.23)-(5.24) are independent of  $\gamma$  whereas the travel time still depends linearly on  $v$ . As the conduction rate in general is higher than the evaporation rate for the droplet sizes and travel times studied (*i.e.* the

temperature gradients in the droplets shown in Fig. 5.17 are small for travel times  $t > 1$  ms), this effect is small and a variation in  $\gamma$  is therefore nearly identical to an uncertainty in the speed. Thus, from hereon we will only study  $\gamma = 1$  and when limiting the uncertainty in the speed through overlap of experimental data we effectively limit  $\gamma$  simultaneously to be close to unity.

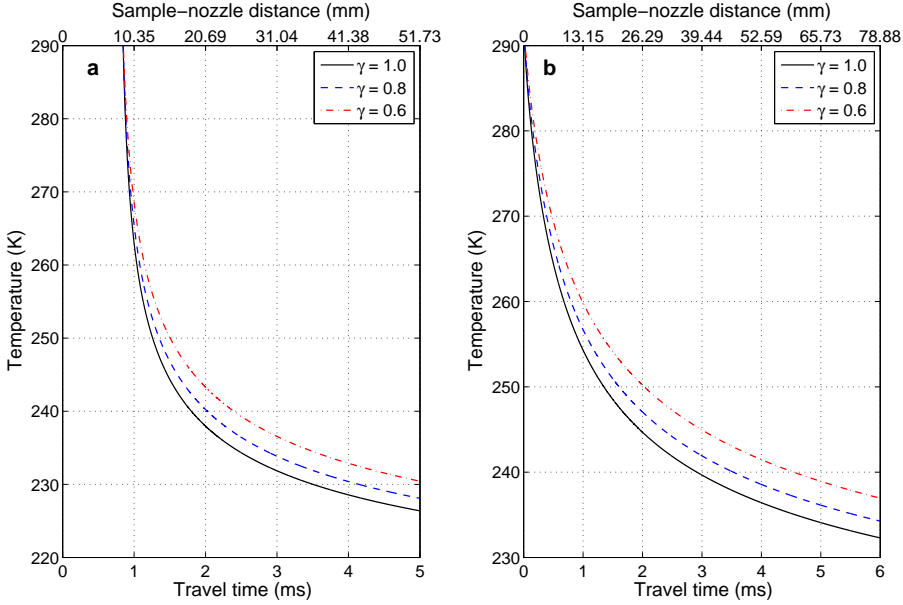


**Figure 5.13:** Effect of the evaporation coefficient  $\gamma$  on the mass-averaged droplet temperatures for (a) the  $12\mu\text{m}$  droplets produced by the GDVN and (b) the  $34\mu\text{m}$  droplets produced by the RJ. The calculations were performed with exponential  $C_p$ ,  $\Delta H_{vap}$  from Somayajulu *et al.* [233],  $P_e$  from Murphy & Koop [92],  $\rho$  from ice  $I_h$  interpolation, polynomial (4<sup>th</sup> order) least-squares fit of  $\kappa$ , linear least-squares fit of  $\Gamma$ ,  $D_{drop} = 12.38$  and  $33.60\mu\text{m}$ ,  $v = 10.35$  and  $13.15\text{m/s}$ , delay distance  $x = 8.7$  and  $0\text{mm}$ ,  $T_0 = 293\text{K}$ ,  $P_v \approx P_0 = 0.1333$  and  $0.2666\text{Pa}$ ,  $n_{max} = 100$  shells, and a time step  $\Delta t = 1 \times 10^{-10}\text{s}$ .

We carefully reviewed the temperature-dependence of various thermodynamic properties of water used in Eq. (5.22)-(5.25), including  $\Delta H_{vap}$ ,  $C_p$ ,  $P_e$ ,  $\kappa$ ,  $\Gamma$ , and  $\rho$ . At temperatures for deeply supercooled water the values of most of these parameters are based upon theoretical studies or experimental extrapolations from higher temperatures. For example, the enthalpy of vaporization  $\Delta H_{vap}$  is calculated using the empirical equation (2) from Somayajulu *et al.* [233] based upon available data from the water triple-point to the liquid-gas critical point.  $C_p$  is least-squares fitted to an exponential due

to the sharp increase observed in experimental data down to 236 K [2]. The equilibrium vapor pressure  $P_e$  is described by the empirical equation (10) from Murphy & Koop [92], which is derived from data on the molar heat capacity of supercooled water. The thermal conductivity  $\kappa$ , the water density  $\rho$ , and the surface tension  $\Gamma$  are obtained from polynomial extrapolations based on experimental data available down to 250 K [90], 243 K [234] and 246 K [235], respectively. Below is a detailed study of each property and its various functional expressions that are consistent with experimental data.

Errors in the calculated droplet temperatures caused by inherent uncertainties in the extrapolations of the parameters were found to be largest for  $C_p$ , which appears to diverge in the supercooled region [2]. In order to test the effect of  $C_p$  on calculated temperatures, several empirical temperature dependencies of  $C_p$  were investigated in Fig. 5.14a. They are: a polynomial (green broken line) and an exponential (black solid line) extrapolation of accessible experimental data down to 236 K [2], which exhibit a divergent behavior toward low temperatures; a power-law fit (red dash-dotted line) to accessible experimental data down to 236 K [2] that strictly diverges at 226 K; and a bell-shaped  $C_p$  (blue dashed line) peaked at 226 K by applying the empirical equation (13) from Huang & Bartell [14]. On the basis of the theoretical scenarios presented in Chapter 3, we can argue what functional form would be preferred. For the LLCP model,  $C_p$  is expected to exhibit a maximum between 220–240 K at 1 atm [236], which would favor the bell-shaped  $C_p$ . A maximum is also expected by the singularity-free scenario [142], whereas the stability-limit conjecture predicts that  $C_p$  would strictly diverge [1], which would favor the power-law fit of  $C_p$ . The bell-shaped  $C_p$  fits the experiment poorly below 240 K, whereas the power-law fit overestimates the increase in  $C_p$  as the strict divergence would render it impossible to quench water to its glassy state through “no-man’s land”, which has been accomplished by projecting micron-sized water jets into a liquid cryomedium [237] or hyperquenching aerosols of micron-sized water droplets on a solid cryoplate *in vacuo* [121, 122]. The mass-averaged droplet temperature for the 12  $\mu\text{m}$  diameter droplets is shown in Fig. 5.14b, where we see that there is only a noteworthy difference between the various fits of  $C_p$  below 230 K, equivalent to travel times beyond  $\sim 3$  ms. Hence, there are only a few data points affected by the choice of  $C_p$  in the current study. As the polynomial and exponential fit of  $C_p$  could be consistent with all theoretical scenarios in the temperature regime studied ( $> 220$  K), we chose the exponential fit of  $C_p$  as a suitable representation of the isobaric heat capacity of water in the deeply supercooled regime. The bell-shaped  $C_p$  and power-law fit of  $C_p$  were used to calculate the maximum and minimum temperatures consistent with experimental data in Section 5.3.7, and these are thus considered as outer boundaries for plausible temperature dependence.

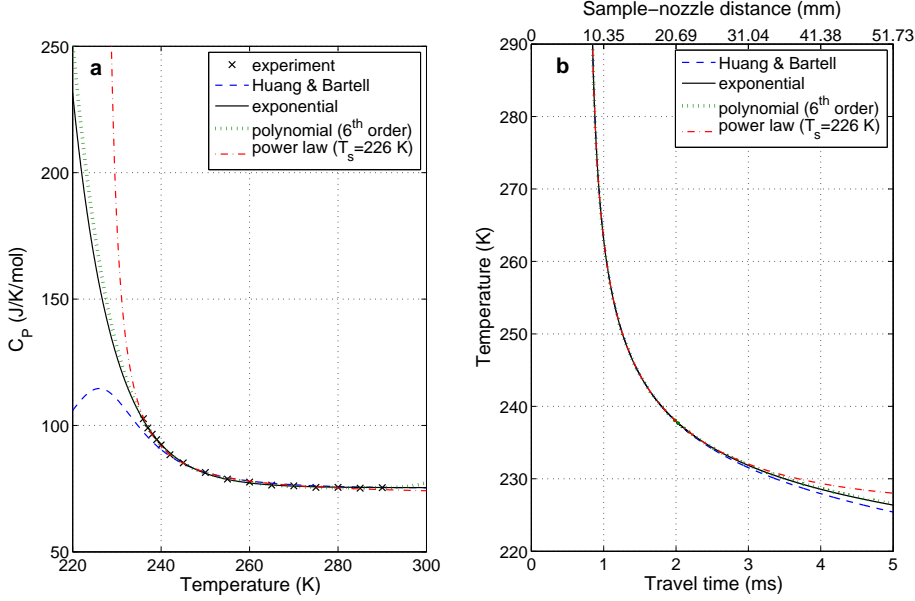


**Figure 5.14:** Extrapolations of the temperature dependence of the specific heat capacity at constant pressure  $C_p$  of water and its effect on the calculated droplet temperatures using the Knudsen theory of evaporation. (a) Comparison between four different fits of  $C_p$  to experimental data (black crosses) taken from Angell *et al.* [2] extrapolated to the deeply supercooled region, where the blue dashed line is the empirical equation (13) from Huang & Bartell [14]. (b) Calculated mass-averaged droplet temperatures for the 12  $\mu$ m diameter droplets using the various extrapolations of  $C_p$  (colors and line types are the same in both panels). All calculations were performed with exponential  $\Delta H_{vap}$  from Somayajulu *et al.* [233],  $P_e$  from Murphy & Koop [92],  $\rho$  from ice  $I_h$  interpolation, polynomial (4<sup>th</sup> order) least-squares fit of  $\kappa$ , linear least-squares fit of  $\Gamma$ ,  $\gamma = 1.0$ ,  $D_{drop} = 12.38 \mu\text{m}$ ,  $v = 10.35 \text{ m/s}$ , delay distance  $x = 8.7 \text{ mm}$ ,  $T_0 = 293 \text{ K}$ ,  $P_v \approx P_0 = 0.1333 \text{ Pa}$ ,  $n_{max} = 100$  shells, and a time step  $\Delta t = 1 \times 10^{-10} \text{ s}$ .

Similarly to  $C_p$ ,  $\Delta H_{vap}$ ,  $P_e$ ,  $\kappa$ ,  $\Gamma$ , and  $\rho$  were tested for various empirical expressions and functional forms. In all these cases, the various fits consistent with experimental data yielded temperature uncertainties of less than 1 K and the choice of the exact expression had little effect on the temperature calibration using the Knudsen theory of evaporation. Nevertheless, the functional forms resulting in the warmest and coldest droplet temperatures were used to calculate the maximum and minimum temperatures consistent with experimental data, respectively, in Section 5.3.7.

### 5.3.4 Delay of Evaporative Cooling from Focusing Gas

Another important correction has been performed to account for the delay of evaporative cooling of water droplets caused by the focusing gas that exists around the jet/droplets produced by the GDVN. Usually, this shielding gas consists of He, which is inert and has low cross-section for absorption and scattering above 200 eV, and therefore He was used in Papers V-VI when performing XES. For the x-ray scattering data in Papers II-III, however, the shielding gas was chosen to be  $N_2$ , as the CSPAD may discharge at too high He pressure and thus damage the detector. All relations in the following discussion, unless stated otherwise, are derived from Pauly's book [238]. In the GDVN, pressurized dry gas flows through the outer glass capillary and necks down the central water jet close to the nozzle exit [212]. The gas pressure  $P_g$  and orifice diameter  $d$  differed for the various experiments, with  $P_g = 490$  psi  $N_2$  and  $d \sim 60 \mu\text{m}$  in Feb 2011,  $P_g = 330$  psi He and  $d \sim 40 \mu\text{m}$  in Oct 2012, and  $P_g = 200$  psi  $N_2$  and  $d \sim 30 \mu\text{m}$  in Jan 2013. The shielding gas exits the nozzle with sonic speed since the gas/vacuum pressure ratio satisfies the condition of

$$\frac{P_g}{P_0} \geq \left( \frac{k+1}{2} \right)^{k(k-1)}, \quad (5.27)$$

where the isentropic expansion factor  $k = C_p/C_V$  is to first order 7/5 for a diatomic gas (in rotational equilibrium), such as  $N_2$ , and 5/3 for He (with no rotations) [90,238]. If we neglect the central water jet, gas molecules/atoms close to the nozzle move along divergent hyperbolic trajectories, with thermal motion causing intermolecular collisions. As the gas diverges and its density drops away from the nozzle, free molecular/atomic flow is achieved at a boundary known as the "quitting" surface, which is typically a few mm away from the nozzle. This boundary can be calculated through the reduced "quitting" surface  $\xi = x/d$  (distance from the nozzle  $x$  and the nozzle exit dimension  $d$ ), which for a hard-sphere model is [238]

$$\xi = \left( \frac{4}{\sqrt{\pi}} C_2(k) \pi a^2 n_g d \right)^{1/k}, \quad (5.28)$$

where  $C_2(k)$  is the coefficient of the two-body collision rate integral for axisymmetric expansion, which is  $C_2(k) = 0.0655$  for  $k = 7/5$  and  $C_2(k) = 0.0465$  for  $k = 5/3$ ,  $a$  is the hard-sphere radius (*i.e.* the van der Waals radius), which is  $a = 2.25 \text{ \AA}$  for an  $\text{N}_2$  molecule and  $a = 1.4 \text{ \AA}$  for a He atom, and  $n_g$  is the number density of gas molecules/atoms in the nozzle. The number density can be calculated from the ideal gas law, which for gas pressures of 490, 330, and 200 psi at 293 K becomes  $n_g \approx 8.4 \times 10^{-4}$ ,  $5.7 \times 10^{-4}$ , and  $3.4 \times 10^{-4} \text{ \AA}^{-3}$  for the experiments performed in Feb 2011, Oct 2012, and Jan 2013, respectively. Thus, the quitting surface is estimated to be 156, 20, and 50 which corresponds to about 9.4, 0.8, and 1.5 mm downstream from the nozzle. As a first approximation, we assume that evaporative cooling for the GDVN initiates around the “quitting” surface where the intermolecular collision rate is negligible and the resulting droplet temperatures are compared in Fig. 5.15 for three selected delay distances from the nozzle ( $x = 8.7, 9.4$  and  $10.1 \text{ mm}$ ) for the  $12 \mu\text{m}$  diameter droplets. Although the droplet temperature close to the nozzle is very sensitive to the exact location of the “quitting” surface, for travel times longer than  $\sim 3 \text{ ms}$  in vacuum, where the boundary of the “no-man’s land” is crossed, the temperature of the droplets is less influenced by the expanded  $\text{N}_2$  gas and the resulting variation in temperature is less than 1 K. In what follows, we chose  $x = 8.7 \text{ mm}$ , which was determined to achieve optimal overlap between the  $12 \mu\text{m}$  droplets and  $34 \mu\text{m}$  droplets and SSRL measurements at absolute temperature as discussed in Section 5.3.7.

### 5.3.5 Mass Loss from Evaporation

We also investigated the effect of mass loss due to evaporation by monitoring  $A_s(t)$  and integrating Eq. (5.26). As illustrated in Fig. 5.16, the mass of water droplets decreases by 10-12 % up to  $t = 6 \text{ ms}$ . Since the diameter decreases as the third root of the mass (assuming constant density over the temperature range), the mass loss enhances the evaporative cooling slightly. This effect is similar to the increased cooling that a slightly smaller droplet exhibits compared to a slightly larger one. In reality, the density decreases with decreasing temperature, which makes the decrease in droplet diameter even smaller, and thus the temperature difference compared to an approximation with constant radius is expected to be much smaller than 1 K.

### 5.3.6 Temperature Gradients in Droplets Due to Evaporative Cooling

Since evaporative cooling only occurs at the vacuum-droplet interface, it is expected that there will be a temperature gradient throughout the droplet with the surface being colder than the center. This effect is demonstrated by plot-



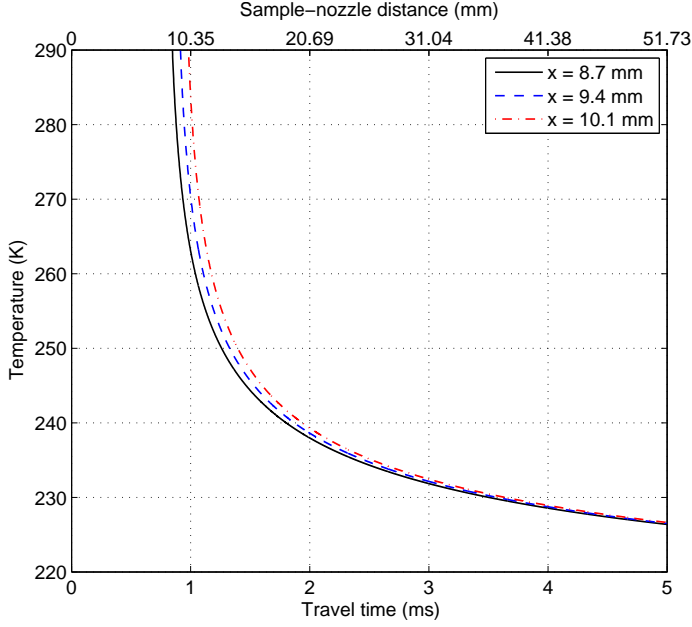


**Figure 5.15:** Effect of evaporation delay distance  $x$  from the orifice of the GDVN due to the presence of  $N_2$  gas around the water droplets as estimated by the quitting surface Eq. (5.28). The calculations of the mass-averaged temperature were performed with exponential  $C_p$ ,  $\Delta H_{vap}$  from Somayajulu *et al.* [233],  $P_e$  from Murphy & Koop [92],  $\rho$  from ice  $I_h$  interpolation, polynomial (4<sup>th</sup> order) least-squares fit of  $\kappa$ , linear least-squares fit of  $\Gamma$ ,  $\gamma = 1.0$ ,  $D_{drop} = 12.38 \mu\text{m}$ ,  $v = 10.35 \text{ m/s}$ ,  $T_0 = 293 \text{ K}$ ,  $P_v \approx P_0 = 0.1333 \text{ Pa}$ ,  $n_{max} = 100$  shells, and a time step  $\Delta t = 1 \times 10^{-10} \text{ s}$ .

ting the difference between the local temperature for each spherical shell in Eq. (5.23)-(5.24) and the mass-averaged temperature of the entire droplet. As shown in Fig. 5.17, the temperature gradient of the  $34 \mu\text{m}$  diameter droplets is larger than that of the  $12 \mu\text{m}$  diameter droplets at a specific travel time, due to the larger size. For droplet travel durations between 2-6 ms, where most of our measurements have been performed, the temperature gradient is reduced quickly with the travel time through the vacuum and eventually becomes negligible for both the RJ and the GDVN. This is due to the fact that  $P_e(T)$  – and thus the cooling rate – drops by several orders of magnitude during the cooling process, which is not the case for the conduction rate.

If we further consider the possible jitter in the droplet position with respect to the incident x-ray beam, it results in an average volume probed in the droplet of  $\sim 10\%$  for the  $12 \mu\text{m}$  diameter droplets with a  $\sim 10 \mu\text{m}^2$ , and

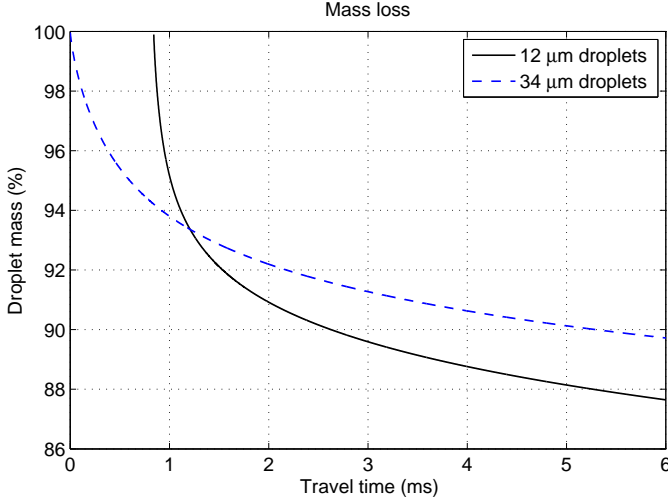


**Figure 5.16:** Mass loss of water droplets for both the RJ and the GDVN due to evaporative cooling. The calculations were performed with exponential  $C_p$ ,  $\Delta H_{vap}$  from Somayajulu *et al.* [233],  $P_e$  from Murphy & Koop [92],  $\rho$  from ice  $I_h$  interpolation, polynomial (4<sup>th</sup> order) least-squares fit of  $\kappa$ , linear least-squares fit of  $\Gamma$ ,  $\gamma = 1.0$ ,  $D_{drop} = 12.38$  and  $33.60 \mu\text{m}$ ,  $v = 10.35$  and  $13.15 \text{ m/s}$ , delay distance  $x = 8.7$  and  $0 \text{ mm}$ ,  $T_0 = 293 \text{ K}$ ,  $P_v \approx P_0 = 0.1333$  and  $0.2666 \text{ Pa}$ ,  $n_{max} = 100$  shells, and a time step  $\Delta t = 1 \times 10^{-10} \text{ s}$ .

$\sim 2\%$  for the  $9 \mu\text{m}$  diameter droplets with a  $\sim 1 \mu\text{m}^2$ . The average volume probed is even smaller for the  $34\text{--}37 \mu\text{m}$  diameter droplets, which results in a distribution of droplet temperatures probed at a given distance (corresponding to a given travel time). Although we chose to use the mass-averaged temperature in the calculation to represent the droplet temperature associated with averaged single-shot scattering images at a certain sample distance, which we can safely do at long travel times, we used the temperature gradients within the droplets to calculate the error bars for the mass-average temperature presented in Tables 5.5–5.8.

### 5.3.7 Experimental Temperature Calibration

As already indicated in Section 5.1.5, the experimental overlap between SSRL and LCLS data yields additional constraints on the droplet parameters. In particular, they have to be chosen so that the  $34 \mu\text{m}$  diameter droplets produced by the RJ at  $10.01 \text{ mm}$  away from the nozzle have a temperature of  $258 \pm 1 \text{ K}$ , the  $12 \mu\text{m}$  diameter droplets produced by the GDVN at  $12.35 \text{ mm}$  away from the nozzle have a temperature of  $252 \pm 1 \text{ K}$ , and the  $12 \mu\text{m}$

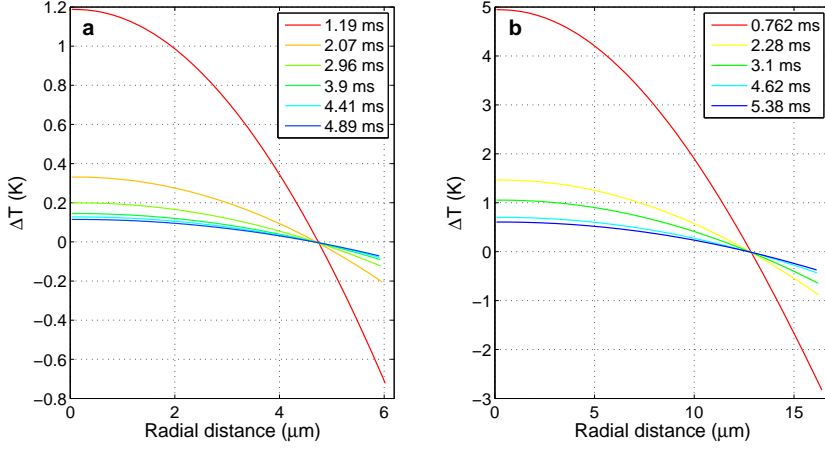


**Figure 5.17:** Temperature variation  $\Delta T$  with respect to the mass-averaged temperature is plotted along the radius of (a) the  $12\text{ }\mu\text{m}$  diameter droplets and (b) the  $34\text{ }\mu\text{m}$  diameter droplets at selected travel times corresponding to the sample-nozzle distances measured. The calculations were performed with exponential  $C_P$ ,  $\Delta H_{\text{vap}}$  from Somayajulu *et al.* [233],  $P_e$  from Murphy & Koop [92],  $\rho$  from ice  $I_h$  interpolation, polynomial (4<sup>th</sup> order) least-squares fit of  $\kappa$ , linear least-squares fit of  $\Gamma$ ,  $\gamma = 1.0$ ,  $D_{\text{drop}} = 12.38$  and  $33.60\text{ }\mu\text{m}$ ,  $v = 10.35$  and  $13.15\text{ m/s}$ , delay distance  $x = 8.7$  and  $0\text{ mm}$ ,  $T_0 = 293\text{ K}$ ,  $P_v \approx P_0 = 0.1333$  and  $0.2666\text{ Pa}$ ,  $n_{\text{max}} = 100$  shells, and a time step  $\Delta t = 1 \times 10^{-10}\text{ s}$ . Note that the range of the x-axes corresponds to the initial radii of the droplets ( $6.19$  and  $16.8\text{ }\mu\text{m}$ , respectively).

droplets and  $34\text{ }\mu\text{m}$  droplets at sample-nozzle distances of  $30.60$  and  $70.66\text{ mm}$ , respectively, have the same temperature given the uncertainty of the temperature evolution. To establish such an overlap, the minimum and maximum temperature consistent with the experimental overlap of the GDVN at  $252 \pm 1\text{ K}$  (see Fig. 5.18a) and the RJ at  $258 \pm 1\text{ K}$  (see Fig. 5.18b) were calculated by choosing the least and most conservative empirical expressions of each thermodynamic quantity, respectively, as well as varying droplet size and speed around their corrected values (see Tables 4.4 and 4.1). It was found that, when holding the temperature fixed at a calibration point, larger radii and lower speeds gave, in general, temperature evolutions toward lower temperatures after the calibration point than smaller radii and higher speeds. Compared to the reported values for the droplet diameter and speed in Table 4.1, the  $34\text{ }\mu\text{m}$  droplets obtained the cooling curve reaching lowest temperatures when  $D_{\text{drop}} = 36.52\text{ }\mu\text{m}$  (100%) and  $v = 10.75\text{ m/s}$  (79%), and exhibited the cooling curve at highest temperatures when  $D_{\text{drop}} = 33.60\text{ }\mu\text{m}$

(92%)  $\mu\text{m}$  and  $v = 13.66\text{ m/s}$  (100.2%) (the values in parenthesis are given in percent of their previously determined values in Table 4.1). This resulted in a temperature of  $233 \pm 1\text{ K}$  for the  $34\text{ }\mu\text{m}$  droplets at 70.66 mm away from the nozzle, thus restricting the temperature uncertainty for the  $12\text{ }\mu\text{m}$  diameter droplets at 30.60 mm. For these droplets, plausible droplet radii and speeds were varied from their initial, fitted value to achieve experimental overlap with SSRL data. The cooling curve reaching lowest temperatures was obtained for the  $12\text{ }\mu\text{m}$  droplets when  $D_{drop} = 13.88$ ,  $v = 9.65\text{ m/s}$ , and delay distance  $x = 8.2\text{ mm}$ . Similarly, the cooling curve at highest temperatures was obtained for the  $12\text{ }\mu\text{m}$  droplets when  $D_{drop} = 12.15\text{ }\mu\text{m}$ ,  $v = 13.13\text{ m/s}$ , and delay distance  $x = 8.0\text{ mm}$ .

Once the boundaries for the temperature evolution from the calibration points had been established, the reported values of the droplet parameters from Tables 4.4 and 4.1 were perturbed as little as possible (within their uncertainties) from their best guesses to achieve experimental overlap. Since the  $12\text{ }\mu\text{m}$  diameter droplets originally had a colder temperature calibration, the speed had to be increased slightly to  $10.35\text{ m/s}$  (104%) from its initial value. At the same time, the delay distance is very sensitive to the temperature of the calibration point and it had to be decreased to  $8.7\text{ mm}$  (93%) to ensure that the temperature is  $\sim 252\text{ K}$  at  $12.35\text{ mm}$  away from the nozzle. For the  $9\text{ }\mu\text{m}$  diameter droplets, experimental overlap was established through the onset of ice crystallization at  $46.09\text{ mm}$  away from the nozzle, which should coincide with the onset of ice crystallization at  $40.40\text{ mm}$  away from the nozzle for the  $12\text{ }\mu\text{m}$  droplets, corresponding to a droplet temperature of  $229^{+2}_{-1}\text{ K}$ . The reported droplet parameters in Table 4.4 for the  $9\text{ }\mu\text{m}$  droplets result in a droplet temperature of  $228\text{ K}$ , which is within the uncertainty of the calibration temperature so no corrections had to be made. The  $34\text{ }\mu\text{m}$  droplets originally had a warmer temperature calibration than consistent with experimental overlap, so the droplet diameter and speed were decreased to  $33.60\text{ }\mu\text{m}$  (92%) and  $13.15\text{ m/s}$  (96%) from their initial values. The  $37\text{ }\mu\text{m}$  droplets also produced by the RJ had been characterized and measured under near-identical conditions to the  $34\text{ }\mu\text{m}$  droplets, and thus we believe the systematic shifts in droplet diameter and speed should be similar for the two data sets. Therefore, the droplet diameter and speed for the  $37\text{ }\mu\text{m}$  droplets were similarly decreased to  $36.52\text{ }\mu\text{m}$  (91%) and  $11.03\text{ m/s}$  (95%) from their initial values.

Mindful of the effects discussed above, the calculated temperatures of water droplets using Eq.(5.22)-(5.24) are shown in Fig. 5.18. The markers represent measurements on the RJ in Fig. 5.18a and the GDVNs in Fig. 5.18b. The total error bars  $\epsilon_{T,tot}$  of droplet temperatures are made up of two contributions: the relative error in temperature  $\epsilon_{T,rel}$  due to uncertainty in the temperature evolution from the calibration points at experimental overlap;

the error in temperature  $\epsilon_{T,grad}$  caused by the temperature gradients within the droplets due to the interplay between evaporation rate at the surface and conduction rate inside the droplet. Assuming these two sources of error are mutually independent, their net error becomes  $\epsilon_{T,tot} = \sqrt{\epsilon_{T,rel}^2 + \epsilon_{T,grad}^2}$ . These results are also summarized in Tables 5.5-5.8. For the  $37\text{ }\mu\text{m}$  diameter droplets using the RJ in Feb 2011 and the  $5\text{ }\mu\text{m}$  diameter droplets using the GDVN in Oct 2012, no experimental overlap occurred with SSRL measurements at absolute temperatures and the uncertainties for these data points are therefore estimated by their temperature gradients and the least/most conservative extrapolations of thermodynamic quantities into “no-man’s land” (see Section 5.3.3). Additionally, the maximum/minimum travel time due to the large focus of  $75 \times 520\text{ }\mu\text{m}^2$  used for the  $5\text{ }\mu\text{m}$  diameter droplets was taken into account. For the  $9\text{ }\mu\text{m}$  diameter droplets using the GDVN in Jan 2013,  $\epsilon_{T,rel}$  was taken to be equal to that for the  $12\text{ }\mu\text{m}$  droplets at 40.40 mm away from the nozzle where the onset of ice nucleation coincides.

**Table 5.5:** Calculated mass-averaged temperatures of  $34\text{-}37\text{ }\mu\text{m}$  diameter water droplets generated by the RJ in Feb 2011 according to the Knudsen theory of evaporation described by Eq. (5.22)-(5.24). The error bars were calculated from the temperature evolution from the calibration points at experimental overlap and the temperature gradients within the droplets. For the  $37\text{ }\mu\text{m}$  diameter droplets, no experimental overlap occurred and the error bars were estimated only by the temperature gradients.

Sample-nozzle distance (mm)	Travel time (ms)	Temperature (K)
10.01	0.76	$258^{+5}_{-3}$
15.80	1.43	$251^{+3}_{-2}$
20.79	1.88	$247^{+2}_{-1}$
30.01	2.28	$243 \pm 2$
30.74	2.78	$242 \pm 1$
40.76	3.40	$239 \pm 1$
60.71	4.62	$235^{+1}_{-2}$
70.66	5.38	$233 \pm 1$

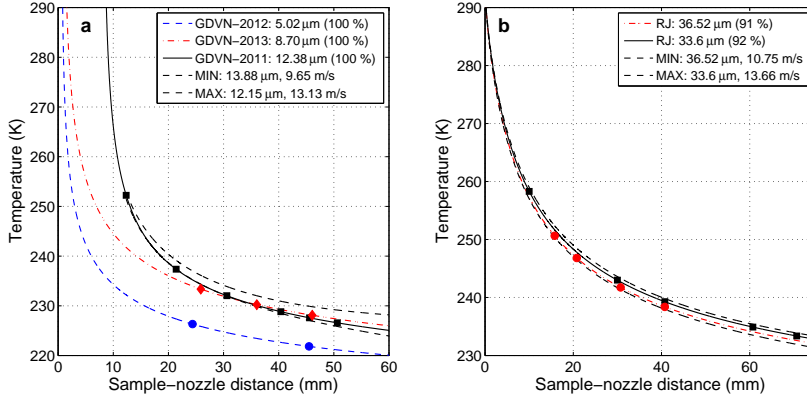


**Figure 5.18:** Calculated mass-averaged temperatures of water droplets generated by (a) the GDVNs and (b) the RJ according to the Knudsen theory of evaporation described by Eq. (5.22)–(5.24). All the temperature calibrations were (unless stated) calculated with exponential  $C_p$ ,  $\Delta H_{vap}$  from Somayajulu *et al.* [233],  $P_e$  from Murphy & Koop [92],  $\rho$  from ice  $I_h$  interpolation, polynomial (4<sup>th</sup> order) least-squares fit of  $\kappa$ , linear least-squares fit of  $\Gamma$ ,  $\gamma = 1.0$ ,  $T_0 = 293$  K,  $n_{max} = 100$  shells, and a time step  $\Delta t = 1 \times 10^{-10}$  s. The droplet parameters from Tables 4.1 and 4.4 were optimized within their uncertainties to achieve overlap between experimental data sets as established in Section 5.1.5 (the values in parenthesis are given in percent of the previously determined values); the resulting droplet parameters for the 5  $\mu\text{m}$  droplets (blue dashed line with circles), 9  $\mu\text{m}$  droplets (red dash-dotted line with diamonds), and 12  $\mu\text{m}$  droplets (black solid line with squares) in (a) produced by GDVNs were respectively  $D_{drop} = 5.02$  (100%), 8.70 (100%), and 12.38 (100%)  $\mu\text{m}$ ,  $v = 14.03$  (100%), 19.23 (100%), and 10.35 (104%) m/s, delay distance  $x = 0.8$  (100%), 1.5 (100%), and 8.7 (93%) mm, and  $P_v \approx P_0 = 0.231$  (100%), 0.05995 (100%), and 0.1333 (100%) Pa; the resulting droplet parameters for the 34  $\mu\text{m}$  droplets (black solid line with squares) and 37  $\mu\text{m}$  droplets (red dash-dotted line with circles) in (b) produced by the RJs were respectively  $D_{drop} = 33.60$  (92%) and 36.52 (91%)  $\mu\text{m}$ ,  $v = 13.15$  (96%) and 11.03 (95%) m/s, and  $P_v \approx P_0 = 0.2666$  (100%) and 0.3999 (100%) Pa. The minimum/maximum cooling curves (black dashed lines) for the 12  $\mu\text{m}$  droplets in (a) and 34  $\mu\text{m}$  droplets in (b) were calculated with  $C_p$  from Huang & Bartell [14]/power-law fit of  $C_p$ ,  $\Delta H_{vap}$  from Murphy & Koop [92]/ $\Delta H_{vap}$  from Somayajulu *et al.* [233] (swapped for the 34  $\mu\text{m}$  droplets),  $P_e$  from Hyland & Wexler [239]/ $P_e$  from Murphy & Koop [92],  $\rho$  from Hare *et al.* [240]/ $\rho$  from TIP4P/2005 force field re-scaled to fit experimental data at  $\rho_{max}$  of 277 K, polynomial (4<sup>th</sup> order) least-squares fit of  $\kappa/\kappa$  from Ramires *et al.* [241], and delay distance  $x = 8.2$  (87%) and 8.0 (85%) mm (only for the 12  $\mu\text{m}$  droplets). The adjusted droplet diameters and velocities to achieve experimental overlap are given in the legends.

**Table 5.6:** Calculated mass-averaged temperatures of  $12\mu\text{m}$  diameter water droplets generated by the GDVN in Feb 2011 according to the Knudsen theory of evaporation described by Eq. (5.22)-(5.24). The error bars were calculated from the temperature evolution from the calibration points at experimental overlap and the temperature gradients within the droplets.

Sample-nozzle distance (mm)	Travel time (ms)	Temperature (K)
12.35	1.19	$252^{+2}_{-1}$
21.41	2.07	$237^{+2}_{-0.2}$
30.60	2.96	$232^{+2}_{-0.1}$
40.40	3.91	$229^{+2}_{-1}$
45.60	4.41	$228^{+2}_{-1}$
50.62	4.89	$227^{+2}_{-1}$

**Table 5.7:** Calculated mass-averaged temperatures of  $5\mu\text{m}$  diameter water droplets generated by the GDVN in Oct 2012 according to the Knudsen theory of evaporation described by Eq. (5.22)-(5.24). The error bars were estimated from the temperature gradients within the droplets, the maximum/minimum travel time due to the large focus of  $75 \times 520\mu\text{m}^2$ , and the least/most conservative extrapolations of the thermodynamic properties, discussed in Section 5.3.3.

Sample-nozzle distance (mm)	Travel time (ms)	Temperature (K)
$0.6^{+0.3}_{-0.4}$	$0.04 \pm 0.02$	$291^{+2}_{-8}$
$24.4 \pm 0.4$	$1.74^{+0.02}_{-0.03}$	$226^{+2}_{-1}$
$45.5 \pm 0.3$	$3.24^{+0.03}_{-0.02}$	$222^{+5}_{-3}$

**Table 5.8:** Calculated mass-averaged temperatures of  $9\mu\text{m}$  diameter water droplets generated by the GDVN in Jan 2013 according to the Knudsen theory of evaporation described by Eq. (5.22)-(5.24). The error bars were calculated from the temperature gradients within the droplets and  $\varepsilon_{T,rel}$  taken to be equal to that for the  $12\mu\text{m}$  diameter droplets at 40.40 mm away from the nozzle, where the onset of ice nucleation coincides.

Sample-nozzle distance (mm)	Travel time (ms)	Temperature (K)
25.88	1.35	$233^{+2}_{-1}$
36.04	1.87	$230^{+2}_{-1}$
46.09	2.40	$228^{+2}_{-1}$

## 5.4 Ice Analysis

In addition to the analysis of single-shot scattering patterns (see Sections 5.1.2 and 5.1.3) and temperature calibration (see Section 5.3), a few remarks have to be made regarding the extracted ice nucleation rate, the classical nucleation theory (CNT) applied to it, and the concept of fragility applied to supercooled water in Paper III.

### 5.4.1 Extraction of the Ice Nucleation Rate

The ice nucleation rate<sup>||</sup> can be extracted from the ice hit fraction  $f_{ice}$  shown in Fig. 5.9. We assume that homogeneous nucleation is a stochastic process in the bulk liquid that follows Poisson statistics<sup>\*\*</sup> and that the Bragg diffraction collected in each ice hit comes from a single crystal, in which case

$$f_{ice}(t) = \begin{cases} 0, & t < t_0 \\ 1 - e^{-JV(t-t_0)}, & t \geq t_0 \end{cases} \quad (5.29)$$

where  $J$  is the homogeneous nucleation rate,  $V$  is the probed volume of the sample, and  $t_0$  is an arbitrary time after which the freezing is assumed to begin<sup>††</sup>. Although the average illuminated volume is  $\sim 10\%$  for the  $12\ \mu\text{m}$  droplets and  $\sim 2\%$  for the  $9\ \mu\text{m}$  droplets, we may approximate  $V$  by the whole droplet volume  $V_{drop}$ , since dendritic ice growth within the droplet is expected to occur at a velocity of  $\sim 0.3\ \text{m/s}$  [243], which would correspond to a timescale of  $20\text{--}40\ \mu\text{s}$ . Hence, ice that nucleates outside the illuminated volume grows to the probed part of the droplet much faster than the characteristic timescale for ice nucleation as seen in Fig. 5.9. If we also assume that  $J$  is constant between adjacent data points at  $t_n$  and  $t_{n+1}$ , which is reasonable since the cooling rate is fairly low when ice nucleation occurs (see Fig. 5.18 and Tables 5.6 and 5.8), we can eliminate the unknown  $t_0$  and solve for  $J$  at

---

<sup>||</sup>The ice nucleation rate is not a usual rate corresponding to events per time, but is in fact commonly defined as the number of nuclei per time and volume. The reason for this is to make the nucleation rate independent of sample volume, so the measured nucleation rate of bulk water at a given temperature is unique despite that the exponential decay constant in Eq. (5.29) is assumed to scale with volume. If, on the other hand, the exponential decay constant is assumed to scale with surface area, the corresponding surface nucleation rate should be stated as number of nuclei per time and area.

<sup>\*\*</sup>Thus, we neglect the effect of impurities within the drops, which could make the statistical spread of nucleation times many times larger than the average time itself [242].

<sup>††</sup>Ideally, one would like to perform a measurement where the temperature is fixed from some time  $t_0$  and then the nucleation is probed as a function of lag time  $t - t_0$  [242]. However, this is not possible in our experiments, because each droplet can only be probed once by the FEL and cooling is inherently convoluted with travel time.



time  $t_{n+1/2}$  and obtain

$$J(t_{n+1/2}) = -\frac{\ln\left(\frac{1-f_{ice}(t_{n+1})}{1-f_{ice}(t_n)}\right)}{V_{drop}(t_{n+1}-t_n)}. \quad (5.30)$$

The corresponding nucleation rate was expected to be representable of bulk water at  $T_{n+1/2} = (T_{n+1} + T_n)/2$  and Eq. (5.30) was therefore used in Paper III to estimate the nucleation rate as a function of temperature.

### 5.4.2 Classical Nucleation Theory and Fragility

According to CNT [244, 245], the homogeneous nucleation rate is governed by the rate at which nuclei of critical size (henceforth denoted critical nuclei) appear within a supercooled liquid, after which ice growth occurs spontaneously. Thus, the nucleation rate can be formulated as a thermally activated process [246, 247]

$$J = J_0 e^{-\frac{\Delta G^*}{k_B T}}, \quad (5.31)$$

where  $\Delta G^*$  is the Gibbs free energy barrier to form a critical nucleus,  $k_B$  is Boltzmann's constant,  $T$  is the temperature, and  $J_0$  is the highly temperature-dependent pre-exponential factor that is related to an Arrhenius-like expression [248]

$$J_0 = A e^{-\frac{\Delta g^\ddagger}{k_B T}}, \quad (5.32)$$

including a second pre-exponential factor  $A$  that is approximately independent of temperature and the kinetic activation energy barrier  $\Delta g^\ddagger$  for a water molecule to jump across the solid-liquid interface. As there are no direct measurements of  $\Delta g^\ddagger$ , it is usually inferred from either the viscosity  $\eta$  or the diffusivity  $D$  (*i.e.* self-diffusion constant) [248], which are related through the Stokes-Einstein equation [249]

$$D = \frac{k_B T}{6\pi\eta a}, \quad (5.33)$$

where  $a$  is the effective hydrodynamic radius of a water molecule that is roughly constant. When  $T \gg T_g$ , Eq. (5.33) holds for nearly all liquids and  $D\eta/T$  is approximately independent of  $T$ , resulting in that the same value is obtained when  $\Delta g^\ddagger$  is inferred from either  $D$  or  $\eta$ , namely about 4.6 kcal/mol for water near  $T_m$  [248]. However, below  $\sim 1.8T_g$ , Eq. (5.33) breaks down for water [250], and we must choose what measurable quantity best describes  $\Delta g^\ddagger$ . In Paper III, we chose to use the diffusivity  $D$ , because it can be microscopically related (*e.g.* in MD simulations) to the asymptotic slope of the mean-squared displacement of individual water molecules, whereas

the viscosity is difficult to accurately calculate in MD simulations and it has instead been estimated microscopically by the  $\alpha$  relaxation time  $\tau_\alpha$  of the liquid [250]. Hence, we write the pre-exponential factor in Eq. (5.31) as

$$J_0 = \frac{16D}{\nu_{H_2O,s}} \left( \frac{3}{4\pi} \right)^{1/3} \left( \frac{\sigma_{sl}}{k_B T} \right)^{1/2}, \quad (5.34)$$

where  $\sigma_{sl}$  is the solid-liquid interfacial free energy<sup>††</sup>,  $\nu_{H_2O,s}$  is the molecular volume of a water molecule in the solid, and  $D$  can be represented by

$$D = D_0 e^{-\frac{E_D}{k_B T}}, \quad (5.35)$$

where  $D_0$  is a constant and  $E_D = \Delta g^\ddagger$  is the activation energy for diffusion in the liquid. We assume that the temperature-dependence of  $D$  is entirely captured in the exponent. When cooling toward  $T_g$ , there exist two quite different scenarios. If  $E_D$  is approximately constant as the liquid is cooled, we call it a “strong” liquid, whereas if  $E_D$  is changing significantly with temperature, we call it a “fragile” liquid, in agreement with the definition for  $\eta$  by Angell [251–253]. Fragility, *i.e.* deviations from Arrhenius-like behavior for  $D$  or  $\eta$ , implies structural changes beyond those of thermal motion during the glass-forming process. We shall apply this concept to the temperature-dependence of the diffusivity when we present the results of Paper III (see Section 6.2.1).

We can quantify fragility by the Vogel-Fulcher-Tammann (VFT) equation in a modified form [252, 254], which has been empirically found to hold almost universally for glass formers close to  $T_g$ , and can be applied to  $D$  as [248]

$$D = D_0 e^{-\frac{FT_k}{T - T_k}}, \quad (5.36)$$

where  $D_0$  is a constant pre-factor and  $F$  is the fragility parameter that describes the deviation from Arrhenius-like behavior, for which  $T_k = 0$  K and  $F \rightarrow \infty$ . Thus, large  $F$  corresponds to a “strong” liquid and liquids with small  $F$  are called “fragile”. Furthermore, it shows that when  $F$  changes so does  $T_k$ , known as the Kauzmann temperature [115, 255] at which the difference in entropy between the liquid and the crystal disappears<sup>x</sup>. It has been interpreted as the thermodynamic transition temperature from a liquid phase to an ideal glassy state [255], or, in other words, the calorimetric ideal glass transition temperature when the cooling rate is infinitely slow, but this

<sup>††</sup>The solid-liquid interfacial free energy can also be regarded as the surface tension of the solid in the bulk liquid phase, and therefore has the same units as surface tension [N/m = J/m<sup>2</sup>].

<sup>x</sup>This would imply that the configurational entropy  $S = k_B \ln W = 0$ , where  $W$  is the number of possible configurations, assuming the vibrational entropy of the liquid is similar to that of the crystal [255].

has been criticized by Kauzmann [115] and Stillinger *et al.* [256], arguing that the extrapolation of metastability to such conditions simply is not valid. Nevertheless,  $T_g$  can be regarded as a kinetic manifestation of  $T_k$  [252, 254], and the two would only coincide when  $D_o = D_0$  or an ideal “fragile” liquid with  $F = 0$  is obtained [252]. To obtain  $\Delta g^\ddagger$  from VFT-fitted diffusivity, we must relate Eq. (5.36) to Eq. (5.35) as

$$\Delta g^\ddagger = E_D = k_B T \left[ \frac{FT_k}{T - T_k} - \ln \left( \frac{D_o}{D_0} \right) \right]. \quad (5.37)$$

Turning back to Eq. (5.31), we describe the thermodynamic energy barrier in the Boltzmann factor by [248]

$$\Delta G^* = \frac{16\pi\sigma_{sl}^3\nu_{H_2O,s}^2}{3(\Delta\mu_{sl})^2}, \quad (5.38)$$

where  $\Delta\mu_{sl}$  is the chemical potential difference between the solid and liquid phase evaluated at the pressure and temperature of the liquid phase, which may be partitioned into  $\Delta\mu_{sl} = \Delta\mu_{sl,P_0}(T) + \Delta\mu_{sl}(P)$ , where

$$\Delta\mu_{sl,P_0} = -k_B T \ln \left( \frac{P_{e,l}}{P_{e,s}} \right) \quad (5.39)$$

is the chemical potential calculated at a reference pressure  $P_0$  with equilibrium vapor pressure  $P_{e,l}$  and  $P_{e,s}$  of the liquid and solid, respectively. Assuming constant isothermal compressibility, the pressure-dependence can be approximated by [248]

$$\Delta\mu_{sl}(P) = (P_l - P_{e,s})\nu_{H_2O,s} - (P_l - P_{e,l})\frac{\nu_{H_2O,l}(P_l) + \nu_{H_2O,l}(P_{e,l})}{2}, \quad (5.40)$$

where  $\nu_{H_2O,s}$  and  $\nu_{H_2O,l}$  is the molecular volume of a water molecule in the solid and in the liquid, respectively.

In Paper III, we assume that the liquid nucleates into ice  $I_c$  that, as discussed in Section 3.4, is kinetically favored to ice  $I_h$ , especially upon deep supercooling.



# Chapter 6

## Summary of Results

In this chapter, the results presented in Papers I-VI will be summarized. An effort will be made to put the results in context and connect the studies. The interested reader is referred to the papers for further details.

### 6.1 X-ray Scattering of Liquid Water

In this section, I will summarize the results on temperature-dependent x-ray scattering of liquid water, presented in Papers I-II. It was shown that the principal maximum of  $S(q)$  splits up into a doublet upon cooling, and that the splitting  $\Delta q$  of the doublet is correlated to the increase in local structures with tetrahedral coordination in the liquid. This relationship was utilized to extract the height of the second hydration shell in  $g_{OO}(r)$  directly from  $\Delta q$  without Fourier inversion, enabling metastable liquid water to be studied down to a temperature of  $227^{+2}_{-1}$  K, which is below the upper boundary of “no-man’s land” at 232 K [8–10]. It was found that, upon deep supercooling, the liquid structure undergoes a continuous transformation toward a tetrahedrally-coordinated LDL, with local correlations at  $\sim 230$  K more similar to those of LDA ice than those of ambient water.

#### 6.1.1 Paper I – Medium-range Order in Water is a Fingerprint of Tetrahedral Structures

The scattered intensity  $I(q)$  of liquid water was measured up to  $\sim 16 \text{ \AA}^{-1}$  at 280 K, 298 K, and 339 K. The resulting intermolecular  $S(q)$  was obtained by applying Eq. (2.49) with the normalization constant taken from the average of Eq. (5.5) and Eq. (5.9). The result is presented in Fig. 6.1. As the temperature is decreased, the principal maximum in  $S(q)$  develops a distinct splitting

into a doublet. Looking closely, it is also seen that the higher oscillations are slightly more dampened when the liquid is heated. Although heating water and pressurizing it has many analogies, such an effect (*i.e.* damping of the higher oscillations) is not observed when applying pressure to water [182]. It was argued by Okhulkov *et al.* [182] that above  $8\text{--}9\text{ \AA}^{-1}$  only the correlations of the first coordination shell are present. Assuming a Gaussian distribution of the first coordination shell, the increased damping of the higher oscillations could then be interpreted as a broadening of the first coordination shell [182].

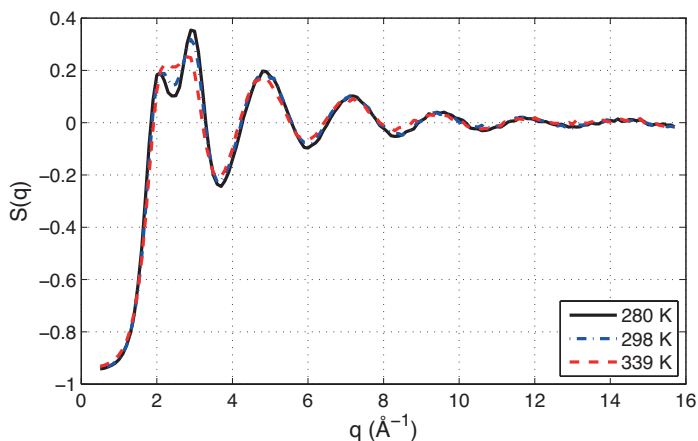


**Figure 6.1:** Comparison of  $S(q)$  of liquid water ( $\text{H}_2\text{O}$ ) measured at 280 K (black solid line), 298 K (blue dash-dotted line) and 339 K (red dashed line), respectively. The figure has been adapted from Paper I by permission of the PCCP Owner Societies.

The molecular PCF describes the average probability of finding a water molecule at distance  $r$  from another water molecule at the origin, where the orientation of water molecules is averaged over all angles. It was obtained using Eq. (5.10) and the result is shown in Fig. 6.2a for the three temperatures measured. The PCFs exhibit a well-defined peak corresponding to nearest-neighbor molecules at  $\sim 2.8\text{ \AA}$  and pronounced second and third hydration shells centered at  $\sim 4.5\text{ \AA}$  and  $\sim 6.8\text{ \AA}$ , respectively, confirming the results of previous work [3, 4, 37, 38, 159, 182, 183]. Comparing the three temperatures, it is evident that heating the liquid broadens the peaks and reduces the amplitude of the correlations corresponding to the hydration shells. In particular, the second peak centered at  $\sim 4.5\text{ \AA}$  is strongly reduced above 298 K. It satisfies the condition for tetrahedral coordination

$$r_2 = \sqrt{\frac{8}{3}} r_1, \quad (6.1)$$

where  $r_1 \approx 2.8 \text{ \AA}$  is the distance of the nearest-neighbor molecules and  $r_2$  is the distance of the second coordination shell. This suggests that the local structures with tetrahedral coordination are diminished as the liquid is heated.

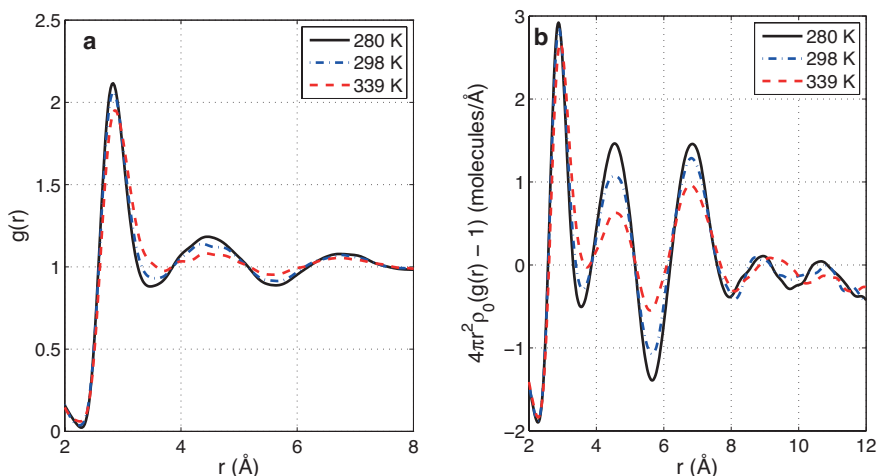


**Figure 6.2:** Comparison of (a)  $g(r)$  and (b) dRDFs (defined on the vertical axis) of liquid water ( $\text{H}_2\text{O}$ ) derived from measurements at 280 K (black solid line), 298 K (blue dash-dotted line) and 339 K (red dashed line), respectively. A damping factor of  $a = 0.009$  in (a) and  $a = 0.018$  in (b) was used in Eq. (5.10) to reduce the truncation oscillations, especially in the large- $r$  range where the true correlations are very weak. The peak height of the first peak is therefore suppressed, especially in (b). The figure has been adapted from Paper I by permission of the PCCP Owner Societies.

On close inspection of the first peak, it is observed to shift outwards with temperature from  $2.81 \text{ \AA}$  at 280 K, to  $2.82 \text{ \AA}$  at 298 K, and to  $2.84 \text{ \AA}$  at 339 K, which is attributable to the thermal expansion of the liquid. Additionally, the first peak becomes highly asymmetric upon heating the liquid with a growing correlation at  $\sim 3.4 \text{ \AA}$ , which has been assigned to interstitial molecules [159] that are weakly H-bonded to the molecule at the origin and thus are far from being tetrahedrally coordinated. A similar effect has also been observed when applying pressure to water [182]. Furthermore, we note that there is an isosbestic point at  $\sim 3.4 \text{ \AA}$  for the coordination function  $n(0, r)^*$  defined

\*In our experimental data, artificial correlations between molecules are present below  $2.2 \text{ \AA}$ , which have been ignored in the present analysis. Thus, we actually calculate  $n(2.2 \text{ \AA}, r)$  when we estimate the number of neighboring molecules present up to a distance  $r$ .

in Eq. (2.34), which corresponds to 4.8 neighboring molecules up to this distance.

The correlations at intermediate distances beyond the nearest-neighbor molecules can be magnified by plotting the difference in the radial distribution function (dRDF) from that of the average molecular density in Fig. 6.2b. The second and third coordination shells are now more clearly seen than in Fig. 6.2a. In addition, the high quality of the data also revealed weaker fourth and fifth hydration shells, resolving shell structure out to 12 Å similar to studies of supercooled water [4, 257]. This was the first time the fourth and fifth shells had been resolved for room temperature water. Interestingly, the temperature dependence of the hydration shells differed. The first and fourth peaks were less sensitive to a temperature change, whereas especially the second peak increased significantly upon cooling. Thus, the temperature-dependent structural changes are strongest around  $r = 4.5$  Å, corresponding to next-nearest neighbors in a tetrahedral coordination, which will be used in Paper II. The fourth peak, on the other hand, shifts to longer distances as the liquid is heated. This indicates that there are temperature-dependent structural changes in liquid water in addition to the effects of disorder induced by normal thermal motion, such as thermal expansion.

### 6.1.2 Paper II — Accelerated Abundance of Tetrahedral Structures in Deeply Supercooled Water

The x-ray scattering of supercooled water was measured up to  $\sim 3$  Å<sup>-1</sup> at temperatures down to 227<sup>+2</sup><sub>-1</sub> K, after which homogeneous ice nucleation was inevitable. The interatomic structure factor  $S(q)$ , obtained by applying Eq. (5.9) and Eq. (5.11), is shown in Fig. 6.3a for selected temperatures over the whole temperature range. At temperatures above the melting point, the principal maximum of  $S(q)$  shows similar characteristics to what was presented in Paper I above, but as the liquid is supercooled the observed doublet develops further into two well-separated peaks denoted  $S_1$  and  $S_2$ , as indicated by the dashed lines. The temperature dependence of the positions of  $S_1$  and  $S_2$ , denoted  $q_1$  and  $q_2$ , is displayed in Fig. 6.3b and compared to that of LDA ice determined experimentally using neutron diffraction (ND) [110]. It is evident that  $q_1$  and  $q_2$  move toward the characteristic values of LDA ice. It should be noted, however, that the liquid is not a glass, indicative of slow dynamics, since homogeneous ice nucleation occurs rapidly below 230 K, which will be discussed further in Paper III. Thus, the temperature-dependence of the peak split suggests a continuous structural transition toward an LDL in bulk water upon deep supercooling.



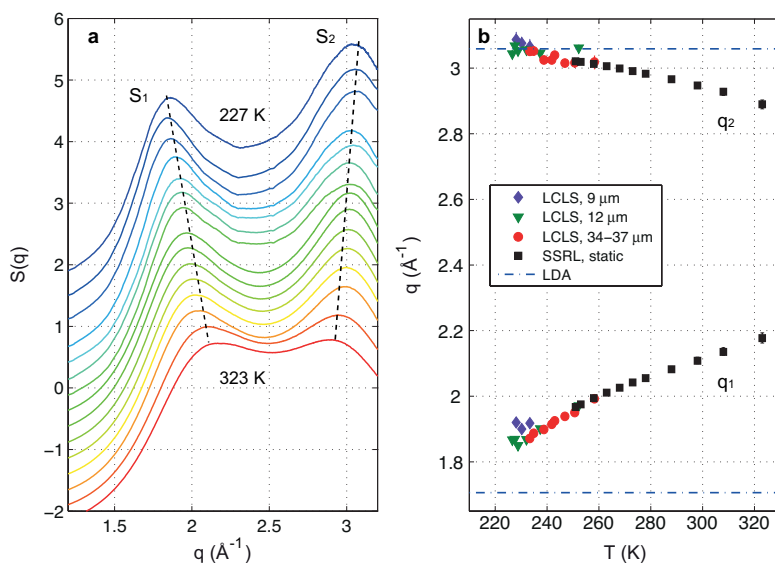


**Figure 6.3:** Temperature dependence of water ( $\text{H}_2\text{O}$ ) scattering peaks. (a) The scattering structure factor  $S(q)$  obtained from averaging over (depending upon the hitting rate at different temperatures) 100-15000 angularly integrated single-shot x-ray scattering patterns recorded on the CSPAD. Water temperature drops (SSRL: 323, 298, 273, 268, 263, 258, 253, 251 K; LCLS: 251, 247, 243, 239, 232, 229, 227 K) from bottom to top. The data reveals a split of the principal maximum of  $S(q)$  into two well-separated peaks,  $S_1$  and  $S_2$ , as indicated by the dashed lines. (b) Plot of temperature dependence of the positions of peaks  $S_1$  and  $S_2$  calculated from the maxima of local 5th order polynomial least-squares fits of  $S(q)$  in (a) with error bars estimated by shifting the derivatives of the polynomial fits by  $\pm 0.15 \text{ \AA}$  (LCLS) and  $\pm 0.050 \text{ \AA}$  (SSRL) as explained in Section 5.1.4. Green triangles are LCLS data from  $12 \mu\text{m}$  diameter droplets, red circles are the LCLS data from  $34\text{--}37 \mu\text{m}$  diameter droplets, and black squares are SSRL data from a static liquid sample with a thickness of  $1.5 \text{ mm}$  along the beam path. Purple diamonds are LCLS data from  $9 \mu\text{m}$  diameter droplets measured at a separate LCLS run with separate  $q$ -calibration (see Section 5.1.2 for details on CSPAD corrections). As the temperature decreases in “no-man’s land”, the positions of peaks  $S_1$  and  $S_2$  approach the characteristic values of LDA ice (solid blue lines) as determined using ND [110]. The figure is reprinted with permission from Paper II.

This picture was further reinforced by comparing the results to MD simulations using the TIP4P/2005 force-field [258]. It was found that the  $S(q)$  peak split, defined as  $\Delta q = q_2 - q_1$ , exhibited a strong correlation with the magnitude of the second peak in  $g_{OO}(r)$ , denoted  $g_2$  (see Fig. 6.4a). The non-linear relationship between the two quantities was established through MD simulations in a broad range of temperatures ( $T = 200$ -340 K). It was utilized to derive an experimental temperature-dependence of  $g_2$  in “no-man’s land”, shown in Fig. 6.4b. The same quantity was derived for the MD simulation at 1 bar and the agreement is satisfactory, although slightly underestimated at low temperatures. As demonstrated in Paper I, the magnitude of  $g_2$  is closely related to the tetrahedral coordination of the liquid structure. A sharp increase in  $g_2$  is seen upon supercooling water, indicating that the tetrahedrally coordinated species grows quickly and becomes the dominant structure of the liquid. The limiting value for  $g_2$  in the liquid state is assumed to be the value of LDA ice, discussed in Section 3.5 to correspond to the glassy equivalent of LDL water [144] with a tetrahedrally coordinated local structure. Upon deep supercooling,  $g_2$  at  $229^{+2}_{-1}$  K is closer to the value of LDA ice than water at room temperature, suggesting that the liquid structure is approaching that of pure LDL at these temperatures.

On close inspection, it is seen that  $g_2$  drops for the last two data points at  $228^{+2}_{-1}$  and  $227^{+2}_{-1}$  K for the 12  $\mu\text{m}$  diameter droplets and the last data point at  $228^{+2}_{-1}$  K for the 9  $\mu\text{m}$  diameter droplets, deviating from the general trend set by the MD simulation. The reason for this is thought to be an indirect effect of the onset of homogeneous ice nucleation observed at these temperatures (see Fig. 5.9); although all hits containing ice were removed during the data sorting process, the occurrence of Bragg peaks among the scattering patterns forced us to increase the attenuation to avoid damaging the detector. With increased attenuation, the weakened scattering peaks become more asymmetric (as discussed in Section 5.1.4), which is attributed to the non-linear response of the detector at low photon intensities. Hence, caution should be exercised when interpreting the value of  $g_2$  below the onset of homogeneous nucleation.

Despite the limited  $q$ -range of the data, impeding the PCF to be derived in a similar fashion as in Paper I, the PCF of the MD simulation at 220 K can be used as an estimate of the local structure of the liquid at  $\sim 228$  K with similar  $g_2$ . It is compared in Fig. 6.5 to the experimentally derived PCFs of liquid water at 295 K [5] and that of LDA ice [110]. There is a striking similarity between LDA ice and the MD simulation at 220 K, further strengthening the proposed structural similarity between the liquid upon deep supercooling and LDA ice. In contrast, we see that water at 295 K shows much less structural correlation with high probability of interstitial molecules between the broadened hydration shells.

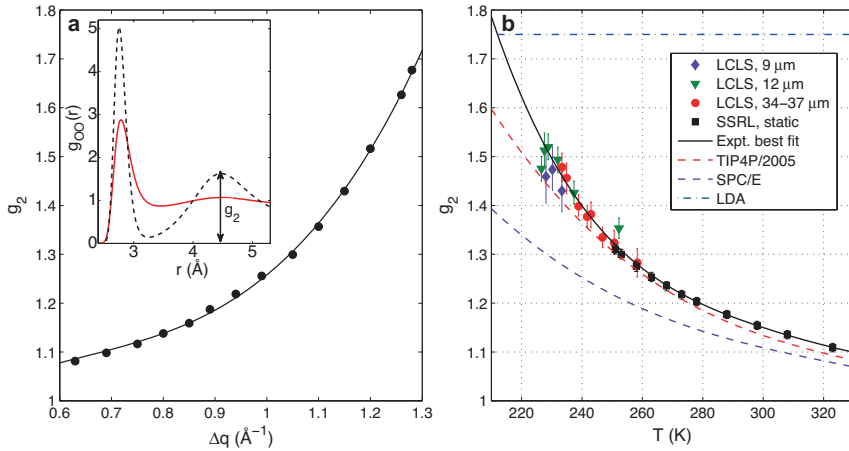


**Figure 6.4:** Temperature dependence of the tetrahedral coordination of liquid water ( $\text{H}_2\text{O}$ ). (a) Correlation of the magnitude of the second  $g_{oo}(r)$  peak, denoted as  $g_2$ , with the  $S(q)$  peak split, defined as  $\Delta q = q_2 - q_1$ , obtained from MD simulations using the TIP4P/2005 force field in a broad range for  $T = 200$ – $340$  K (circles). The variation of  $g_2$  with temperature is illustrated in the inset for  $g(r)$  at 320 K (red solid line) and 210 K (black dashed line)). The solid curve is the 3<sup>rd</sup> order polynomial least-squares fit of the MD results. (b) The experimental  $g_2$ , derived from measured  $\Delta q$  in various experimental setups (the labels are the same as in Fig. 6.3b) according to the best-fit MD data shown in (a), with error bars estimated by maximum/minimum  $\Delta q$  allowed by the uncertainty in the  $S_1$  and  $S_2$  peak positions. The solid black line is the 4<sup>th</sup> order polynomial least-squares fit to experimental data, where the last two data points for the 12  $\mu\text{m}$  diameter droplets and the last data point for the 9  $\mu\text{m}$  diameter droplets are ignored due to high non-linearity in the detector response, which artificially decreases  $g_2$  (see Section 5.1.4). For comparison, the temperature dependence of  $g_2$  for the TIP4P/2005 (red dashed line) and SPC/E (purple dashed line) models are depicted along with the characteristic value of  $g_2$  for LDA ice [110] (dash-dotted blue line). The figure is reprinted with permission from Paper II.

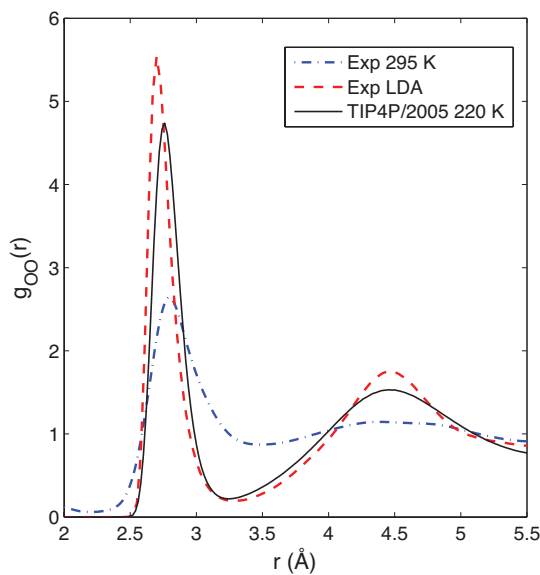


**Figure 6.5:** The oxygen-oxygen PCF of TIP4P/2005 water at 220 K (black solid line), representative of bulk liquid water at 229 K with same  $g_2$ , bears a striking similarity to LDA ice [110] (red dashed line), while the measured  $g_{OO}(r)$  of water at 295 K [5] (blue dash-dotted line) shows less structural correlation. The figure is reprinted with permission from Paper II.

## 6.2 X-ray Scattering and Absorption Spectroscopy of Ice

In this section, the results of Papers III-IV are summarized and a connection between the structure of the metastable liquid is made to the ice nucleation kinetics in deeply supercooled water. We find indications of a “fragile-to-strong” transition in deeply supercooled water, related to the structural transition toward an LDL observed in Paper II. Additionally, the crystalline phase prepared under various growth conditions is studied by XAS and the spectral features in the absorption spectrum are discussed in terms of the crystalline structure. We present a hypothesis where structural transitions in ice induced by the intense x-rays result in an enhanced pre-edge absorption cross-section, usually associated with distorted H-bonds.

### 6.2.1 Paper III — Homogeneous Ice Nucleation in Deeply Supercooled Water

The x-ray scattering at LCLS presented in Paper II yielded additional information regarding the homogeneous ice nucleation in deeply supercooled water. At the farthest distances from the nozzle, the droplets produced by the GDVNs crystallized rapidly, with an onset temperature of  $\sim 232$  K in agreement with  $T_h$  [8–10] at ambient pressure. As individual shots could be sorted into containing either pure diffuse water scattering or Bragg peaks indicative of crystalline order, the ice shot fraction could be calculated as a function of travel time in vacuum (see Fig. 5.9 and Tables 5.2 and 5.3). From these data, together with the temperature calibration discussed in Section 5.3.7, we could calculate according to Eq. (5.30) the homogeneous ice nucleation rate in bulk water below  $T_h$ , assuming it follows Poisson statistics and crystal growth is much faster than the formation of new ice nuclei (see Section 5.4.1). The resulting nucleation rates are presented in Fig. 6.6 and compared to already existing nucleation rate data. We obtain nucleation rates between  $2.1 \times 10^{11}$  to  $3.6 \times 10^{12} \text{ cm}^{-3} \text{ s}^{-1}$ , which are 2-9 orders of magnitude lower than previous measurements by Hagen *et al.* [259] in the same temperature range. However, Hagen *et al.* did not measure the temperature and diameter of the droplets. Instead, they relied on using a droplet growth model to estimate them, which may introduce large uncertainties to their highly temperature-dependent nucleation rate [260]. We will therefore discard measurements by Hagen *et al.* [259] from further analysis.

In general, all previous data presented in Fig. 6.6 can be classified into three groups: micron-sized droplets (denoted microdroplets) measured between 236–240 K at ambient pressure [243, 260–262], nanometer-sized droplets (denoted nanodroplets) measured between 170–215 K at an internal pressure

of 270-550 bar [14–16], and vapor-deposited thin films [254, 263]. CNT analysis (see Section 5.4.2 for details) reveals that previous microdroplets and nanodroplets data are consistent with “fragile” water. However, their large pressure difference together with the effects of nanoconfinement [17, 153] suggest that the two data groups should be analyzed separately. Thin film measurements deviate strongly, which highlights the complexity of growing well-characterized ice (discussed further in Section 6.2.2), but recent measurements by Amann-Winkel *et al.* [133] support the data by Jenniskens & Blake [254] consistent with “strong” water above  $T_g$  [264, 265]. The comparably low nucleation rates calculated from the measurements presented in Paper II lie in-between the expected behavior of “fragile” and “strong” liquids, and appear to support a “fragile-to-strong” transition just below  $T_h$ .

According to CNT (see Section 5.4.2), there are two quantities (both unknown in “no-man’s land”) that can explain the huge range of ice nucleation rates observed in experiments, namely the diffusivity  $D$  in Eq. (5.34), which makes up the kinetic energy barrier to move water molecules across the solid-liquid interface, and the solid-liquid interfacial free energy  $\sigma_{sl}$ , of which the thermodynamic energy barrier to form a critical nucleus in Eq. (5.38) is a cubic function. As described in detail in Paper III, we may analyze the CNT fits of microdroplets and nanodroplets data in two ways. We can fit  $\sigma_{sl}$  from nucleation rates using the method by Murray *et al.* [246], which assumes a weak temperature dependence of the diffusivity within a given data set, or we can fit existing measurements of  $D$  using the VFT law defined in Eq. (5.36) and extrapolate the measurements to “no-man’s land”. In Fig. 6.7 the derived diffusivity consistent with the experimentally observed nucleation rates using the former (solid line of CNT fits) and latter (dashed line of CNT fits) technique are compared to direct measurements. The high diffusivity predicted by the  $D_{VFT}$  fit forces the solid-liquid interfacial free energy to increase strongly below  $T_h$  for the microdroplets, which is very unlikely because the water structure (as seen in Paper II) is transitioning toward an LDL and becoming more similar to that of the crystal. Thus, our new data support a strong decrease in  $D$  (red solid line) below  $T_h$ , consistent with a “fragile-to-strong” transition in bulk liquid water. The situation is less clear for the nanodroplets, because the high nucleation rate observed in Fig. 6.6 allows  $\sigma_{sl}$  to obtain reasonable values for the  $D_{VFT}$  fit, and the validity of using the method by Murray *et al.* [246] is questionable since  $D$  is expected to change rapidly in “no-man’s land”. Nevertheless, the nucleation rate of “fragile” water is in general governed by the thermodynamic energy barrier, whereas “strong” water seems to be related to a strong increase in the kinetic energy barrier, so that it is comparable to (or even dominates over) the thermodynamic barrier toward nucleation. It has been argued by Kauzmann [115] and more recently by Moore & Molinero [148] that if a

metastable liquid is only inhibited by its kinetic energy barrier from forming the crystalline phase, it is no different from a glass. However, it should be noted that for the microdroplets presented in Paper II measured just below  $T_h$ , the thermodynamic energy barrier is still 2-3 times larger than the kinetic energy barrier, and we therefore consider our estimated nucleation rates to appropriately represent measurements of the metastable liquid.

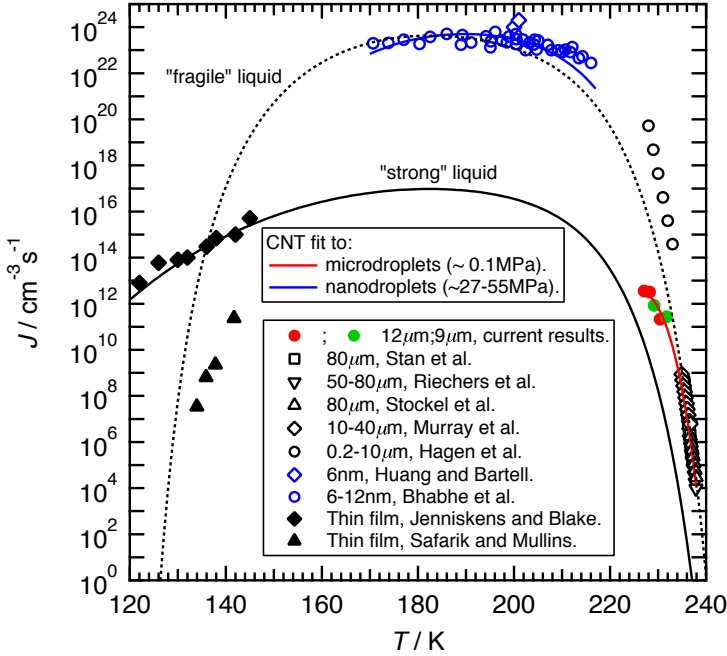


**Figure 6.6:** Comparison of homogeneous ice nucleation rates  $J$  of water ( $\text{H}_2\text{O}$ ) measured using microdroplets (227-240 K), nanodroplets (170-215 K), and vapor-deposited thin films (120-150 K). The authors of the original data sets are given in the legend, namely Stan *et al.* [243], Riechers *et al.* [261], Stöckel *et al.* [262], Murray *et al.* [260], Hagen *et al.* [259], Huang & Bartell [14], Bhabhe *et al.* [16], Jenniskens & Blake [254], and Safarik & Mullins [263]. Due to the large difference in internal pressure, the data of microdroplets (red solid line) and nanodroplets (blue solid line) are fitted separately to CNT. Our data (green and red filled circles) suggest slower increase in nucleation rate below  $T_h$  than previous data from Hagen *et al.* [259], which are excluded from the CNT fits. The expected CNT fits for a “fragile” (black dotted line) and “strong” (black solid line) liquid are included as guides to the eye.

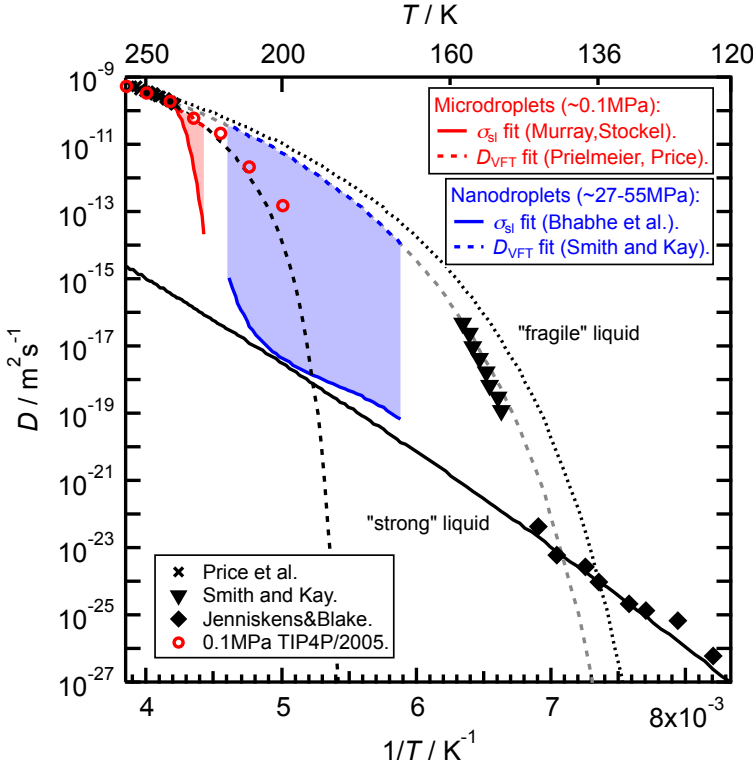


**Figure 6.7:** Derived diffusivity  $D$  of water ( $\text{H}_2\text{O}$ ) as a function of temperature. Diffusivity measurements performed by Price *et al.* [266] (black crosses and black fitted line) and Smith & Kay [11] (black filled triangles and gray fitted line) are fitted using the VFT law described by Eq. (5.36) and compared to  $D$  derived from ice nucleation rate data of microdroplets (red shaded area) and nanodroplets (blue shaded area) and MD simulations at 0.1 MPa using the TIP4P/2005 force field (red open circles). The range of  $D$  consistent with ice nucleation rate data was established using CNT together with  $\sigma_{sl}$  fits using the method by Murray *et al.* [246], which assumes a weak temperature dependence of the diffusivity within a given data set, applied to the data sets of Murray *et al.* [260], Stöckel *et al.* [262], and Riechers *et al.* [261] for the microdroplets (red solid line), and the data sets of Bhabhe *et al.* [16] for the nanodroplets (blue solid line). Alternatively, CNT was used together with  $D_{VFT}$  fits of the diffusivity data of Prielmeier *et al.* [267] and Price *et al.* [266] for the microdroplets (red dotted line), and data of Smith & Kay [11] for the nanodroplets (blue dotted line). The expected behavior of  $D$  for a “fragile” (black dotted line) and “strong” (black solid line) liquid are included as guides to the eye.



### 6.2.2 Paper IV – The Heterogeneous Structure of Crystalline Ice Films

In previous studies, the structure of water and its effect on ice nucleation kinetics have been studied. Additionally, the structure of ice still poses interesting questions to resolve. Although the structure of the crystalline phases with hexagonal (ice  $I_h$ ) and cubic (ice  $I_c$ ) order existing at ambient pressure are well-defined [100], their spectroscopic fingerprints have been intensely discussed. Specifically, it has been debated if the pre-edge absorption cross-section in XAS of ice  $I_h$  and ice  $I_c$  at  $\sim 535$  eV is an inherent feature of the crystalline phase or due to defects in crystal preparation. It has been proposed to be due to a localized core excitation, known as a core-exciton, in a tetrahedrally H-bonded network with only minor distortions [163,185,187]. It was further claimed that the change in pre-edge cross-section between water and ice is rather small, with a remaining pre-edge cross-section of the order 70% in bulk hexagonal ice [185]. In Paper IV, we show that large variations in pre-edge absorption cross-section can be obtained for crystalline ice films prepared under various growth conditions.

O K-edge x-ray absorption spectra of ice deposited on  $\text{BaF}_2(111)$  (black solid curve) and bulk ice prepared by freezing water between  $\text{Si}_3\text{N}_4$  membranes (red double-dotted curve) are compared in Fig. 6.8 to amorphous (blue dashed curve) and crystalline (green single-dotted curve) ice deposited on  $\text{Pt}(111)$  [71]. It is evident that the pre-edge absorption cross-section at 535 eV varies significantly between the various samples. In fact, Gaussian peak-fitting analysis performed in Paper IV showed that ice prepared on  $\text{BaF}_2(111)$  has a pre-edge absorption cross-section of about 40% of that of crystalline ices prepared differently. At the top of Fig. 6.8, difference spectra are shown with respect to liquid water at 299 K measured between  $\text{Si}_3\text{N}_4$  membranes in transmission yield. All difference spectra show strong depletion at the pre-edge, indicating that the pre-edge is already reduced for all ice spectra compared to liquid water.

Thus, we propose that in unperturbed ice there is only an extremely weak pre-edge (in agreement with the arguments presented in Section 4.1.2), where the small cross-section is due to vibronic coupling to asymmetric molecular vibrations that break the instantaneous near-tetrahedral symmetry [71, 85], similar to what is observed for the lowest excited state in methane [71]. This is also supported by 2D H-bonded adsorbed ice films on metal surfaces [86], measured with the electric field vector parallel to the surface, which indicate only a very weak pre-edge. In Paper IV, we present a hypothesis that could explain the large variations in experimentally determined pre-edge cross-sections. We can anticipate that the highly energetic x-rays will dump a lot of energy into the ice through the dominating Auger decay channel of the

core hole, which may be able to induce structural transitions in the ice to those with notable pre-edge absorption cross-sections. In fact, we show in Section 6.3.1 that the Auger decay even distorts the x-ray emission yield of liquid water at high fluences produced by a FEL. Thus, the pre-edge absorption cross-section in crystalline ice would be related to how effectively the ice or underlying substrate can take up the energy deposited by the high-energy electrons. This will be connected to the band structure of the ice, where defects and grain boundaries that disrupt the delocalized bands in the crystal will convert easily to high-density structures with distorted H-bonds, to which the pre-edge has been associated [71, 83, 84]. The  $\text{BaF}_2(111)$  surface reduces the number of defects by favoring growth of larger crystallites, hence showing a reduced pre-edge in the recorded spectrum at low flux. Nevertheless, it is difficult to completely eliminate the beam-induced decomposition of water on an insulating surface, and a small peak is observed at  $\sim 533$  eV, indicative of OH species bonded directly to the surface.

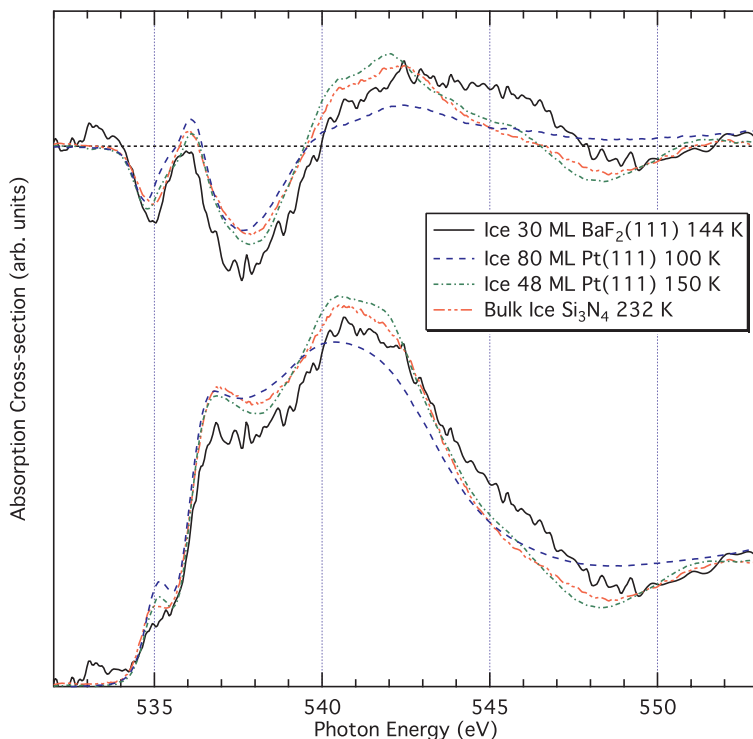


**Figure 6.8:** O K-edge x-ray absorption spectra of ice prepared under various growth conditions. SEY spectrum of crystalline ice prepared on  $\text{BaF}_2(111)$  (black solid curve) by depositing 30 ML of  $\text{D}_2\text{O}$  at 144 K; AEY spectrum of amorphous ice prepared on  $\text{Pt}(111)$  (blue dashed curve) by depositing 80 ML of  $\text{D}_2\text{O}$  at 100 K, an AEY spectrum of crystalline ice (green single-dotted curve) of 48 ML of  $\text{D}_2\text{O}$  was measured by annealing the amorphous film at 150 K and monitoring the desorption rate through mass spectrometry [71]; STXM spectrum of bulk crystalline ice (red double-dotted curve) at 232 K prepared by freezing an approximately 500 nm thick  $\text{H}_2\text{O}$  sample contained between  $\text{Si}_3\text{N}_4$  windows. The  $\text{D}_2\text{O}$  spectra were shifted -0.16 eV to correct for the difference in zero-point energy between the two isotopes; the reference spectra on  $\text{Pt}(111)$  [71] were shifted +0.3 eV to put all spectra on a common energy scale, as determined by the inflection point in the main-edge rise. All spectra were background subtracted and area normalized between 532.5 and 550 eV. The top section shows the difference in absorption cross-section compared to the STXM spectrum of bulk  $\text{H}_2\text{O}$  (l) measured at 299 K; the black dotted line denotes no difference.

### 6.3 X-ray Emission Spectroscopy of Liquid Water

In this section, I will summarize the results on XES of liquid water at FELs, presented in Papers V-VI. First, the various fluence regimes of O *K*-edge x-ray emission of H<sub>2</sub>O available at a FEL are studied, and it was shown that the emission yield increased non-linearly with peak fluence above  $\sim 0.2 \text{ J/cm}^2$ . A rate equation of reabsorption due to valence-excited molecules could describe this square-root-like fluence dependence of the emission yield, which was further found to saturate at  $\sim 2.8$  valence holes per molecule. Second, the temperature-dependent changes of the O *K*-edge x-ray emission of D<sub>2</sub>O were studied in the low-fluence regime with peak fluence below  $0.27 \text{ J/cm}^2$ , where spectral distortions due to reabsorption are minimized. The lone-pair region of the spectra, which is split up into a doublet and has been previously shown to be highly temperature-dependent in liquid water [60], was surprisingly insensitive to deep supercooling.

#### 6.3.1 Paper V – Valence-excited State Reabsorption of X-ray Emission at High Fluences

The O *K*-edge x-ray emission yield of H<sub>2</sub>O was measured with four different foci (horizontal  $\times$  vertical):  $25 \times 20 \mu\text{m}^2$ ,  $20 \times 70 \mu\text{m}^2$ ,  $35 \times 170 \mu\text{m}^2$ , and  $75 \times 520 \mu\text{m}^2$ . Additionally, beam transmission was scanned between  $\sim 1$ -100 % for each focal size, which enabled a continuous variation of the incident x-ray peak fluence between 0.01 and  $20 \text{ J/cm}^2$ . The x-ray emission yield and fluence were converted to detected and incident photons per water molecule, respectively, which is presented in Fig. 6.9a by the black markers (gray area is a confidence interval of one standard deviation). The linear dependence of detected photons with number of incident photons (represented by the dashed black line) is only observed at fluences below  $\sim 0.2 \text{ J/cm}^2$ , which is highlighted in the lower right inset over the low-fluence regime. Instead, a square-root-like fluence dependence is seen over the largest range measured, up to about  $10 \text{ J/cm}^2$ , after which a linear regime appears again but with a slope about four times lower than in the low-fluence regime.

The non-linear dependence of the x-ray emission yield could be accurately modeled by a rate equation of reabsorption (red solid line), which is described in Section 5.2.2, following Lambert-Beer's law. The reabsorption occurs due to an increased density of valence holes during the x-ray pulse length, which can reabsorb the emitted photons (originating from the radiative decay of the core-hole). To understand how such a large fraction of molecules in valence-excited states can appear within less than 100 fs, one has to remember that the dominating decay channel of a core-excited oxygen atom is non-radiative O *KLL* Auger decay, described in Section 2.5.5. The

Auger electron with an energy of about 500 eV [54] will scatter elastically and inelastically off neighboring water molecules, where the inelastic scattering will transfer part of the kinetic energy of the Auger electron to the neighboring molecules, creating valence-excited states. Since the time between individual scattering events is on the order of 100 as, a single Auger electron creates a cascade of valence excitations within a few femtoseconds [268–270] (assumed in the model to create 40 valence holes within 10 fs). Hence, a large valence hole density occurs already at incident photon concentrations of less than 1 % (per molecule), which is evident by the non-linear fluence dependence. At the same time, when a valence hole absorbs an emitted x-ray, the vast majority of the created core holes will once again decay through non-radiative *O KLL* Auger decay, further increasing the valence hole density and thus strengthening the non-linear behavior.

At fluences above  $\sim 10 \text{ J/cm}^2$  a new linear regime appears, which cannot be described accurately by the reabsorption model (as described in Section 5.2.2) unless the valence hole density saturates at  $\sim 2.8$  valence holes per molecule (red dashed line). However, from the simple reabsorption model based on the ground-state electronic structure of water, it should be possible to attain up to six valence holes per molecule. This implies that there are notable relaxation effects in the valence-excited state compared to the ground state, changing the valence hole density and the energy distribution of the reabsorption process, which is supported by deviations in spectral shape between the reabsorption model (gray dashed lines) and the recorded *OK*-edge x-ray emission spectra (colored solid lines) presented in Fig. 6.9b.

It should also be noted that the reabsorption model assumes that the valence holes have a much longer lifetime than the x-ray pulse length, which is reasonable since they can only decay by recombining with another photoelectron or dissipate outside of the probed volume. This is in stark contrast to the core holes initially created by the incident x-rays, with reported lifetime of 3–4 fs [43,44], which therefore only exist in very low concentrations throughout the pulse duration.

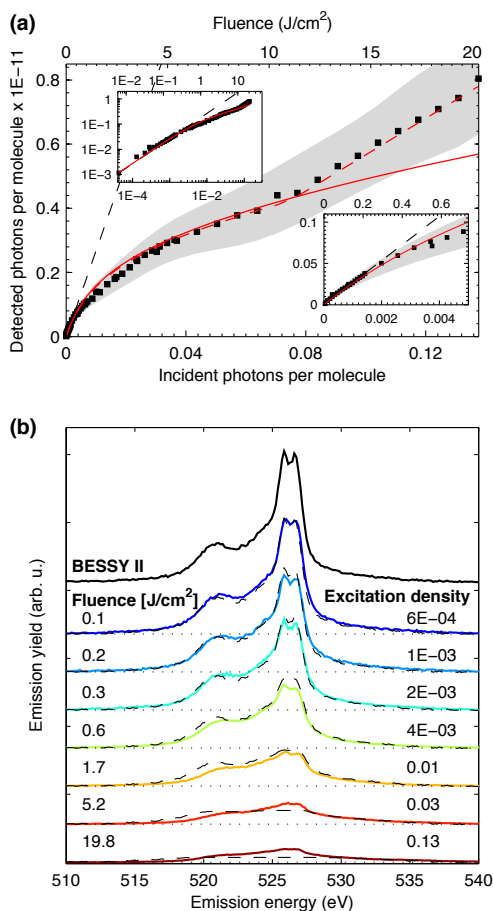


**Figure 6.9:** (a) Detected photons as a function of incident photons. Markers represent measured data and the gray shaded area gives a confidence interval of one standard deviation. The red curves (solid and dashed) are results of the reabsorption model described in Section 5.2.2. The black dashed line is a linear fit to the experimental data in the low fluence regime, which the lower right inset enlarges. The upper left inset shows the complete fluence range on a double logarithmic scale. (b) O K-edge x-ray emission spectra of  $\text{H}_2\text{O}$  from BESSY II (black solid curve) and for selected incident fluences at LCLS (colored curves). The black dashed curve superimposed with each LCLS spectrum is the result of the reabsorption model described in Section 5.2.2.

### 6.3.2 Paper VI – Assessing the Lone-pair Emission in Deeply Supercooled Water

Once the fluence dependence of the x-ray emission spectra had been established in Paper V, the temperature-dependent changes of water were studied with peak fluences below  $0.27 \text{ J/cm}^2$ , where spectral distortions due to reabsorption are minimized. We chose to focus on heavy water ( $\text{D}_2\text{O}$ ), as it has been shown to increase vibrational interference in the intermediate state compared to  $\text{H}_2\text{O}$  and thus the effect of the intermediate state is reduced [271]. We can understand this by expanding the ground-state wave function in the intermediate vibrational states according to the Franck-Condon principle. In the limit of full vibrational interference (*i.e.* infinitely short core-hole lifetime), the amplitudes (rather than the probabilities) are summed upon radiative decay and we recognize the original expansion of the ground-state wave function.

The OK-edge x-ray emission spectra of  $\text{D}_2\text{O}$  are shown in Fig. 6.10 for three sample-nozzle distances corresponding to  $\sim 290 \text{ K}$  (black line),  $226^{+2}_{-1} \text{ K}$  (red line), and  $222^{+5}_{-3} \text{ K}$  (green line) according to the Knudsen theory of evaporation (see Section 5.3.7). First we note that all three spectra show broad peaks at approximately 521 and 524 eV, corresponding to the bonding orbitals of  $1b_2$  and  $3a_1$ , respectively, and a doublet feature in the peak intensity at 526–527 eV, associated with the lone-pair orbital of water with  $1b_1$  character. This assessment – that the two peaks are indeed of  $b_1$  symmetry – has been verified by polarization dependent XES [164]. We denote the low-energy peak  $1b'_1$  and the high-energy peak  $1b''_1$ . At first sight, there are no spectral changes as a function of temperature above the noise level, but looking at the inset of Fig. 6.10, which highlights the lone-pair region of the spectra, we see that there is a decrease in spectral intensity at the high-energy side of the  $1b''_1$  peak. This effect is magnified in the difference spectra with respect to  $\sim 290 \text{ K}$  presented in the top of Fig. 6.10. The shift of the  $1b''_1$  peak is accompanied by slight increase and a possible shift to lower energies of the  $1b'_1$  and  $3a_1$  peaks, whereas the  $1b_2$  peak appears to become slightly weaker. Whether the latter effects are statistically significant is questionable, considering the level of noise and the spectral resolution.

Putting the x-ray emission results into the context of previous studies, what is most remarkable about the spectra is their similarity, given the large structural changes observed in the x-ray scattering in the same temperature range. This also appears to be in contrast with the strong temperature- and excitation energy-dependence of the  $1b_1$  peaks observed in previous studies [60, 167]. However, a peak fitting algorithm similar to what was employed by Tokushima *et al.* [60] is investigated in Paper VI, and the results appear to be in agreement. Six different hypotheses that could potentially explain the

x-ray emission spectra recorded in “no-man’s land” are proposed, and the interested reader is referred to the discussion in Paper VI.

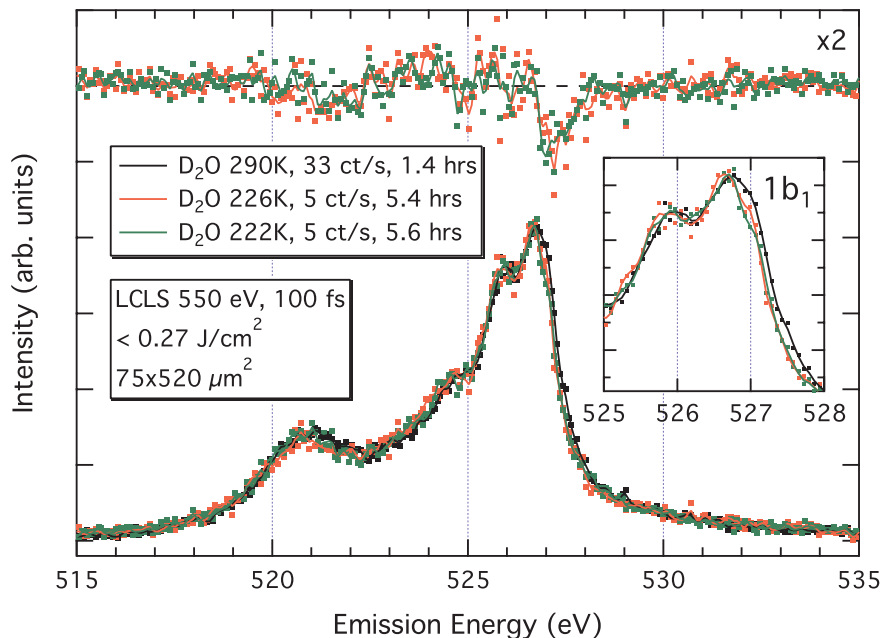


**Figure 6.10:** O K-edge x-ray emission spectra of liquid D<sub>2</sub>O measured at  $\sim 290$  K (black curve),  $226^{+2}_{-1}$  K (red curve), and  $222^{+5}_{-3}$  K (green curve). Count rate (ct/s), acquisition time (hrs), as well as experimental conditions are given for each spectrum. The top shows the difference spectra (magnified by a factor of 2) with respect to the x-ray emission spectrum of D<sub>2</sub>O at 290 K. The inset shows an enlarged view of the lone-pair (*1b<sub>1</sub>*) region of the x-ray emission spectra. All x-ray emission spectra were background subtracted with an 8<sup>th</sup> order polynomial and area normalized between 500 and 550 eV.



## Chapter 7

# Concluding Remarks and Outlook

This thesis has presented recent results on water and ice using x-rays. The local structure of liquid water has been probed from 339 K to 227 K using x-ray scattering, thus pushing the border of “no-man’s land” to a temperature comparable to  $T_S$ . In the ambient and hot regime, liquid water is characterized by a tetrahedrally coordinated minority that grows quickly upon cooling the liquid. When the liquid is supercooled, tetrahedrally coordinated structures grow rapidly and dominate the liquid below  $T_h$ . The metastable liquid could undergo rapid crystallization, differentiating it from a glass, and its structure was similar to that of LDA ice. We therefore propose a continuous transformation of bulk liquid water toward LDL at deeply supercooled temperatures.

The homogeneous nucleation rate of bulk water at near-atmospheric pressure is much lower around  $T_S$  than previous measurements and extrapolations above  $T_h$  have indicated, suggesting a sharp decrease in diffusivity by several orders of magnitude that is consistent with a “fragile-to-strong” transition in “no-man’s land”. We may connect the “fragile-to-strong” transition to the structural transformation toward LDL, implying that LDL is a “strong” liquid in agreement with thermodynamic [133, 264, 265] and dielectric relaxation [133] measurements of ultraviscous water formed by heating LDA ice (as well as ASW and HGW) above  $T_g$ . It is unclear if this transition also exists in nanoconfined water under elevated pressure, since nucleation rate data, in this case, are consistent with both “strong” and “fragile” behavior. Interestingly though, “strong” water appears to be related to diffusion-limited nucleation rates at temperatures way below  $T_h$ , which is in contrast to “fragile” water that is inhibited from crystallization by a thermodynamic

energy barrier to form critical nuclei everywhere in “no-man’s land”. As our experiments presented in Paper II only extend down to  $227^{+2}_{-1}$  K, we avoid speculations whether this behavior is relevant for bulk water, but it is clear that equilibration is one of the most challenging and essential questions to understand the properties of metastable water.

In addition to the diffusivity of supercooled water, the novel scattering data below 232 K also bring new insight into the thermodynamic models of supercooled water. Our experimental results cannot discriminate between the singularity-free scenario and the LLC model, which would require aid from MD simulations to infer the position of the apparent singularity from the rise in  $g_2$  upon supercooling. Due to the ongoing debate regarding liquid-liquid transitions in simulated water [149, 150, 152, 155, 272, 273], we refrain from conclusions whether experimental data supports the presence or absence of an LLC in bulk water. Nevertheless, our data give no indication of a discontinuous transition down to  $227^{+2}_{-1}$  K. Unless the discontinuous transitions predicted by the stability-limit conjecture and critical point-free model are shifted to significantly lower temperatures, our data therefore suggest that a singularity-free scenario or an LLC at higher pressure is most likely to occur in bulk water. This is consistent with thermodynamic arguments\* that have already proven the stability-limit conjecture to be highly unlikely [1]. To separate the two remaining models, measurements of the local structure or isobaric molar heat capacity at high pressure would be necessary, since the entropy and volume fluctuations are expected to increase when the LLC is approached [97], which is not the case for the singularity-free model [142].

The spectroscopic results presented in this thesis have reinforced the previously established assignment of the spectral features in XAS (see Section 3.7), namely that the pre-edge is associated with distorted or broken H-bonds [71, 83, 85, 86, 167], the main-edge is correlated with density and collapse of 2<sup>nd</sup> shell in  $g(r)$  [163], and the post-edge is associated with a H-bond  $\sigma^*$  resonance [71, 83, 86]. The weak pre-edge absorption cross-section of crystalline ice on BaF<sub>2</sub>(111) supports that unperturbed hexagonal ice would only give a pre-edge contribution due to vibronic coupling to asymmetric molecular vibrations that break the instantaneous near-tetrahedral symmetry. Instead, we raise questions over beam-induced structural transitions in ice due to Auger decay. The effect of the Auger decay and its subsequent cascade of secondary electrons was evident when measuring XES at a FEL. We established a rate equation of reabsorption to effectively model the non-linear fluence dependence of the x-ray emission yield and we found empirically that the valence hole density saturates at  $\sim 2.8$  holes per water molecule. Despite well-characterized fluence conditions, we did not observe a signifi-

---

\*The retracing spinodal would imply that there exists a second metastable vapor-liquid critical point, for which there is no experimental evidence that such a point exists [1].

cant change in peak ratio of the  $1b_1$  doublet in “no-man’s land” as expected from the structural transformation toward LDL, which indicates that the x-ray emission process is more complex than the previous assignment of two interconverting species [60]. Instead, a narrowing and shift of the  $1b_1''$  peak to lower energy is the only indication of the structural changes in “no-man’s land”, but the spectral changes are limited by the signal-to-noise ratio and the resolution of the spectrometer. To clearly distinguish the hypotheses discussed in Paper VI, further investigations with superior energy resolution are required. Measurements of radioactive tritiated water ( $T_2O$ ) should also be under consideration to increase the experimental information on the core-hole dynamics during the RIXS process.

We may conclude with an outlook to future investigations that show promise. To further shine light upon the equilibration and metastability limit of bulk liquid water, the temperature onset of homogeneous nucleation has to be pushed down at least 5-10 K further. This may be possible by consistent jet development and thorough characterization, so that stable droplet trains with uniform diameters of  $\sim 1\mu m$  at reasonably low speeds can be tailor made, and the scientific results may be very rewarding. At the same time, the answer to the origin of water’s anomalies requires innovative approaches to study supercooled water under pressure. Equally important is further technical development of the temperature calibration in “no-man’s land”. Current techniques rely on theoretical modeling and reference calibrations at higher temperatures, whereas avant-garde solutions of *in situ* temperature measurements with lasers or using black-body radiation may revolutionize the experimental knowledge of evaporative cooling. Last, much development is foreseen in the analysis of coherent scattering of water, where spatial and temporal correlations, which are currently limited by the detector response, may enable angular and dynamic information about the H-bonded network in liquid water to be accessed on ultrafast timescales.



# Populärvetenskaplig sammanfattning

Vatten är nödvändigt för vår överlevnad på jorden<sup>†</sup> och en fundamental förståelse för vattnets egenskaper är viktig inom alla naturvetenskapliga discipliner. Samtidigt är vatten den enda kemiska föreningen som förekommer naturligt som vätska (vatten), gas (vattenånga) och i fast form (is) vid atmosfärstryck, och uppvisar utöver detta många ovanliga egenskaper – så kallade anomalier<sup>‡</sup> – som skiljer sig från de flesta andra ämnen.

Denna avhandling fokuserar på nya experimentella studier av vatten och is genom användning av starka röntgenstrålar skapade av en så kallad frielektronlaser. Röntgenstrålar är användbara för att studera material, eftersom våglängden är tillräckligt kort för att det ska gå att avbilda atomer. Samtidigt är röntgenpulserna skapade av frielektronlasern så korta att atomerna inte hinner röra sig – pulserna varar nämligen endast den tid det tar för ljus att färdas tjockleken av ett hårstrå<sup>§</sup>. Trots att de är så korta har de samma ljusstyrka varje sekund som de starkaste bland andra typer av röntgenkällor som finns tillgängliga, vilket har skapat nya forskningsmöjligheter med utvecklingen av frielektronlasern.

Generellt skiljer sig vätskor, såsom vatten, avsevärt från de flesta fasta material som är gjorda av kristaller. En kristall, som till exempel is, kan beskrivas av en enhetscell<sup>¶</sup> innehållande endast ett fåtal vattenmolekyler<sup>||</sup> som vi kan kopiera upp i alla riktningar. Detta medför att det finns ordning i kristallerna – om vi vet var en viss molekyl befinner sig, kan vi stega

---

<sup>†</sup>För en längre motivering och en beskrivning av utmaningarna som ligger framför oss, se FN:s vatteninitiativ: <http://www.un.org/waterforlifedecade/background.shtml>

<sup>‡</sup>För en ambitiös sammanställning av dessa anomalier, se: <http://www1.lsbu.ac.uk/water/anmlies.html>

<sup>§</sup>Det tar ljus 2.4s att färdas fram och tillbaka till månen, vilket gör att ljus kan färdas tjockleken av ett hårstrå på endast  $100 \times 10^{-15} \text{ s} = 100 \text{ fs}$ .

<sup>¶</sup>Tänk er en legobit som kan kopplas samman med likadana legobitar i alla riktningar.

<sup>||</sup>En vattenmolekyl består av två väteatomer (H) och en syreatom (O) sammansatta i en "V"-liknande formation med en H-O-H vinkel mellan väteatomerna på  $104.52^\circ$ .

bort ett godtyckligt antal enhetsceller och lokalisera var en annan molekyl måste vara<sup>\*\*</sup>. En vätska å andra sidan har ingen ordning, vilket betyder att även om vi vet var en vattenmolekyl befinner sig i vätskan vid en viss tidpunkt, kan vi inte lokalisera en annan molekyl ett godtyckligt antal enhetsceller bort. Av detta följer att en vätska ser likadan ut i alla riktningar så att det inte heller finns någon favoriserad riktning i vätskan. Trots denna oordning, om vi förflyttar oss tillräckligt korta avstånd i vätskan lokalt kring en vattenmolekyl, så finner vi ordning! Denna lokala ordning beskriver hur en vattenmolekyl orienterar sig gentemot sina närmaste grannar. Det visar sig något kontraintuitivt att vattenmolekylerna föredrar energimässigt att bilda ett öppet nätverk med endast fyra närmaste grannar ordnade likt en tetraeder kring varandra, vilket resulterar i en låg densitet, men den termiska oordningen gör att vattenmolekylerna packas tätare och ger en högre densitet i vätskan. Det är detta som gör att is har lägre densitet än vatten – en av vattens mest kända anomalier – och att iskuben således flyter på vattnet i vårt glas.

Vi har använt frielektronlasern vid SLAC National Accelerator Laboratory, USA, för att kyla vatten under dess fryspunkt och avbilda strukturen i vätskan. Vatten har många unika egenskaper, men en av dem är att det kan kylas långt under sin fryspunkt, speciellt när det studeras i väldigt små volymer. Därför lät vi mikrometerstora vattendroppar avdunsta i vakuum och lyckades avbilda vätskans struktur ända ner till  $-46^{\circ}\text{C}$ , vilket är temperaturen där vattnets anomalier har antagits vara som starkast. Trots detta har ingen i vår vetenskap tidigare lyckats att mäta vatten vid atmosfärstryck i dess "ingenmansland" mellan  $-41^{\circ}\text{C}$  och  $-116^{\circ}\text{C}$ . Vi fann att strukturen i vätskan övergår gradvis mot en vätska med låg densitet och tetraedriskt koordinerade grannmolekyler. Vid  $-44^{\circ}\text{C}$ , när denna lågdensitetsstruktur börjar dominera, fryser vätskan snabbt till is och vi kan undersöka hur snabbt is bildas jämfört med tidigare studier vid högre temperaturer. Detaljer kring experimenten tillsammans med deras konsekvenser för vattnets struktur diskuteras i avhandlingen.

---

<sup>\*\*</sup>Detta brukar kallas för translationell ordning, eftersom vi kan förflytta oss från en vattenmolekyl till en annan med hjälp av en translation av ett godtyckligt antal enhetsceller.

# Acknowledgements

First of all, I would like to thank **Anders** for believing in me and giving me the opportunity to work in your group. Your knowledge and intuition inspire me to perform great research. I am also very grateful for the guidance I have received from **Lars** who always encourages me to become a better scientist. Thank you for taking time to discuss and explain experiments as well as theory, and your commitment to reading and commenting manuscripts is highly appreciated.

In addition to my supervisors, this work would never have been possible without my many mentors. Thank you **Congcong** for being an exceptional scientist who is both modest and thorough. Thank you **Jan** and **Duane** for teaching me so much about programming and all the exciting discussions about scattering theory. Thank you **Sarp**, **Dennis**, and **Hirohito** for your countless hours of beam line support and for always explaining how to make the most out of a planned experiment. I am impressed with your knowledge and dedication to science.

I am also filled with gratitude for the help and joy from all my colleagues. Thank you **Ira** for showing me how everything works at SLAC. Thank you **Trevor**, **Chen Chen**, and **Ningdong** for all the work on water together. Thanks everyone else in the group for making life fun at SLAC: **Tetsuo**, **May Ling**, **Daniel Friebe**, **Hernan**, **Kaj**, **Anders**, **Felix**, **Toyli**, and **Sangwan**. Special thanks to **Dan Miller** and **Srivats** for all the good times in the gym, **Jerry** for the beer brewing, **Derek** and **Sebastian** for the climbing, and **Martin** and **TJ** for the bike rides. Thanks to all collaborators: **Mike**, **Hartawan**, **Ray** (go Gators!), **Christina**, **Dmitri**, **Dan DePonte**, **Simon**, **Wilson**, **Philippe**, **Flo**, **Martina**, **Wilfred**, **Alexander**, **Seb**, **Daniel Ratner**, **Lee-Ping**, **Jongmin**, **Andrew**, **Anton**, **Chiara**, **Jan**, **Uwe**, **Junko**, **Vittal**, and **Benedikt**. Thanks to all beam line scientists: **Sebastien**, **Garth**, **Bill**, **Josh**, **Georgi**, **Tolek**, **Mary**, and **Thomas**. Thanks to **Michelle** for always taking care of my problems.

I am grateful for all the good times with the Stockholm group. Thank you **Henrik**, **Daniel**, **Mathias**, **Thor**, **Micke**, **Iurii**, **Jörgen**, and **Henrik** for

all the beers, help, and discussions. Special thanks to **Daniel** and **Thor** for proof-reading and giving constructive comments. Thanks to **Ulf**, **André**, and **Henrik** for getting me through Landau and Lifshitz [29].

The support from my family has also been invaluable to me. Thank you **mom** for all your proof-reading. Thank you **Fredrik** for the guidance throughout my education, you always know the answer to what to do next. Thank you **Henrik** for informing me about the PhD position, it has been great to be able to study together with you for so many years. Thank you **Lena** and **Åmis** for awakening my interest in chemistry and physics. Without all of you, I would not be here today.

Finally, lots of love to **Maggie** for always being there and making my life extraordinary. Saranghae!



# References

- [1] Debenedetti, P. G., J. Phys.: Condens. Matter **15** (2003) R1669.
- [2] Angell, C. A., Sichina, W. J., and Oguni, M., J. Phys. Chem. **86** (1982) 998.
- [3] Fu, L., Bienenstock, A., and Brennan, S., J. Chem. Phys. **131** (2009) 234702.
- [4] Neufeind, J., Benmore, C. J., Weber, J. K. R., and Paschek, D., Mol. Phys. **109** (2011) 279.
- [5] Skinner, L. B. et al., J. Chem. Phys. **138** (2013) 74506.
- [6] Rasmussen, D. H. and MacKenzie, A. P., J. Chem. Phys. **59** (1973) 5003.
- [7] Speedy, R. J. and Angell, C. A., J. Chem. Phys. **65** (1976) 851.
- [8] Cwilog, B. M., Proc. R. Soc. Lond. A **190** (1947) 137.
- [9] Mason, B. J., Adv. Phys. **7** (1958) 221.
- [10] Thomas, D. G. and Staveley, L. A. K., J. Chem. Soc. (1952) 4569.
- [11] Smith, R. S. and Kay, B. D., Nature **398** (1999) 788.
- [12] Liu, D. et al., Proc. Natl. Acad. Sci. (USA) **104** (2007) 9570.
- [13] Mallamace, F. et al., Proc. Natl. Acad. Sci. (USA) **104** (2007) 424.
- [14] Huang, J. and Bartell, L. S., J. Phys. Chem. **99** (1995) 3924.
- [15] Manka, A. et al., Phys. Chem. Chem. Phys. **14** (2012) 4505.
- [16] Bhabhe, A., Pathak, H., and Wyslouzil, B. E., J. Phys. Chem. A **117** (2013) 5472.
- [17] Levinger, N. E., Science **298** (2002) 1722.
- [18] Hertz, H., Ann. Phys. **267** (1887) 983.
- [19] Board of Regents, S. I., *Report of the Board of Regents*, Publication (Smithsonian Institution), The Institution, 1914.
- [20] Jackson, J. D., *Classical Electrodynamics*, Wiley, New York, 1998.
- [21] Einstein, A., Ann. Phys. **322** (1905) 132.
- [22] Hubbell, J. H., Gimm, H. A., and Øverbø, I., J. Phys. Chem. Ref. Data **9** (1980).
- [23] Henke, B. L., Gullikson, E. M., and Davis, J. C., Atom. Data Nucl. Data Tables **54** (1993) 181.
- [24] Stöhr, J., *NEXAFS Spectroscopy*, Springer-Verlag, Berlin Heidelberg, 1992.

- [25] Thompson, A. et al., *X-ray Data Booklet*, Lawrence Berkeley National Laboratory, Berkeley, 2009.
- [26] Compton, A. H., *Phys. Rev.* **21** (1923) 483.
- [27] Klein, O. and Nishina, Y., *Z. Phys.* **52** (1929) 853.
- [28] Sellberg, J. A., *Temperature-dependent X-ray Scattering of Liquid Water*, Licentiate thesis, Stockholm University, 2012.
- [29] Landau, L. D. and Lifshitz, E. M., *Quantum Mechanics (Non-relativistic Theory)*, Butterworth-Heinemann, Oxford, 3rd edition, 1981.
- [30] Messiah, A., *Quantum Mechanics*, Dover Publications Inc., Mineola, 1999.
- [31] Warren, B. E., *X-ray Diffraction*, Dover Publications Inc., Mineola, 1990.
- [32] Debye, P., *Ann. Phys.* **46** (1915) 809.
- [33] Hansen, J.-P. and McDonald, I. R., *Theory of Simple Liquids*, Academic Press, London, 3rd edition, 2008.
- [34] Waser, J. and Schomaker, V., *Rev. Mod. Phys.* **25** (1953) 671.
- [35] Wikfeldt, K. T., *Structure, Dynamics and Thermodynamics of Liquid Water*, PhD thesis, Stockholm University, 2011.
- [36] Soper, A. K., *J. Phys.: Cond. Mat.* **19** (2007) 335206.
- [37] Sorenson, J. M., Hura, G., Glaeser, R. M., and Head-Gordon, T., *J. Chem. Phys.* **113** (2000) 9149.
- [38] Narten, A. H. and Levy, H. A., *J. Chem. Phys.* **55** (1971) 2263.
- [39] Kittel, C., *Introduction to Solid State Physics*, John Wiley & Sons, Inc., Hoboken, 8th edition, 2005.
- [40] Clark, J. N. et al., *Science* **341** (2013) 56.
- [41] Nilsson, A. and Pettersson, L. G. M., Adsorbate Electronic Structure and Bonding on Metal Surfaces, in *Chemical Bonding at Surfaces and Interfaces*, edited by Nilsson, A., Pettersson, L. G. M., and Nørskov, J. K., Elsevier, Amsterdam, 2008.
- [42] Nordlund, D., *Core Level Spectroscopy of Water and Ice*, PhD thesis, Stockholm University, 2004.
- [43] Neeb, M., Rubensson, J. E., Biermann, M., and Eberhardt, W., *J. El. Spec. Rel. Phen.* **67** (1994) 261.
- [44] Sorensen, S. L. et al., *Phys. Rev. A* **64** (2001) 12719.
- [45] Townsend, J. S., *A Modern Approach to Quantum Mechanics*, University Science Books, Sausalito, 2000.
- [46] Leetmaa, M., *Structure Modeling with X-ray Absorption and Reverse Monte Carlo: Applications to Water*, PhD thesis, Stockholm University, 2009.
- [47] Dirac, P. A. M., *Proc. R. Soc. Lond. A* **114** (1927) 243.
- [48] Moss, R. E., *Advanced molecular quantum mechanics*, Chapman and Hall, London, 1973.

- [49] Harris, D. C. and Bertolucci, M. D., *Symmetry and Spectroscopy: An Introduction to Vibrational and Electronic Spectroscopy*, Oxford University Press, New York, 1978.
- [50] Atkins, P. and de Paula, J., *Atkins' Physical Chemistry*, Oxford University Press, New York, 7th edition, 2002.
- [51] Kramers, H. A. and Heisenberg, W., *Z. Phys.* **31** (1925) 681.
- [52] Gel'mukhanov, F. and Ågren, H., *Phys. Reps.* **312** (1999) 87.
- [53] Sandell, A., Nilsson, A., Björneholm, O., Tillborg, H., and Mårtensson, N., *Phys. Rev. B* **48** (1993) 11347.
- [54] Nordlund, D. et al., *Phys. Rev. Lett.* **99** (2007) 217406.
- [55] Wurth, W. and Menzel, D., *Chem. Phys.* **251** (2000) 141.
- [56] Nilsson, A., *J. El. Spec. Rel. Phenom.* **126** (2002) 3.
- [57] Brühwiler, P., Karis, O., and Mårtensson, N., *Rev. Mod. Phys.* **74** (2002) 703.
- [58] Ben-Naim, A., *Molecular Theory of Water and Aqueous Solutions; Part 1: Understanding Water*, World Scientific Publishing Co. Pte. Ltd., Singapore, 2009.
- [59] Clough, S. A., Beers, Y., Klein, G. P., and Rothman, L. S., *J. Chem. Phys.* **59** (1973) 2254.
- [60] Tokushima, T. et al., *Chem. Phys. Lett.* **460** (2008) 387.
- [61] Reed, A. E., Curtiss, L. A., and Weinhold, F., *Chem. Rev.* **88** (1988) 899.
- [62] Buckingham, A. D., Fowler, P. W., and Hutson, J. M., *Chem. Rev.* **88** (1988) 963.
- [63] King, B. F. and Weinhold, F., *J. Chem. Phys.* **103** (1995) 333.
- [64] Stone, A. J., Buckingham, A. D., and Fowler, P. W., *J. Chem. Phys.* **107** (1997) 1030.
- [65] Dang, L. X., *J. Phys. Chem. B* **102** (1998) 620.
- [66] Dannenberg, J. J., Haskamp, L., and Masunov, A., *J. Phys. Chem. A* **103** (1999) 7083.
- [67] Fulton, R. L. and Perhacs, P., *J. Phys. Chem. A* **102** (1998) 9001.
- [68] Gregory, J. K., Clary, D. C., Liu, K., Brown, M. G., and Saykally, R. J., *Science* **275** (1997) 814.
- [69] Silvestrelli, P. L. and Parrinello, M., *Phys. Rev. Lett.* **82** (1999) 3308.
- [70] Nilsson, A. et al., *J. Chem. Phys.* **122** (2005) 154505.
- [71] Nilsson, A. et al., *J. El. Spec. Rel. Phen.* **177** (2010) 99.
- [72] Ojamäe, L. and Hermansson, K., *J. Phys. Chem.* **98** (1994) 4271.
- [73] Hohenberg, P. and Kohn, W., *Phys. Rev.* **136** (1964) B864.
- [74] Kohn, W. and Sham, L. J., *Phys. Rev.* **140** (1965) A1133.
- [75] Becke, A. D., *J. Chem. Phys.* **98** (1993).
- [76] Stephens, P. J., Devlin, F. J., Chabalowski, C. F., and Frisch, M. J., *J. Phys. Chem.* **98** (1994) 11623.

- [77] Ludwig, R., *Phys. Chem. Chem. Phys.* **4** (2002) 5481.
- [78] Cruzan, J. D. et al., *Science* **271** (1996) 59.
- [79] Liu, K., Brown, M. G., Cruzan, J. D., and Saykally, R. J., *Science* **271** (1996) 62.
- [80] Liu, K., Cruzan, J. D., and Saykally, R. J., *Science* **271** (1996) 929.
- [81] Badger, R. M., *J. Chem. Phys.* **2** (1934) 128.
- [82] Kumar, R., Schmidt, J. R., and Skinner, J. L., *J. Chem. Phys.* **126** (2007) 204107.
- [83] Wernet, P. et al., *Science* **304** (2004) 995.
- [84] Myneni, S. et al., *J. Phys.: Condens. Matter* **14** (2002) L213.
- [85] Cavalleri, M., Ogasawara, H., Pettersson, L. G. M., and Nilsson, A., *Chem. Phys. Lett.* **364** (2002) 363.
- [86] Nordlund, D. et al., *Phys. Rev. B* **80** (2009) 233404.
- [87] Berendsen, H. J. C., Grigera, J. R., and Straatsma, T. P., *J. Phys. Chem.* **91** (1987) 6269.
- [88] Salzmann, C. G., Radaelli, P. G., Mayer, E., and Finney, J. L., *Phys. Rev. Lett.* **103** (2009) 105701.
- [89] Guildner, L. A., Johnson, D. P., and Jones, F. E., *J. Res. Natl. Bur. Stand.* **80A** (1976) 505.
- [90] Lide, D. R., *CRC Handbook of Chemistry and Physics*, CRC Press/Taylor and Francis, Boca Raton, 90th edition, 2010.
- [91] Bridgman, P. W., *Proc. Am. Acad. Arts Sci.* **47** (1912) 441.
- [92] Murphy, D. M. and Koop, T., *Q. J. R. Meteorol. Soc.* **131** (2005) 1539.
- [93] Lee, C. M. G., [http://en.wikipedia.org/wiki/File:Phase\\_diagram\\_of\\_water.svg](http://en.wikipedia.org/wiki/File:Phase_diagram_of_water.svg), 2013.
- [94] Chaplin, M., <http://www1.lsbu.ac.uk/water/phase.html>, 2014.
- [95] Chaplin, M., <http://ergodic.ugr.es/termo/lecciones/water1.html>, 2011.
- [96] Lennard-Jones, J. E., *Proc. Phys. Soc.* **43** (1931) 461.
- [97] Stanley, H. E., *Introduction to Phase Transitions and Critical Phenomena*, Oxford University Press, New York, 1987.
- [98] Landau, L. D. and Lifshitz, E. M., *Statistical Physics Part 1*, Butterworth-Heinemann, Oxford, 3rd edition, 1980.
- [99] Petrenko, V. F. and Whitworth, R. W., *Physics of ice*, Oxford University Press, Oxford, 1999.
- [100] Dowell, L. G. and Rinfret, A. P., *Nature* **188** (1960) 1144.
- [101] Murray, B. J., Knopf, D. A., and Bertram, A. K., *Nature* **434** (2005) 202.
- [102] Mayer, E. and Hallbrucker, A., *Nature* **325** (1987) 601.
- [103] Kuhs, W. F., Bliss, D. V., and Finney, J. L., *J. Phys. Colloques* **48** (1987) 631.
- [104] Hansen, T. C., Koza, M. M., and Kuhs, W. F., *J. Phys.: Condens. Matter* **20** (2008) 285104.

- [105] Hansen, T. C., Koza, M. M., Lindner, P., and Kuhs, W. F., J. Phys.: Condens. Matter **20** (2008) 285105.
- [106] Kuhs, W. F., Sippel, C., Falenty, A., and Hansen, T. C., Proc. Natl. Acad. Sci. (USA) **109** (2012) 21259.
- [107] Malkin, T. L., Murray, B. J., Brukhno, A. V., Anwar, J., and Salzmann, C. G., Proc. Natl. Acad. Sci. (USA) **109** (2012) 1041.
- [108] Kuhs, W. F., Genov, G., Staykova, D. K., and Hansen, T., Phys. Chem. Chem. Phys. **6** (2004) 4917.
- [109] Tulk, C. A. et al., Science **297** (2002) 1320.
- [110] Bowron, D. T. et al., J. Chem. Phys. **125** (2006) 194502.
- [111] Giovambattista, N., Amann-Winkel, K., and Loerting, T., Amorphous Ices, in *Liquid Polymorphism*, pages 139–173, John Wiley & Sons, Inc., 2013.
- [112] McMillan, J. A. and Los, S. C., Nature **206** (1965) 806.
- [113] Johari, G. P., Hallbrucker, A., and Mayer, E., Nature **330** (1987) 552.
- [114] Elsaesser, M. S., Winkel, K., Mayer, E., and Loerting, T., Phys. Chem. Chem. Phys. **12** (2010) 708.
- [115] Kauzmann, W., Chem. Rev. **43** (1948) 219.
- [116] Mishima, O., Calvert, L. D., and Whalley, E., Nature **314** (1985) 76.
- [117] Mishima, O., J. Chem. Phys. **100** (1994) 5910.
- [118] Poole, P. H., Sciortino, F., Essmann, U., and Stanley, H. E., Nature **360** (1992) 324.
- [119] Mishima, O. and Stanley, H. E., Nature **396** (1998) 329.
- [120] Brüggeller, P. and Mayer, E., Nature **288** (1980) 569.
- [121] Mayer, E., J. Appl. Phys. **58** (1985) 663.
- [122] Kohl, I., Bachmann, L., Hallbrucker, A., Mayer, E., and Loerting, T., Phys. Chem. Chem. Phys. **7** (2005) 3210.
- [123] Burton, E. F. and Oliver, W. F., Nature **135** (1935) 505.
- [124] Venkatesh, C. G., Rice, S. A., and Narten, A. H., Science **186** (1974) 927.
- [125] Loerting, T. et al., J. Phys. Chem. B **115** (2011) 14167.
- [126] Mishima, O., Calvert, L. D., and Whalley, E., Nature **310** (1984) 393.
- [127] Suzuki, Y. and Mishima, O., J. Phys. Soc. Jpn. **72** (2003) 3128.
- [128] Finney, J. L., Hallbrucker, A., Kohl, I., Soper, A. K., and Bowron, D. T., Phys. Rev. Lett. **88** (2002) 225503.
- [129] Tulk, C. A., Hart, R., Klug, D. D., Benmore, C. J., and Neufeind, J., Phys. Rev. Lett. **97** (2006) 115503.
- [130] Mishima, O., Takemura, K., and Aoki, K., Science **254** (1991) 406.
- [131] Winkel, K., Mayer, E., and Loerting, T., J. Phys. Chem. B **115** (2011) 14141.

- [132] Nelmes, R. J. et al., Nat Phys **2** (2006) 414.
- [133] Amann-Winkel, K. et al., Proc. Natl. Acad. Sci. (USA) **110** (2013) 17720.
- [134] Loerting, T., Salzmann, C., Kohl, I., Mayer, E., and Hallbrucker, A., Phys. Chem. Chem. Phys. **3** (2001) 5355.
- [135] Finney, J. L. et al., Phys. Rev. Lett. **89** (2002) 205503.
- [136] Winkel, K., Elsaesser, M. S., Mayer, E., and Loerting, T., J. Chem. Phys. **128** (2008) 044510.
- [137] Salzmann, C. G. et al., Phys. Chem. Chem. Phys. **8** (2006) 386.
- [138] Lienhard, J. H., Shamsundar, N., and Biney, P. O., Nucl. Eng. Des. **95** (1986) 297.
- [139] Prielmeier, F. X., Lang, E. W., Speedy, R. J., and Lüdemann, H.-D., Phys. Rev. Lett. **59** (1987) 1128.
- [140] Angell, C. A., Nature **331** (1988) 206.
- [141] Angell, C. A., Science **319** (2008) 582.
- [142] Rebelo, L. P. N., Debenedetti, P. G., and Sastry, S., J. Chem. Phys. **109** (1998) 626.
- [143] Huang, C. et al., Proc. Natl. Acad. Sci. (USA) **106** (2009) 15214.
- [144] Kim, C. U., Barstow, B., Tate, M. W., and Gruner, S. M., Proc. Natl. Acad. Sci. (USA) **106** (2009) 4596.
- [145] Stokely, K., Mazza, M. G., Stanley, H. E., and Franzese, G., Proc. Natl. Acad. Sci. (USA) **107** (2010) 1301.
- [146] Stanley, H. E., *Mysteries of Water*, May, Les Houches Lecture, 1998.
- [147] Swenson, J. and Teixeira, J., J. Chem. Phys. **132** (2010) 14508.
- [148] Moore, E. B. and Molinero, V., Nature **479** (2011) 506.
- [149] Limmer, D. T. and Chandler, D., J. Chem. Phys. **135** (2011) 134503.
- [150] Limmer, D. T. and Chandler, D., J. Chem. Phys. **138** (2013) 214504.
- [151] Liu, Y., Panagiotopoulos, A. Z., and Debenedetti, P. G., J. Chem. Phys. **131** (2009) 104508.
- [152] Liu, Y., Palmer, J. C., Panagiotopoulos, A. Z., and Debenedetti, P. G., J. Chem. Phys. **137** (2012) 214505.
- [153] Soper, A. K., J. Phys.: Condens. Matter **24** (2012) 64107.
- [154] Molinero, V. and Moore, E. B., J. Phys. Chem. B **113** (2009) 4008.
- [155] Palmer, J. C., Car, R., and Debenedetti, P. G., Faraday Discuss. **167** (2013) 77.
- [156] Whiting, H., *A new theory of cohesion applied to the thermodynamics of liquids and solids*, PhD thesis, Harvard University, 1884.
- [157] Röntgen, W. C., Ann. Phys. **45** (1892) 91.
- [158] Bernal, J. D. and Fowler, R. H., J. Chem. Phys. **1** (1933) 515.
- [159] Narten, A. H. and Levy, H. A., Science **165** (1969) 447.
- [160] Chen, S.-H. and Teixeira, J., Adv. Chem. Phys. **64** (1986) 1.

- [161] Soper, A. K. and Ricci, M. A., Phys. Rev. Lett. **84** (2000) 2881.
- [162] Rahman, A. and Stillinger, F. H., J. Chem. Phys. **55** (1971) 3336.
- [163] Pylkkänen, T. et al., J. Phys. Chem. B **114** (2010) 3804.
- [164] Tokushima, T. et al., J. Chem. Phys. **136** (2012) 044517.
- [165] Fuchs, O. et al., Phys. Rev. Lett. **100** (2008) 27801.
- [166] Odelius, M., Phys. Rev. B **79** (2009) 144204.
- [167] Harada, Y. et al., Phys. Rev. Lett. **111** (2013) 193001.
- [168] Winter, B. et al., J. Phys. Chem. A **108** (2004) 2625.
- [169] Winter, B., Aziz, E. F., Hergenhahn, U., Faubel, M., and Hertel, I. V., J. Chem. Phys. **126** (2007) 124504.
- [170] Leetmaa, M. et al., J. Chem. Phys. **129** (2008) 84502.
- [171] Egelstaff, P. A., *An Introduction to the Liquid State*, Academic Press, New York, 1967.
- [172] Bosio, L., Teixeira, J., and Stanley, H. E., Phys. Rev. Lett. **46** (1981) 597.
- [173] Huang, C. et al., J. Chem. Phys. **133** (2010) 134504.
- [174] Torquato, S. and Stillinger, F., Phys. Rev. E **68** (2003) 041113.
- [175] Ivanenko, D. D. and Sokolov, A. A., Doklady Akad. Nauk SSSR **59** (1948) 1551.
- [176] Schwinger, J., Phys. Rev. **75** (1949) 1912.
- [177] Elder, F. R., Gurewitsch, A. M., Langmuir, R. V., and Pollock, H. C., Phys. Rev. **71** (1947) 829.
- [178] Altarelli, M., Crystallogr. Rep. **55** (2010) 1145.
- [179] Attwood, D. T., *Soft X-Rays and Extreme Ultraviolet Radiation: Principles and Applications*, Cambridge University Press, Cambridge, 2000.
- [180] Winick, H., Properties of Synchrotron Radiation, in *Synchrotron Radiation Research*, edited by Winick, H. and Doniach, S., Plenum, New York, 1979.
- [181] Sands, M., SLAC-R-121, The Physics of Electron Storage Rings: An Introduction, Technical report, SLAC National Accelerator Laboratory, Menlo Park, 1970.
- [182] Okhulkov, A. V., Demianets, Y. N., and Gorbaty, Y. E., J. Chem. Phys. **100** (1994) 1578.
- [183] Hura, G., Sorenson, J. M., Glaeser, R. M., and Head-Gordon, T., J. Chem. Phys. **113** (2000) 9140.
- [184] Näslund, L.-Å. et al., J. Phys. Chem. B **109** (2005) 13835.
- [185] Pylkkänen, T. et al., J. Phys. Chem. B **115** (2011) 14544.
- [186] Parent, P., Laffon, C., Mangeney, C., Bournel, F., and Tronc, M., J. Chem. Phys. **117** (2002) 10842.
- [187] Tse, J. S. et al., Phys. Rev. Lett. **100** (2008) 95502.

- [188] Näslund, L.-Å. et al., J. Phys. Chem. A **109** (2005) 5995.
- [189] Cappa, C. D. et al., J. Phys. Chem. B **109** (2005) 7046.
- [190] Cappa, C. D., Smith, J. D., Messer, B. M., Cohen, R. C., and Saykally, R. J., J. Phys. Chem. B **110** (2006) 1166.
- [191] Cappa, C. D., Smith, J. D., Messer, B. M., Cohen, R. C., and Saykally, R. J., J. Phys. Chem. A **111** (2007) 4776.
- [192] Waluyo, I. et al., J. Chem. Phys. **134** (2011) 64513.
- [193] Waluyo, I. et al., J. Chem. Phys. **134** (2011) 224507.
- [194] Chen, C. et al., J. Chem. Phys. **138** (2013) 154506.
- [195] Ogasawara, H. et al., Phys. Rev. Lett. **89** (2002) 276102.
- [196] Schiros, T., Andersson, K. J., Pettersson, L. G. M., Nilsson, A., and Ogasawara, H., J. El. Spec. Rel. Phen. **177** (2010) 85.
- [197] Waluyo, I., *X-Ray Study of Ice And Water on Surfaces and in Aqueous Solutions*, PhD thesis, Stanford University, 2011.
- [198] Huang, N. et al., J. Chem. Phys. **136** (2012) 74507.
- [199] Kilcoyne, A. L. D. et al., J. Synchrotron Radiat. **10** (2003) 125.
- [200] Kaya, S. et al., Sci. Rep. **3** (2013) 1074.
- [201] Robinson, I., Gruebel, G., and Mochrie, S., New J. Phys. **12** (2010) 35002.
- [202] Amann, J. et al., Nat. Photon. **6** (2012) 693.
- [203] Yang, X. and Shvyd'ko, Y., Phys. Rev. Spec. Top. - Acc. Beams **16** (2013) 120701.
- [204] Seibert, M. M. et al., Nature **470** (2011) 78.
- [205] Emma, P. et al., Nature Photonics **4** (2010) 641.
- [206] Ratner, D., *Much Ado About Microbunching: Coherent Bunching in High Brightness Electron Beams*, PhD thesis, Stanford University, 2011.
- [207] Lutman, A. A. et al., Phys. Rev. Spec. Top. - Acc. Beams **15** (2012) 030705.
- [208] Schlotter, W. F. et al., Rev. Sci. Instrum. **83** (2012) 043107.
- [209] Kunnus, K. et al., Rev. Sci. Instrum. **83** (2012) 123109.
- [210] Boutet, S. and Williams, G. J., New J. Phys. **12** (2010) 35024.
- [211] Rayleigh, F. R. S., Proc. London Math. Soc. **s1-10** (1878) 4.
- [212] DePonte, D. P. et al., J. Phys. D: Appl. Phys. **41** (2008) 195505.
- [213] Herrada, M. A., Gañán Calvo, A. M., Ojeda-Monge, A., Bluth, B., and Riesco-Chueca, P., Phys. Rev. E **78** (2008) 36323.
- [214] Wang, J., Tripathi, A. N., and Smith, V. H., J. Chem. Phys. **101** (1994) 4842.
- [215] Philipp, H. T., Koerner, L. J., Hromalik, M. S., Tate, M. W., and Gruner, S. M., IEEE Trans. Nucl. Sci. **57** (2010) 3795.
- [216] Hart, P. et al., The Comell-SLAC Pixel Array Detector at LCLS, in *Nuclear Science Symposium and Medical Imaging Conference*, pages 538–541, IEEE, 2012.



- [217] White, T. A. et al., *Acta Crystallogr. Sect. D: Biol. Crystallogr.* **69** (2013) 1231.
- [218] van Oosterom, A. and Strackee, J., *IEEE Trans. Biomed. Eng.* **30** (1983) 125.
- [219] Fu, L., *X-ray Study of the Structure of Liquid Water*, PhD thesis, Stanford University, 2008.
- [220] Krogh-Moe, J., *Acta Crystallogr.* **9** (1956) 951.
- [221] Norman, N., *Acta Crystallogr.* **10** (1957) 370.
- [222] Wikfeldt, K. T., Leetmaa, M., Ljungberg, M. P., Nilsson, A., and Pettersson, L. G. M., *J. Phys. Chem. B* **113** (2009) 6246.
- [223] Arfken, G. B., Weber, H. J., and Harris, F., *Mathematical Methods for Physicists*, Elsevier, Oxford, 7th edition, 2013.
- [224] Knudsen, M., *Ann. Phys.* **352** (1915) 697.
- [225] Maa, J. R., *Ind. Eng. Chem. Fund.* **6** (1967) 504.
- [226] Faubel, M., Schlemmer, S., and Toennies, J. P., *Z. Phys. D: Atom., Mol., Cl.* **10** (1988) 269.
- [227] Knudsen, M., *The Kinetic Theory of Gases*, Methuen, London, 1950.
- [228] Smith, J. D., Cappa, C. D., Drisdell, W. S., Cohen, R. C., and Saykally, R. J., *J. Am. Chem. Soc.* **128** (2006) 12892.
- [229] Eames, I. W., Marr, N. J., and Sabir, H., *Int. J. Heat Mass Transfer* **40** (1997) 2963.
- [230] Varilly, P. and Chandler, D., *J Phys. Chem. B* **117** (2013) 1419.
- [231] Schlesinger, D., Sellberg, J. A., Nilsson, A. R., and Pettersson, L. G. M., In preparation (2014).
- [232] Smith, J. D. et al., *Proc. National Acad. Sci. (USA)* **102** (2005) 14171.
- [233] Somayajulu, G. R., *Int. J. Thermophys.* **9** (1988) 567.
- [234] Kell, G. S., *J. Chem. Eng. Data* **20** (1975) 97.
- [235] Floriano, M. A. and Angell, C. A., *J. Phys. Chem.* **94** (1990) 4199.
- [236] Bertrand, C. E. and Anisimov, M. a., *J. Phys. Chem. B* **115** (2011) 14099.
- [237] Mayer, E. and Bruggeller, P., *Nature* **298** (1982) 715.
- [238] Pauly, H., *Atom, Molecule, and Cluster Beams Vol. I*, Springer, Berlin, 2000.
- [239] Wexler, A. and Hyland, R., A formulation for the thermodynamic properties of the saturated pure ordinary water-substance from 173.15 to 473.15 K, in *Thermodynamic properties of dry air, moist air, and water and SI psychrometric charts*, Project 216. Special publication of the American Society of Heating, Refrigerating and Air-Conditioning Engineers, Atlanta, 1983.
- [240] Hare, D. E. and Sorensen, C. M., *J. Chem. Phys.* **87** (1987) 4840.
- [241] Ramires, M. L. V. et al., *J. Phys. Chem. Ref. Data* **24** (1995) 1377.
- [242] Haymet, A. D. J. and Barlow, T. W., *Ann. N.Y. Acad. Sci.* **715** (1994) 549.
- [243] Stan, C. A. et al., *Lab on a Chip* **9** (2009) 2293.

- [244] Frenkel, J., *Kinetic Theory of Liquids*, Oxford University Press, Oxford, 1946.
- [245] Debenedetti, P. G., *Metastable Liquids*, Princeton University Press, Princeton, 1996.
- [246] Murray, B. J., O'Sullivan, D., Atkinson, J. D., and Webb, M. E., *Chem. Soc. Rev.* **41** (2012) 6519.
- [247] Nëmec, T., *Chem. Phys. Lett.* **583** (2013) 64.
- [248] Jeffery, C. A. and Austin, P. H., *J. Geophys. Res. D* **102** (1997) 25269.
- [249] Einstein, A., *Ann. Phys.* **322** (1905) 549.
- [250] Kumar, P. et al., *Proc. Natl. Acad. Sci. (USA)* **104** (2007) 9575.
- [251] Angell, C. A., *J. Phys. Chem. Solids* **49** (1988) 863.
- [252] Angell, C. A., *Science* **267** (1995) 1924.
- [253] Angell, C. A., *Chem. Rev.* **102** (2002) 2627.
- [254] Jenniskens, P. and Blake, D. F., *Astrophys. J.* **473** (1996) 1104.
- [255] Dyre, J. C., *Rev. Mod. Phys.* **78** (2006) 953.
- [256] Stillinger, F. H., Debenedetti, P. G., and Truskett, T. M., *J. Phys. Chem. B* **105** (2001) 11809.
- [257] Yokoyama, H., Kannami, M., and Kanno, H., *Chem. Phys. Lett.* **463** (2008) 99.
- [258] Abascal, J. L. F. and Vega, C., *J. Chem. Phys.* **123** (2005) 234505.
- [259] Hagen, D. E., Anderson, R. J., and Kassner, J. L., *J. Atmos. Sci.* **38** (1981) 1236.
- [260] Murray, B. J. et al., *Phys. Chem. Chem. Phys.* **12** (2010) 10380.
- [261] Riechers, B., Wittbracht, F., Hutten, A., and Koop, T., *Phys. Chem. Chem. Phys.* **15** (2013) 5873.
- [262] Stöckel, P., Weidinger, I. M., Baumgärtel, H., and Leisner, T., *J. Phys. Chem. A* **109** (2005) 2540.
- [263] Safarik, D. J. and Mullins, C. B., *J. Chem. Phys.* **121** (2004).
- [264] Angell, C. A., *J. Phys. Chem.* **97** (1993) 6339.
- [265] Ito, K., Moynihan, C. T., and Angell, C. A., *Nature* **398** (1999) 492.
- [266] Price, W. S., Ide, H., and Arata, Y., *J. Phys. Chem. A* **103** (1999) 448.
- [267] Prielmeier, F. X., Lang, E. W., Speedy, R. J., and Lüdemann, H.-D., *Ber. Bunsenges. Phys. Chem.* **92** (1988) 1111.
- [268] Ziaja, B., van der Spoel, D., Szöke, A., and Hajdu, J., *Phys. Rev. B* **64** (2001) 214104.
- [269] Ziaja, B., Szöke, A., van der Spoel, D., and Hajdu, J., *Phys. Rev. B* **66** (2002) 24116.
- [270] Timneanu, N., Caleman, C., Hajdu, J., and van der Spoel, D., *Chem. Phys.* **299** (2004) 277.
- [271] Ljungberg, M. P., Pettersson, L. G. M., and Nilsson, A., *J. Chem. Phys.* **134** (2011) 44513.
- [272] Abascal, J. L. F. and Vega, C., *J. Chem. Phys.* **133** (2010) 234502.
- [273] Overduin, S. D. and Patey, G. N., *J. Chem. Phys.* **138** (2013) 184502.